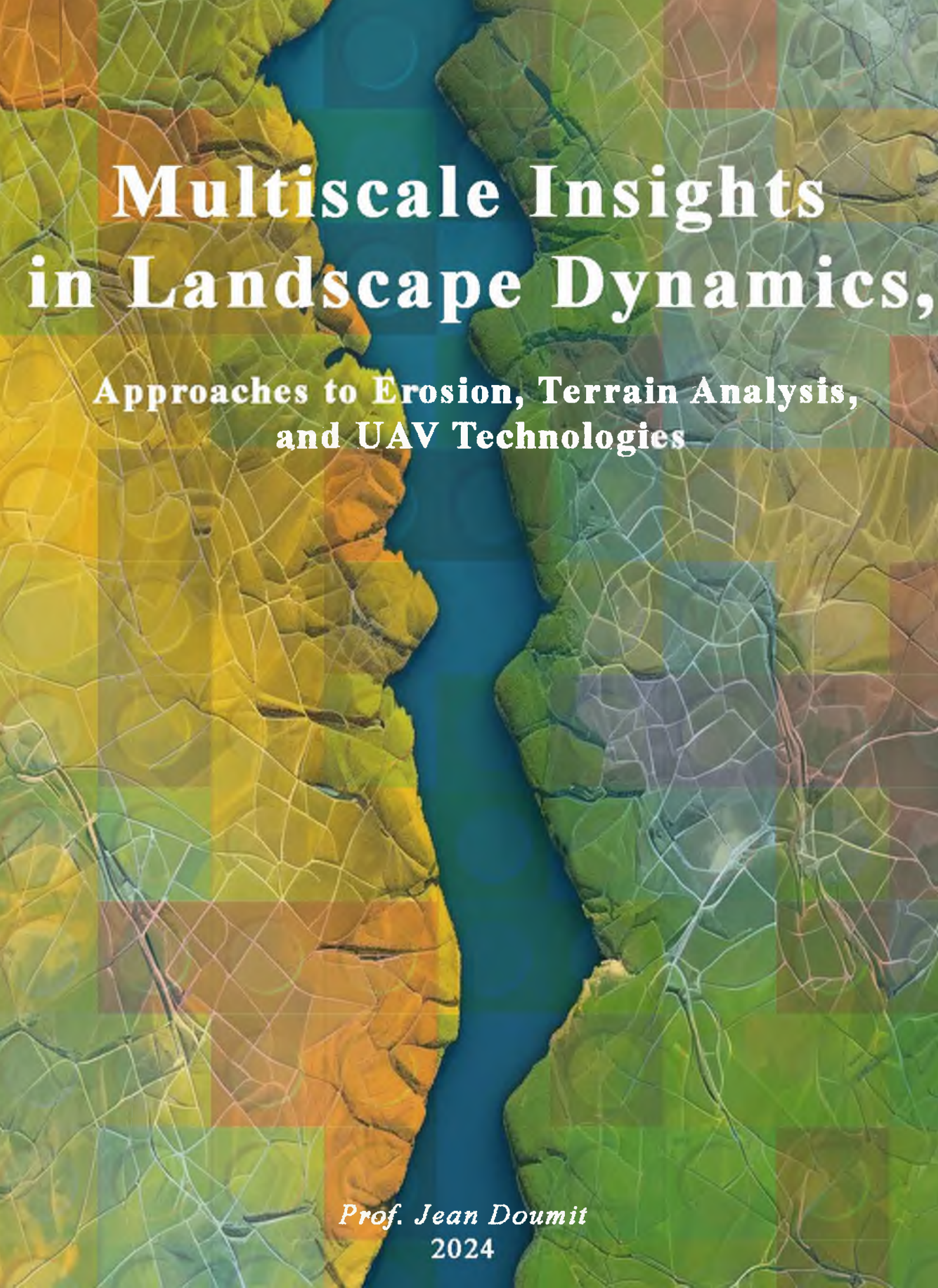

Multiscale Insights in Landscape Dynamics,

Approaches to Erosion, Terrain Analysis, and UAV Technologies

Prof. Jean Doumit

2024

Multiscale Insights in Landscape Dynamics,

Approaches to Erosion, Terrain Analysis, and UAV Technologies

Prof. Jean Doumit

2024

Editor Jean Doumit
Lebanon, Fanar, Fouad Afram El Boustany BLDG,
LEBANESE UNIVERSITY,
Faculty of Letters and Human Sciences branch 2
Geospatial Lab
DOI
jeandoumit@gmail.com

Preprint DOI
https://doi.org/10.31219/osf.io/wk47n

Disciplines
Geography Social and Behavioral Sciences Science and Technology Studies
Tags
Erosion GIS Remote sensing UAV
Original Publication Date
2024-09-26

Citations
APA
Doumit, J. (2024, September 27). Multiscale Insights in Landscape Dynamics, Approaches to Erosion, Terrain Analysis, and UAV Technologies. https://doi.org/10.31219/osf.io/wk47n

Acknowledgments

This book would not have been possible without the support and collaboration of many individuals to whom I owe my deepest gratitude.

Firstly, I would like to sincerely thank my colleagues at the Department of Geography at Lebanese University and the entire team at the Geospatial Lab. Your expertise, dedication, and camaraderie have been invaluable throughout this journey, and I feel privileged to be part of such an inspiring academic community.

I am deeply grateful to my wife for her unwavering support and encouragement, which have constantly motivated me. Her patience and belief in my work made this project possible, and I am profoundly thankful for her presence by my side.

Special thanks go to my esteemed colleague, Prof. Samar Sakr, whose insightful contributions and guidance in writing Chapter 8 significantly enriched this work. I appreciate your generosity in sharing your knowledge and willingness to help.

To all who contributed, whether through direct involvement or moral support, thank you for helping transform this book from a concept into reality.

Preface

Multiscale Insights in Landscape Dynamics, this book highlights om multiscale problems in digital terrain modeling.
I am pleased to present this book, a multiscale terrain analysis experiment on the Lebanese territory based on Digital Elevation Models. In its eight chapters:
Chapter 1, Geographic Information Systems analysis based on Digital Elevation Models (DEMs) varies with spatial resolution and dataset production method. DEMs with different spatial resolutions can lead to several results in the analysis. This chapter investigates the effects of DEMs on predicting soil erosion and deposition modeling on Lebanese river basins. Two DEMs at different spatial resolutions from two sources were used to calculate topographic and hydrological parameters for the prediction of the Sediment Transport Index (STI), the erosion-deposition based on Unit Stream Power Erosion, and the Deposition Model (USPED) considering only the topography factors expressed in DEMs.
This chapter analyzes hillslope erosion and deposition rates in a GIS to estimate sheet and rill erosion patterns in 13 Lebanese river basins. A correlation analysis is applied to test the degree of similarity between the datasets and the effect of erosion and deposition on spatial resolution. Results indicate that drill erosion and deposition influence high spatial resolution DEMs due to the excellent terrain representation, especially the concave deposition forms.
This result shows the increased rill erosivity of channel flow downstream and sediment deposition in concave areas.
Chapter 2 objective was to develop multiscale models for the identification of erosion-susceptible areas, exploring the potential of different spatial resolution open-source Digital Elevation Models (DEM) (MERIT, SRTM, ALOS AW3D, and ALOS PALSAR).
Topography and terrain derivative parameters significantly impacting erosion were calculated in a Geographical Information System based on geomorphometry algorithms and fuzzy logic functions proposed for evaluating each parameter on erosion risk in Lebanese territories.
The objective of this research was to develop four different models based on topography parameters (slope and dissection index) and terrain derivatives (LS factor, profile curvature, stream power index, and topography wetness index) to assess the susceptible areas of erosion on the Lebanese territories and explore the potential of DEMs of different spatial resolutions.
Topography parameters and terrain derivatives were computed from the DEM´s elevation, and some fuzzy logic functions were proposed to evaluate the influence of each parameter on erosion risk.
The results showed that DEM use is a relatively easy and uncostly method to identify, Qualitatively, the erosion-susceptible areas (ESA) vary with the spatial resolution (scale) and are related to the DEM way of interpolation. From this study, we can conclude that in digital erosion modeling, the correlation varies with the type and resolution of the database used and influences the shape and geometry of the Erosion-Susceptible Areas.
Chapter 3, The advanced uses of drones in geosciences, producing very high spatial resolution Digital Surface Models (DSMs) and Digital Ortho Models (DOMs) at various flight heights, led to different digital model scales.
Relief plays a vital role in forming Ephemeral Gullies (EG). This Chapter focuses on predicting multiscale EG locations using the compound topographic index (CTI) and analyzing their geometrical characteristics, such as length, depth, and volume, of the three different spatial resolutions that DSM processes from different drone flight heights.
Ephemeral Gully extracted from the three flight heights of 120, 240, and 360 meters were compared with each other to understand the effect of generalization at different scales.
The results highlight the presence of two scales: a small-scale ephemeral gully expressed by the flight heights of 240 and 360 m and a much smaller scale in the level of microrelief of the flight height of 120 m.

Chapter 4, The increasing use of unmanned aerial vehicles (UAV) and the production of high-resolution digital surface models (DSMs) lead to multi-scale results in terrain analysis, prompting new solutions to cope with multi-scale analysis. This chapter tested three indices – the local variance, texture, and fractal dimensions of the same study area with six different spatial resolutions DSM processed from different UAV flight height datasets at 20, 40, 60,120,240, and 360 meters. The higher spatial resolution DSM extracted from 20 meters of flight height was set as a base for a series of correlation analyses between the three indices to study the generalization at different scales. This approach could help understand the spatial resolution changing with scale and could be used for developing hierarchical DSM scale classifications.

Chapter 5, Surface Roughness is a crucial geomorphological variable; no single definition exists. However, we use surface roughness within geomorphometry to express variability in a topographic surface at a given scale.

Obtaining Digital Surface models (DSMs) at different scales and levels before Unmanned Aerial Vehicles (UAVs) appeared rare or impossible. UAVs with advanced photogrammetry software produce high-resolution DSMs. In this chapter, we tested terrain roughness at multiscale DSM generated from six different UAV flight heights of 20, 40, 60, 120, 240, and 360 meters.

We tested an easily calculated terrain roughness index (TRI) and the vector roughness measure (VRM), providing an objective quantitative measure of topographic heterogeneity.

The TRI and VRM values of the six DSMs were correlated to understand the influence of spatial resolution on terrain heterogeneity. Statistics and regression analysis revealed that the first three high-resolution DSMs saved the degree of roughness, and the last three generated from flight heights of 120, 240, and 360 meters lost the roughness degree with the loss of scale and spatial resolution.

Chapter 6, Obtaining Digital Surface models (DSMs) at different scales and levels before Unmanned Aerial Vehicles (UAVs) appeared rare or impossible. UAVs with advanced photogrammetry software can produce high-resolution Digital Surface Models with several spatial resolutions at multiscale levels. In this chapter, we tested the Chord Ratio (ACR) method, decouples rugosity from the slope at multiscale DSM generated from six different UAV flight altitudes of 20, 40, 60, 120, 240, and 360 meters for the study and analysis of the surface to planar areas changes with spatial resolutions.

The path of DSM to planar areas should pass by a series of surfaces: a planar slope surface and a boundary data surface to reach the horizontal planar surface.

To answer this question, did the transition of multiscale Digital Surface Models to planar areas in the same study area have the same results?

After calculating the multiscale rugosity, this chapter studies the similarity between these surfaces at multiscale by correlation and statistical analysis. Visually and statistically, planar areas of all flight heights are very similar. Correlation results showed a significant value difference due to cartographic generalization and spatial resolution.

Chapter 7, The advanced uses of unmanned aerial vehicles (UAV) in geosciences, producing very high spatial resolution digital surface models (DSMs), and the various UAV flight altitudes have led to different scales of DSM. This chapter analyzed terrain forms using the Topographic Position Index (TPI), landforms extracted by the Iwahashi and Pike method, and morphometric features of three different spatial resolutions DSM processed from different UAV flight height datasets of the same study area.

Topographic position index (TPI) is an algorithm for measuring topographic slope positions and automating landform classifications; Iwahashi and Pike developed an unsupervised method for the classification of Landforms, and we have used the techniques developed by Peuker and Douglas, a method classifying terrain surfaces into 7 classes.

Landforms extracted from the three indices listed above at the three flight heights of 120, 240, and 360 meters were compared with each other to understand the generalization of different scales and to highlight which landforms are more affected by the scale changes.

Chapter 8, Unmanned Aerial Vehicles (UAV) have recently become an attractive means of generating high-resolution Digital Surface Models (DSMs), leading to multi-scale results in terrain analysis. This has prompted new solutions to cope with multi-scale analysis.
This study has developed a UAV capable of collecting meteorological values by mounting a meteorological sensor.
At different flight heights of 50, 100, and 150 meters, aerial sensors collected photos, relative humidity, and temperature values in the Baskinta region (Lebanon). All images were processed using photogrammetric software to produce digital elevation models (DSM) and digital ortho models (DOM).
Meteorological data are translated into a Geographic Information System (GIS) to produce digital temperature and relative humidity models.
The study's significant results include building reliable high-spatial-resolution Digital Ortho Models (DOM) and Digital Surface Models (DSM) at different flight altitudes. Besides terrain data, humidity and temperature maps (sub-meter pixels) are produced to characterize a horizontal and vertical profile and evaluate the feasibility of mapping.
Digital models adopted by GIS technology can yield a treasure trove of information.
My message to the readers is: "**Think spatially**."

Contents

Chapter 1

Multiscale Impact on Hillslope Erosion and Deposition Modeling.

Digital Elevation Models (DEM) represent terrain topography in Geographic Information Systems (GIS) and can vary in resolution and accuracy. This directly moderates water flow over the Earth's surface, which moderates the potential for soil erosion (Hutchinson, 1996).

Geomorphometry is the science of extracting topographic and hydrological features from DEMs, while terrain analysis has been studied extensively over the last two decades (Mark, 1983; Doumit, 2017; Jenson, 1991; Moore et al., 1993; Florinsky, 1998).

This chapter mainly aimed to assess the topography effects of two DEM resolutions on erosion deposition for 13 watersheds in Lebanon. Since multiple types of DEMs with different spatial resolutions exist, it evaluates DEM's impact on soil erosion and deposition prediction modeling.

Therefore, topographic attributes have been used to describe spatial soil elevation, slope, and aspect (Moore et al., 1991). Scientists proposed many hydrologic and topographic indices to map hill slope erosion, soil sediments, and moisture based on field models (Grunwald, 2006), expressing the properties of their maps by numbers of pixels; this approach has been supported by the development of GIS and remote sensing technologies (Moore et al., 1991; Moore, 1996; Murphy et al., 2009).

Erosion patterns and deposition are results of rainfall, topography, groundwater flow, vegetation cover and growth, and soil detachment. This paper only focused on the main factors influencing erosion, topography excluding other geographical factors. Here, terrain analyses the mathematical representation of sediment transport and erosion-deposition processes.

The fast evolution of GIS erosion modeling workflows made the data processing and analysis very fast and easy by applying scripts and model builders.

This project aimed to assess the impacts of DEM spatial resolution on sheet and rill erosion and deposition in watershed basins. The paper addresses the quantitative estimation of soil erosion to better understand the overall connectivity between erosion type and terrain scale represented by DEM, using a soil erosion and transport model implemented in a Geographical Information System.

Thus, the model focuses on the complex interaction between topography affecting the potential for soil erosion and how the spatial distribution of these factors leads to variations in sheet and rill erosion and deposition within a watershed based on pixel size.

This paper identifies and predicts the spatial patterns of soil rill and sheet erosion with sediment deposition inside the Lebanese watersheds based on MERIT and ALOS DEMS.

MATERIALS AND METHODS

GIS and Digital Elevation Models (DEM) can be used to perform watershed delineation. Our study used the ArcHydro GIS algorithm developed for building hydrologic information systems to delineate watersheds. Lebanon includes 16 river basins, 13 of which flow in the Mediterranean Sea, moving a massive quantity of sediments and constituting the study area of our research (Figure 1).

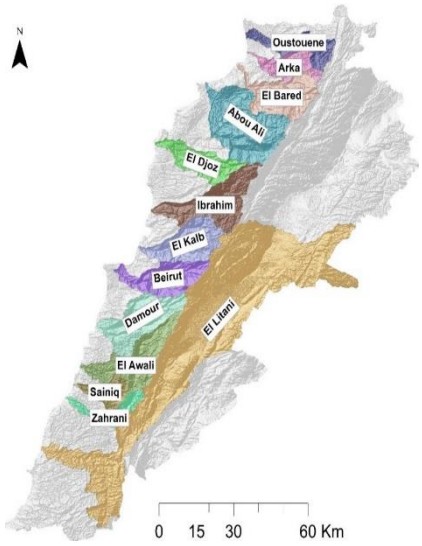

Fig. 1.1 River Basins of the Study Area Draped on the Hill Shade Map of Lebanon

The different DEMs, MERIT, and ALOS used in this study show different spatial resolution datasets. The MERIT DEM has a 90-meter spatial resolution and is made from the existing free-of-charge SRTM and AW3D with correction of component error (Yamazaki et al., 2017).
The second DEM, ALOS, from the Japan Aerospace Exploration Agency (JAXA) dataset, has a spatial resolution of 30 meters (Takaku et al., 2016).
According to Kothari et al. (2002), there are many methods to estimate sediment transport; they reported that the best GIS-suited method is the one proposed by Moore and Wilson (1992), based on unit stream power theory and called the Sediment Transport Index (STI). It is a non-linear function of specific discharge and slope, and it is derived by considering the transport capacity limiting sediment flux and catchment evolution erosion theories (Moore & Wilson, 1992). This index is a fundamental Universal Soil Loss Equation (USLE) factor. It calculates sediment transport capacity and may be better suited to landscape erosion assessments than the USLE because it considers the flow convergence and divergence (Moore & Wilson, 1992; Desmet & Govers, 1996).

$$\mathrm{STI} = \left[(m+1).\left(\frac{A_s}{22.13}\right)^{m}.\left(\frac{\sin\beta}{0.0896}\right)^{n}\right] \quad (1)$$

Where "As" is the flow accumulation, "β" is the slope. The flow accumulation determines water accumulation from upstream areas and identifies areas that contribute to overland flow. The exponents m and n control the relative impact of water and slope terms and reflect different erosion patterns, with higher values reflecting the pattern for prevailing rill erosion and lower exponent values close to 1 reflecting the pattern of both rill and sheet erosion; previous studies have used the recommended m = 1.6 and n = 1.3 for rill erosion and m = 1.0 and n = 1.0 for sheet erosion (Garcia et al., S., 2012; Liu et al., 2003; Warren et al., 2000).
The model applied for this paper is a modified version of the USPED (Unit Stream Power Erosion Deposition), which calculates sediment erosion and deposition in the hillslope erosion processes, and it is like the USLE but calculated based on upslope contributing area (Liu et al., 2007; Mitasova et al., 1996). Therefore, the sediment transport capacity (T) is defined in the following equation (2):

$$T = R \times K \times C \times P \times A^{m} \times (\sin\beta)^{n} \quad (2)$$

where R is the rainfall, K is the soil erodibility, C is the cover and management factor, P is the conservation practice factor, A is the upslope contributing area, and β is the slope inclination angle in degrees (Leh et al., 2011; Mitasova & Mitas, 2001; Mitasova et al., 1999).
As in this paper, we only test the influence of topography factors on hillslope erosion and its relationship with DEM spatial resolution. We applied the Sediment Transport Index (STI) instead

of transport capacity (T) in the Erosion Deposition (ED) equation (3), where α reflects the aspect of the elevation surface (Oliveira et al., 2013).

$$\mathrm{ED} = \frac{d(T\cos\alpha)}{dx} + \frac{d(T\sin\alpha)}{dy} \quad (3)$$

To make the equation easy to implement in GIS, Mitasova et al. (1996) used the relationship between partial derivatives and surface slope β and aspect α of equation (4) to the ED equation (3) Mitasova et al. (1996).

$$\frac{dz}{dx} = \tan\beta \times \cos\alpha, \frac{dz}{dx} = \tan\beta \times \sin\alpha \quad (4)$$

Simulation results from the USPED model can be positive, indicating soil deposition, or negative, indicating soil erosion.

The topography is only one of many factors that can affect water erosion. DEMs resulted in substantially different resolutions, which led to different terrain models and, therefore, different erosion results.

The approach used MERIT and ALOS DEMs to compare the spatial distribution of rill and sheet erosion and sediment deposition.

The modeled patterns of erosion and deposition rates in the basins were analyzed only based on topographic forcing; the model was run only with the topographic factor present in the calculation of USPED.

DISCUSSIONS AND RESULTS

The terrain topography plays the most crucial role in the erosion and deposition of the watershed basins; the increasing of the upslope contributing area values combined with a high slope value of the local slope could lead to a high sediment transport rate, same as the areas with concave slope profile of convergent accelerated flow. The areas with high transport rates are also associated with concave slope profiles and valleys because these are areas of convergent accelerated flow; in the areas with high sediment transport, the rill erosion is higher than the sheet erosion.

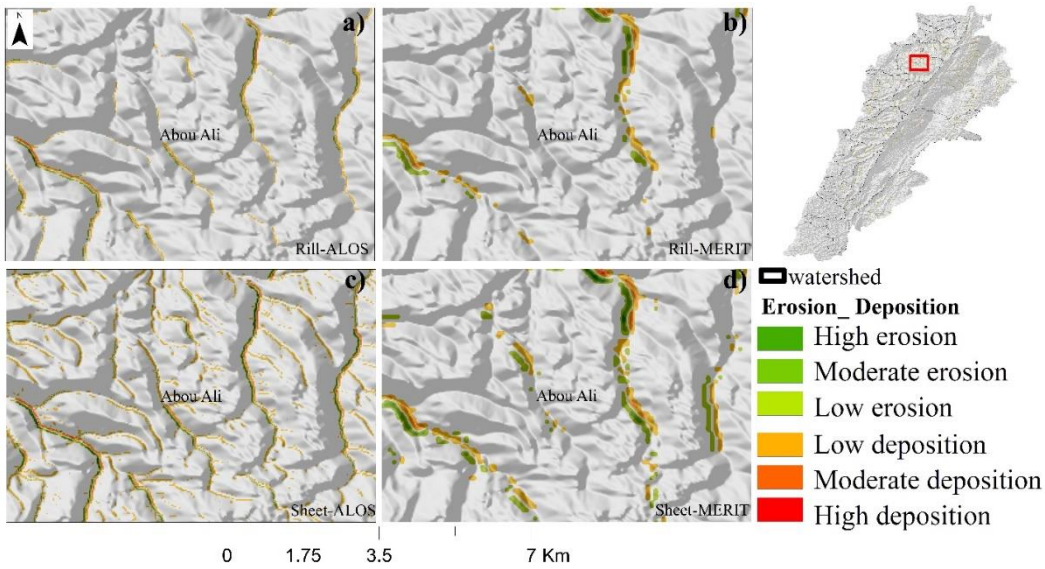

Fig. 1.2 Erosion Deposition Maps of Abou Ali River, a) Rill Erosion and Deposition in ALOS, b) Rill Erosion and Deposition in MERIT, c) Sheet Erosion and Deposition in ALOS, d) Sheet and Deposition Erosion in MERIT

The sediment transport rate expressed in equation 3 identifies areas where it increases in the upslope contributing area and leads to erosion in ED negative values, decreases with ED positive values leading to deposition, or stays constant with values near zero for areas stable with no net erosion and deposition.

The resulting ED maps of Lebanese watershed basin topography based on ALOS and MERIT DEMs show that estimated high erosion and deposition areas are in the North of Lebanon in the El Bared and Abou Ali basins (Figure 1.3).
Figure 2 shows the Sheet and Rill ED maps of the Abou Ali basin generated from the ALOS and MERIT datasets. Figure 2a of the Rill ED ALOS map shows a low rate of erosion and deposition, contrary to Figure 2b, the Rill ED generated from the MERIT dataset, which shows a high rate of erosion and deposition due to the high spatial resolution.
The ALOS sheet ED of Figure 1.2c shows a scattered spatial distribution of sheet erosion and deposition in most of the concave areas, unlike the sheet ED, which shows a concentration of sheet deposition and erosion in deep valleys (Figure 1.2d).

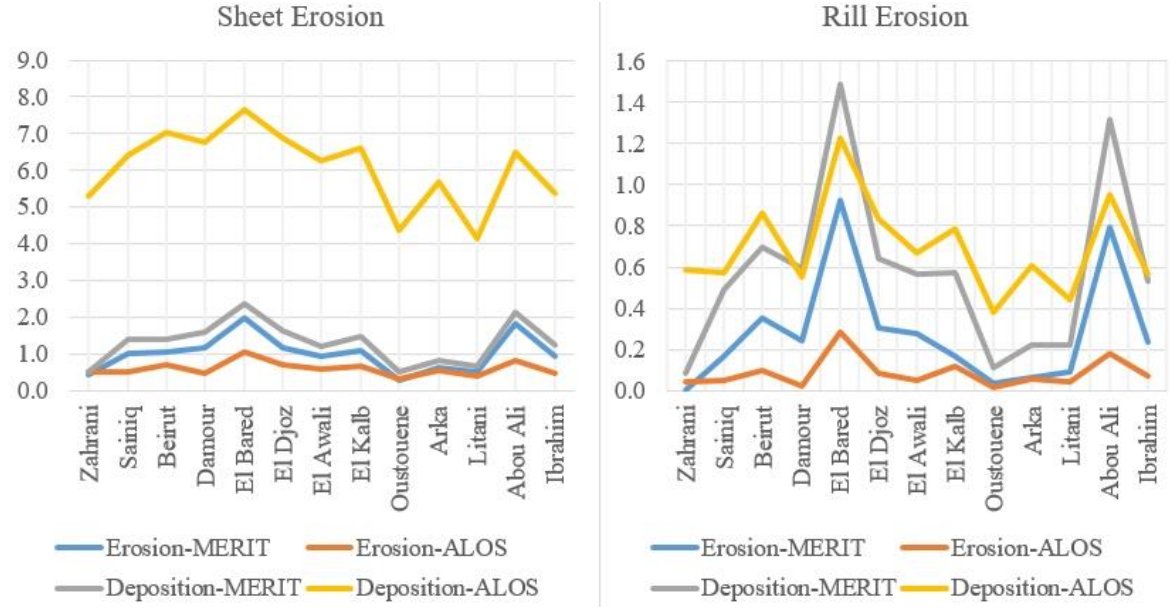

Fig. 1.3 Diagrams of Rill and Sheet Erosion Areas in Lebanese Watershed Basins

The graphs of Figure 1.3 of Sheet and Rill Erosions, with percentages of areas (Y axes) in each basin, show a very high percentage of areas for deposition in ALOS datasets for all Lebanese watersheds, with very high values for El Bared and Abou Ali basins and a very low percentage of area for Oustouene and Damour basins.
The comparison between elevation data sets for sheet erosion gives a proportional percentage of areas between erosion and deposition of MERIT datasets; otherwise, heterogeneity in the percentage of areas between Erosion and Deposition in ALOS datasets when deposition occupied extensive areas against erosion with a lower percentage of areas.
In the diagram of rill erosion in Figure 1.3, we can see very similar graphs for all basins, with some exceptions in the Zahrani basin. The Erosion percentage in ALOS datasets is higher than That in MERIT datasets, and the Deposition of ALOS datasets is lower than that in MERIT datasets in the Damour, El Bared, and Abou Ali basins.
Due to the unexpected results of the difference in the percentage of areas between the ALOS and MERIT datasets for rill erosion and deposition, we calculated the percentage of areas of the classified erosion and deposition in the MERIT and ALOS datasets (Figure 1.4) and (Figure 1.6).

Table 1.1 Percentage of Sheet Erosion and Deposition Areas of ALOS and MERIT.

		Sheet Erosion-MERIT %						Sheet Erosion-ALOS %					
		Erosion			Deposition			Erosion			Deposition		
Basin	Area Sq/Km	High	Moderate	Low	Low	Moderate	High	High	Moderate	Low	Low	Moderate	High
Zahrani	102	-	-	0.413	0.518	0.007	-	0.005	0.056	0.445	5.092	0.201	0.014
Sainiq	109	-	0.119	0.903	1.252	0.132	-	0.004	0.072	0.422	6.197	0.194	0.020
Beirut	237	0.033	0.165	0.845	1.187	0.192	0.033	0.013	0.119	0.563	6.660	0.335	0.030
Damour	308	-	0.104	1.061	1.463	0.128	-	0.001	0.039	0.420	6.584	0.174	0.004
El Bared	263	0.040	0.508	1.441	1.806	0.538	0.021	0.084	0.251	0.718	7.013	0.503	0.132
El Djoz	194	0.022	0.183	0.959	1.412	0.183	0.015	0.011	0.110	0.594	6.538	0.311	0.026
El Awali	297	0.012	0.147	0.786	1.032	0.156	0.007	0.003	0.068	0.504	6.030	0.229	0.009
El Kalb	254	-	0.062	1.019	1.386	0.095	-	0.022	0.126	0.515	6.272	0.305	0.044
Oustouene	164	-	0.013	0.279	0.486	0.021	-	0.001	0.027	0.297	4.240	0.130	0.002
Arka	133	-	0.042	0.574	0.775	0.032	-	0.009	0.075	0.455	5.427	0.223	0.015
Litani	2110	-	0.051	0.442	0.596	0.053	0.002	0.006	0.051	0.317	3.964	0.152	0.012
Abou Ali	472	0.146	0.360	1.330	1.631	0.402	0.11	0.040	0.178	0.589	6.056	0.374	0.072
Ibrahim	332	-	0.113	0.813	1.132	0.126	-	0.015	0.078	0.375	5.128	0.213	0.026

Table 1.1 of the area percentage of the degree of erosion and deposition between MERIT and ALOS of sheet erosion; the highest sheet erosion areas of MERIT datasets are found in the Abou Ali basin, followed by El Bared basin, contrary to ALOS sheet erosion, the highest area found in El Bared followed by Abou Ali.

While the Oustouene basin has lower sheet erosion percentages of MERIT and ALOS areas, the Beirut basin has a precise symmetrical percentage of areas between sheet erosion and sheet deposition.

An independent-sample t-test was conducted to compare the results of MERIT and ALOS in sheet erosion and deposition of the two datasets. There was a significant difference in the scores for low levels of sheet erosion ($P<0.05$) Figure 5. The MERIT method expressed the highest results in a low level of sheet erosion due to gentle terrain slopes and the low spatial resolution of MERIT datasets. Otherwise, ALOS datasets showed a highly significant difference ($p<0.01$) compared with MERIT datasets in a low level of sheet deposition, reflecting a decrease of values in low-level erosion of ALOS datasets. These results prove the effect of spatial resolution on sheet erosion and deposition modeling. Specifically, our results suggest that high-resolution datasets lead to better modeling erosion and deposition results.

Table 1.2 Statistical Analysis for Results Obtained with MERIT and ALOS Datasets for Sheet Erosion and Deposition.

		Sheet Erosion/Deposition	
	Level	MERIT	ALOS
Erosion	High	0.019 ± 0.041^{a}	0.016 ± 0.023^{a}
	Moderate	0.102 ± 0.139^{a}	0.096 ± 0.062^{a}
	Low	0.835 ± 0.345^{b}	0.478 ± 0.119^{a}
Deposition	High	0.01477 ± 0.31594^{a}	0.03123 ± 0.035570^{a}
	Moderate	0.15885 ± 0.152957^{a}	0.25723 ± 0.104296^{a}
	Low	1.12892 ± 0.427406^{a}	$5.7847 \pm 0. .94704^{b}$

[a,b] *Values with different superscripts in a row differ significantly ($p<0.05$).*

In general, the values of area percentage in sheet erosion and deposition of MERIT and ALOS are very homogeneous, as shown in the diagram (Figure 1.3).

Table 1.3 Percentage of Rill Erosion and Deposition Areas of ALOS and MERIT.

		Rill Erosion-MERIT %						Rill Erosion-ALOS %					
		Erosion			Deposition			Erosion			Deposition		
Basin	Area Sq/Km	High	Moderate	Low	Low	Moderate	High	High	Moderate	Low	Low	Moderate	High
Zahrani	102	-	-	-	0.084	-	-	-	-	0.045	0.561	0.023	-
Sainiq	109	-	-	0.165	0.474	0.013	-	-	-	0.053	0.544	0.029	-
Beirut	237	0.012	0.063	0.280	0.613	0.069	0.015	-	0.001	0.095	0.810	0.050	0.001
Damour	308	-	0.005	0.237	0.576	0.019	-	-	-	0.023	0.543	0.008	-
El Bared	263	0.005	0.102	0.817	1.320	0.161	0.005	0.004	0.027	0.252	1.022	0.172	0.032
El Djoz	194	-	0.051	0.252	0.574	0.066	-	-	-	0.087	0.785	0.050	-
El Awali	297	-	0.041	0.233	0.529	0.038	-	-	-	0.047	0.645	0.023	-
El Kalb	254	-	0.006	0.160	0.565	0.008	-	0.001	0.007	0.113	0.715	0.065	0.008
Oustouene	164	-	-	0.034	0.112	-	-	-	-	0.014	0.377	0.005	-
Arka	133	-	-	0.064	0.223	-	-	-	0.004	0.049	0.581	0.020	0.004
Litani	2110	-	0.011	0.083	0.209	0.013	-	-	0.001	0.039	0.419	0.020	0.001
Abou Ali	472	0.037	0.219	0.537	1.025	0.249	0.042	0.002	0.012	0.168	0.830	0.107	0.014
Ibrahim	332	-	0.011	0.227	0.516	0.017	-	0.001	0.003	0.067	0.521	0.038	0.004

According to the independent-sample t-test, values in a low level of MERIT rill erosion were significantly higher ($P<0.05$) than those obtained from ALOS datasets Table 1.4. These results are very similar to the results of MERIT sheet erosion, with differences at low levels. Otherwise, there is no significant difference between MERIT and ALOS datasets for rill deposition in all levels, especially the lower ones. Having no significant results in rill deposition is related to small deposition areas.

For Both datasets and at all levels, deposition and erosion have a significant way of ($p<0.05$) due to the strict separation between levels obtained through classification formulas.

Table 1.4 Statistical Analysis for Results Obtained with MERIT and ALOS Datasets for Rill Erosion and Deposition

		Rill Erosion/Deposition	
	Level	MERIT	ALOS
Erosion	High	0.00415 ± 0.010463a	0.00062 ± 0.001193 a
	Moderate	0.03915 ± 0.062576 a	0.00423 ± 0.007726 a
	Low	0.23762 ± 0.221871 b	0.08092 ± 0.065916a
Deposition	High	0.00477± 0.011966a	0.00492 ± 0.009142a
	Moderate	0.05023± 0.074573 a	0.04692 ± 0.046428 a
	Low	0.52462± 0.348231 a	0.64254 ± 0.182125 a

[a,b] *Values with different superscripts in a row differ significantly ($p<0.05$).*

This study has found that drill erosion and deposition influence high spatial resolution DEMs due to the excellent terrain representation, especially the concave deposition forms.

This result shows the increased rill erosivity of channel flow downstream and sediment deposition in concave areas.

STI values influenced the calculation of ED and reflect sediment accumulation because they demonstrate sediment flow convergence and divergence.

Mitasova et al. (1996) documented high DEM spatial resolution as the most reliable elevation data for erosion and deposition modeling.

CONCLUSION

This study tested the DEM spatial resolution impact on hillslope sheet and rill erosion and deposition modeling of Lebanese watersheds. The model framework included STI applied to the USPED to estimate soil erosion and deposition.

The model was evaluated for different DEM spatial resolutions ALOS 30-m and MERIT 90-m and topographic exponents n=m =1.0 for sheet erosion and n=1.3, m=1.6 for rill erosion.

This study demonstrated the importance of spatial resolution and topographic exponents in estimating and mapping soil redistribution with spatial identification, where erosion and deposition occur at high rates in Lebanese watershed basins influenced by only hydrological and topographic factors. Additional work is needed to improve the current results for these basins by better characterizing the rainfall erosivity and land cover management factors and by considering the effect of changes in topography over time caused by erosion and deposition. Future work would also include applying the model framework over larger agricultural areas and improving predictions about soil erosion and deposition in agricultural landscapes.

Depending on the project's scale, we suggest using high-spatial-resolution DEM for modeling erosion and deposition at local scales and low-spatial-resolution datasets for global scales.

Chapter 2

Multiscale terrain analysis for erosion area identifications

Water Soil erosion has been recognized as a severe hazard because it reduces soil productivity by removing the most fertile topsoil (Shrestha, 1997; Angima et al., 2003).
The applications of remote sensing (RS) and Geographic Information System (GIS) technologies together can make the study more viable, as they handle complex issues and large databases for manipulation and retrieval much more efficiently.
The study area's topographic morphometric characteristics have been addressed using spatial information technology to prepare erosion susceptibility maps based on topography parameters and terrain derivatives in a GIS environment.
Soil surveys provide information about areas with erosion but do not show which areas are susceptible to erosion. The first and second elevation derivatives at multiscale (spatial resolution) DEM are applied to highlight erosion risk at different levels.
The erosion modeling, with its bad spatial resolution and low level of detail, only shows areas with a high incidence of erosion processes. Our research analyzed the multiscale details of erosion areas from global to local scales.
Some research does not consider the effect of scale by merging different spatial resolution digital maps like soil, land use, and topography for soil erosion modeling. Erosion models differ in complexity, requirements, and inputs, the processes they represent, the scale of their intended use, and the types of information they provide (Aksoy & Kavvas, 2005; Merritt et al., 2003).
In his paper, Kienzle (1994) used terrain variables to distinguish between terrain units and estimate soil erosion potential; he determined that slope and soil erosion estimations increase with a decrease in grid cell size.
Saulinier et al. 1997 investigated the analytical compensation between terrain derivatives and grid resolution and found that the topographic index increases with grid cell size.
Zhang and Montgomery (1994) compared the elevation data grid cell sizes and found that the grid size affected the hydrological simulations.
These studies have shown that the DEM spatial resolution affects derived terrain parameters and prove that the chosen grid cell size limits the ability to carry out a realistic terrain analysis and will affect erosion modeling, deposition, and water quality processes.
Spatial resolutions selected to overlay DEM with another raster should be approximately the same to output a valid analysis and modeling.
Several erosion models are based on GIS analysis of various modifications and versions of the Universal Soil Loss Equation (USLE) (Warren et al., 1989; Flacke et al., 1990; Huang & Feng, 1990). The USLE was developed for an agricultural application, not landscape-scale erosion modeling. Therefore, the application of USLE in GIS for complex terrain is somewhat restricted (Foster & Wischmeier, 1974; Moore & Wilson, 1992).
Recently developed erosion models based on the stream power theory (Moore & Wilson, 1992; Mitasova & Iverson, 1992; Hofierka, 1992; Mitasova et al., 1996) include the influence of terrain forms and are therefore more suitable for complex topographic conditions.
This chapter assesses how spatial resolution affects topography parameters and terrain derivatives to identify erosion-susceptible areas.
In other words, terrain derivatives include topography parameters, slope, and dissection index, as well as profile curvature (Kv), topographic wetness index (TWI), stream power index (SPI), and LS factor (LS).
The topography influences the transport and accumulation of sediments, depending on the relief characteristics. Hence, the effect of relief on erosion has been related to the shape and uniformity of the slope (Toy et al., 2002).

DEMs have a high potential to characterize topography as an essential input for different erosion models (Mitasova et al., 1996; Moore et al., 1991).
Terrain analysis is a quantitative GIS technique for analyzing terrain and geomorphic processes at various scales using DEMs (Wilson & Gallant, 2000).
Terrain analysis methods extract and analyze topography parameters and terrain derivatives to determine factors in modeling ESA (King et al., 2005).
The importance of terrain derivative offers an opportunity to describe patterns as a process function (Wilson & Gallant, 2000; Moore et al., 1991) and includes LS factor, profile curvature, stream power, and topographic wetness indices. The objective of this research was to explore the potential of multiscale DEM as a data source, to calculate the variables of relief that have the more significant impact on erosion, and to develop a model for assessing the risk of erosion,

MATERIALS AND METHODS

Lebanon is a mountainous land with an elevation interval of 0 – 3080 above sea level. Its area is 10452 square kilometers, and its physiography ranges from coastal plains in the lowlands to very rugged and snow-covered high mountains. In such landscapes, the topography is an overriding erosion factor.
Figure 2.1 of the study area shows the elevation map of Lebanon, highlighting the geomorphological structures with hydrological networks.

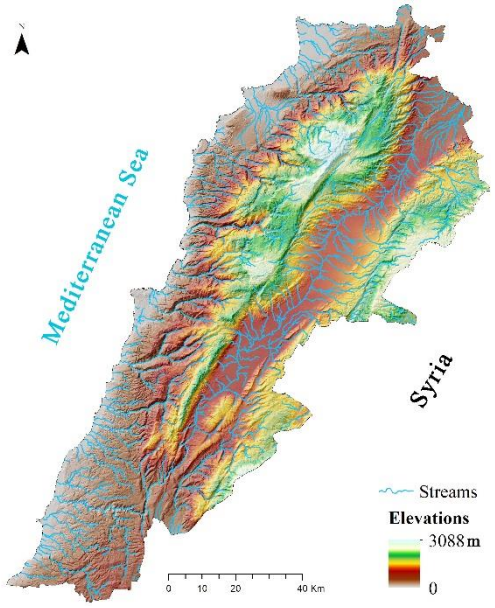

Fig.2.1 Elevations Map of Lebanon with stream network

Multiresolution datasets used in this study are MERIT, SRTM, AW3D, and ALOS.
The MERIT DEM was developed by removing DEM errors such as stripe noise, speckle noise, and tree height bias from Shuttle Radar Topographic Mission (SRTM) and ALOS World 3D (AW3D). MERIT DEMs are freely available for research and education purposes and represent terrain elevations at a 90 m spatial resolution (Yamazaki et al., 2017).
The Shuttle Radar Topography Mission (SRTM) elevation with worldwide coverage of corrected void-filled data at a resolution of 30 meters (USGS, 2006).
ALOS Global Digital Surface Model "ALOS World 3D (AW3D)" from the Japan Aerospace Exploration Agency (JAXA) released the global digital surface model (DSM) dataset with a horizontal resolution of 30-meter mesh free of charge for scientific research and education (Takaku et al., 2016).
PALSAR is one of the Advanced Land Observing Satellite systems (ALOS),
It offers corrected DEM, with a pixel size of 12.5 m; these data are free of charge on the Alaska Satellite Facility website (Logan et al., 2014).

The multiscale datasets used in this study expressed in spatial resolution as MERIT (90 m), SRTM (30 m), AW3D (30 m), and ALOS (12.5 m), the same pixel size of SRTM and AW3D with 30 meters used to test the erosion susceptible area at different types of datasets.
For the calculation of topography parameters (TP), the slope is calculated as the first terrain derivative directly from DEMs, and the dissection index (DI) is calculated based on Maximum relief (Rmax), minimum relief (Rmin), and relative relief (Rr).
The Slope Angle (SA) Calculated from a DEM is relatively simple based on the ArcMap method using the quadratic surface algorithm (Srinivasan & Engel, 1991; ESRI, 1997). Much higher slope angle values estimate erosion risks. The slope angle also corresponds to the direction of the land.
Absolute relief (AR) means the maximum height of any region, expressing the elevation above the sea level. Relative relief (RR) represents the difference in elevation between the highest and lowest points falling in a unit area (square grid). It was the first time a scientific and systematic study of relative relief was done (Smith, 1935).
DEM's highest and lowest points were calculated in a GIS module by the maximum and minimum focal statistics on a 3 x 3 grid; the difference between the generated grids presents a better erosion index in the development stage (Doumit & Kiselev, 2018).
Dissection Index (DI) is the relative relief and absolute altitude ratio. The areal differentiation of this ratio will give a good index value when estimating the vertical balance of erosion.
Nir (1957) calculated the 'Dissection Index" as the ratio of relative relief and absolute relief within a specific areal unit following equation 1.

$$DI = \frac{RR}{AR} \qquad (1)$$

DI gives a better understanding of the landscape; its values range from 0, the complete absence of dissections, to 1, a vertical cliff. DI expresses the relationship between the vertical distance from the erosion level and relative relief (Jha, 1996).
Absolute Relief (AR) is the maximum elevation of a unit area (3 x 3 cells). It is a function of tectonic processes to delineate an area's structural and erosional characteristics. A DEM's maximum focal statistics calculates AR.
Relative relief (RR) represents the difference in elevation between the maximum and minimum elevations in a unit area. In some studies, relative relief is called relief energy, as per Doumit (2017).
The calculation of erosion-susceptible areas was performed with a fuzzy equation applied to all parameters extracted from DEMS (MERIT. SRTM, AW3D, and ALOS) that integrates the effect of elevation on erosion factors by limiting the values of topographic parameters (SA and DI) from 0 to one in an ascending scale from less to more susceptible to erosion. The output of the applied fuzzy operations on topography parameters was four slope angle maps (SA_{MERIT}, SA_{SRTM}, SA_{AW3D}, and SA_{ALOS}) and four Dissection index maps (DI_{MERIT}, DI_{SRTM}, DI_{AW3D}, and DI_{ALOS}).
This study chose terrain derivatives (TD) that strongly influence erosion, such as the LS factor, Profile curvature, Topographic Wetness Index, and Stream Power Index.
The LS factor represents the terrain's influence on erosion, reflecting that erosion increases with slope angle and length. The traditional USLE method for computing the LS factor is Wischmeier and Smith (1978).

$$LS = \left[\left(\frac{\lambda}{22.13}\right)^{t} (65.4\, sin^2\beta + 4.56 \sin\beta + 0.0654)\right] \qquad (2)$$

Where λ is the horizontal projection of slope length.
t is the constant dependent on the value of the slope.
β The slope angle in degrees.

In this study, we applied a GIS method for calculating the LS factor, the same as the method used by (Dunn & Hickey, 1998; Hickey, 2000).
Hickey (2000) explained how to calculate the LS factor based on DEM and mentioned that Slope length calculations are often the most problematic of the erosion model parameters, not the slope angle.
In his method, Hickey 2000 generates a flow direction from depression less DEM; besides the Maximum slope angle, a non-cumulative slope length calculated the cumulative downhill slope length than the LS values (Hickey, 2000).
Haan et al. (1994) have shown that increasing slope length produces higher overland flow velocities and correspondingly higher erosion (Haan et al. 1994).
Profile curvature or vertical curvature *Kv* is the terrain curvature in the vertical plane parallel to the local slope direction and is defined as:

$$Kv = \frac{\theta_{xx}\theta_x^2 + 2\theta_{xy}\theta_x\theta_y + \theta_{yy}\theta_y^2}{\theta_x^2 + \theta_y^2\sqrt{\left(\theta_x^2 + \theta_y^2 + 1\right)^3}} \qquad (3)$$

where θ_x is the slope in the x-direction, θy is the slope in the y-direction, θxx is the second derivative of the slope in the x-direction, and θyy is the second derivative of the slope in the y-direction, and θxy is the second derivative of the product of the slopes in the direction of x and y. Profile curvature measures the rate of change in slope; Kv is negative on concave profiles and positive on convex profiles, while zero on straight profiles (Shary, 1995). Geomorphologically, relative deceleration areas are known as 'concave,' while relative acceleration areas are 'convex.' Profile curvature is a significant topographic element that shows which process tends to be dominant, whether erosion or deposition. On convex terrains, erosion is more likely to prevail, as well as on concave deposition (Wilson & Gallant, 2000; Neteler & Mitasova, 2008; Kennelly, 2008; Doumit, 2017). Profile curvature is important because it reflects the change in slope angle and controls the change of mass velocity flowing down along the slope curve (Evans, 1980).

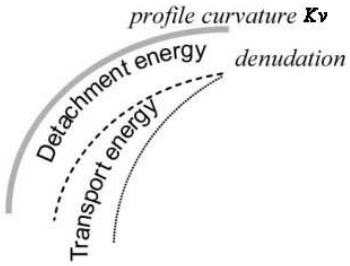

Fig.2.2 Effect of Profile curvature on erosion.

The profile curvature *Kv* is derived from the slope gradient, which expresses the ratio of gravity force down and perpendicular to the slope. Considering the part of gravitational energy expended for detachment and transport (Figure 2.2), the rate of slope denudation (detachment and transport) will be related to the change of acceleration/deceleration of flows (amount of material removed or deposited) on the slope profile (Minár et al., 2013).
The topographic wetness index (TWI) is defined as the log of the ratio of the Specific Catchment Area (As) and the tangent of the gradient at a given location. TWI is a parameter that describes the tendency of a cell to accumulate water; it was calculated in formula 4 (Beven, 2001):

$$TWI = In\left(\frac{A_S}{\tan\theta}\right) \qquad (4)$$

whereas is the specific catchment area, and θ is the degree slope.
The TWI has been used to indicate the potential of saturated areas and predict the distribution of local soil moisture (Blyth et al., 2004; Guntner et al., 2004). TWI is also used to predict spatially varying evapotranspiration and the liability to erosion (Xu & Li, 2003; Stieglitz et al., 2003).

The stream power index (SPI) is a secondary topographic attribute. It has been used to measure the erosive power of flowing water and could identify places that reduce the erosive effects of concentrated surface runoff, such as grassed waterways (Moore et al., 1991).
The calculation of this parameter is done with the following Eq. 5:

$$SPI = A_s \tan\theta \qquad (5)$$

SPI is derived from the slope and the contributing area of flow accumulation. SPI evaluates erosive power not just in streams but across the whole landscape; it predicts contributing areas where the erosive power of overland flow will be the highest (Wilson & Gallant, 2000).
Pike et al. (2009) used various terrain analyses, including SPI, to model the erosion potential of ephemeral gullies and then compared those results to real-world conditions. They found that about 80% of the calculated SPI values successfully identified areas of observed gully formation (Pike et al., 2009).
The same Topography parameters (TP) calculation of erosion susceptible areas was performed with a fuzzy equation applied on Terrain Derivatives (TD) extracted from DEMS (MERIT. SRTM, AW3D, and ALOS) that integrates the effect of first and second elevation derivatives on erosion factors, by limiting their values from 0 to one in an ascending scale from less to more susceptible to erosion. An output of the applied fuzzy operations was sixteen terrain derivatives maps, from LS factor (LS_{MERIT}, LS_{SRTM}, $LS_{AW3D,}$ and LS_{ALOS}), from profile curvature (Kv_{MERIT}, Kv_{SRTM}, $Kv_{AW3D,}$ and Kv_{ALOS}), from Topographic Wetness Index (TWI_{MERIT}, TWI_{SRTM}, $TWI_{AW3D,}$ and TWI_{ALOS}), from Stream Power Index (SPI_{MERIT}, SPI_{SRTM}, SPI_{AW3D} and SPI_{ALOS}).

DISCUSSIONS AND RESULTS

With the results of this study, we identified areas susceptible to erosion based on topography parameters (TP) and terrain derivatives (TD) from multiscale DEMs.
The Hamacher fuzzy function assesses the topography's sensitivity to erosion. This function allows the integration of the effect of geomorphometric parameters on soil erosion. It uses fuzzy connectives to combine the effects of several parameters in multi-criteria decision-making (Canuto et al., 2003).
We used fuzzy logic and the AND operation to calculate Topography Parameters and Terrain Derivatives grids. Reynolds (2001) proposed this method, which is implemented mathematically as a minimum function on the set of logical antecedents.

$$AND(x) = Min_{(x)} + \frac{(Mean_{(x)} - Min_{(x)})(Min_{(x)} + 1)}{2} \qquad (6)$$

$Min_{(xi)}$ = i =1 ..., n the minimum value for erosion factors (topographic parameters and terrain derivatives).
$Mean_{(xi)}$ = the weighted average of xi for erosion factors (topographic parameters and terrain derivatives).
Where AND is a minimum-biased weighted average of the logical antecedents.
Topographic parameters have been calculated with an equal weight because slope and dissection index have approximately the same influence as erosion factors and give as an output four maps of erosion-susceptible areas (TPMERIT, TPSRTM, TPAW3D, and TPALOS). Figure 2.3.
Terrain derivatives, such as profile curvature, LS factor, and stream power, have been weighted as strongly influencing erosion. With a moderate influence on erosion comes the Topographic Wetness Index. It outputs four maps of erosion-susceptible areas (TDMERIT, TDSRTM, TDAW3D, and TDALOS). Figure 2.4.

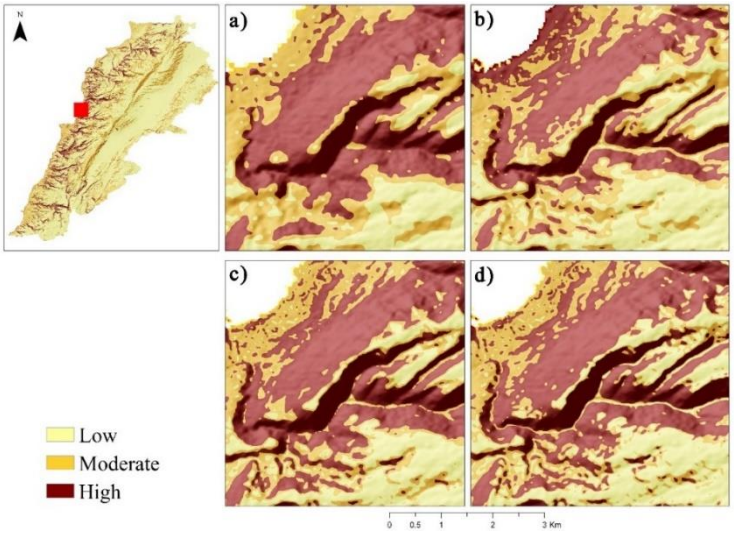

Fig.2.3 Erosion susceptible areas based on Topography parameters, a) TP_{MERIT}, b) TP_{SRTM}, c) $TP_{AW3D,}$ d) TP_{ALOS}

In Figure 3 erosion, susceptible areas scheme an assemblage of topography parameters (slope and dissection index)
Steep to very steep slopes with a high dissection index explain the higher erosion propensity expressed in the dark areas of Figure 3. At TPMERIT's 90-meter spatial resolution, the high erosion susceptibility zone covers about 9.20% of the Lebanese area.
The high erosion susceptibility zones consist of gentle to steep slopes with a moderate to high dissection index. Table 1 shows that high erosion susceptibility increases with the spatial resolution except at $TP_{SRTM,}$ the area susceptible to erosion occupies 6.46 % less space than TPAW3D with the same spatial resolution of 30 meters, and this difference is also discoverable in Figures 2.3b and 2.3c.
Moderate and Low erosion susceptibility areas decrease with the scale when the spatial resolution is higher. Otherwise, a stable zone covers almost 90% of the study area and is associated with lower slopes and a slight dissection index.

Table 2.1: Percentage of areas susceptible to erosion according to Topographic Parameters and Terrain Derivatives.

	TP_{MERIT}	TP_{SRTM}	TP_{AW3D}	TP_{ALOS}	TD_{MERIT}	TD_{SRTM}	TD_{AW3D}	TD_{ALOS}
Low	60.88	65.65	62.60	62.71	42.49	40.85	42.46	26.85
Moderate	30.02	27.89	27.23	26.99	28.56	28.75	28.03	33.68
High	9.10	6.46	10.17	10.31	28.96	30.40	29.51	39.47

The evaluation of topography parameters at all levels of detail has found that nearly all the relief parameters, slope angle (SA), and dissection index (Di) values are high between ridges and channels and low in plain areas such as Bekaa and Akar valleys. Higher relief supports prompt runoff; hence, it is directly related to soil erosion propensity (Phillips et al., 1999). More specifically, TP_{MERIT} occupied the higher area of ESA (39%) of the study area, which lies under the high SA and Di. Figures 3a, c, and d show the quantitative degree in the cartographic generation (change in scale) expressed in a difference of ESA area of 2% between TP_{MERIT} and TP_{ALOS}.
Topography parameters indicate the terrain's structural complexity associated with SA and DI and imply greater susceptibility to erosion.
Terrain derivatives have been done based on the four multiscale DEMs. Their spatial maps were prepared in a Geographical Information System (Figure 2.4).

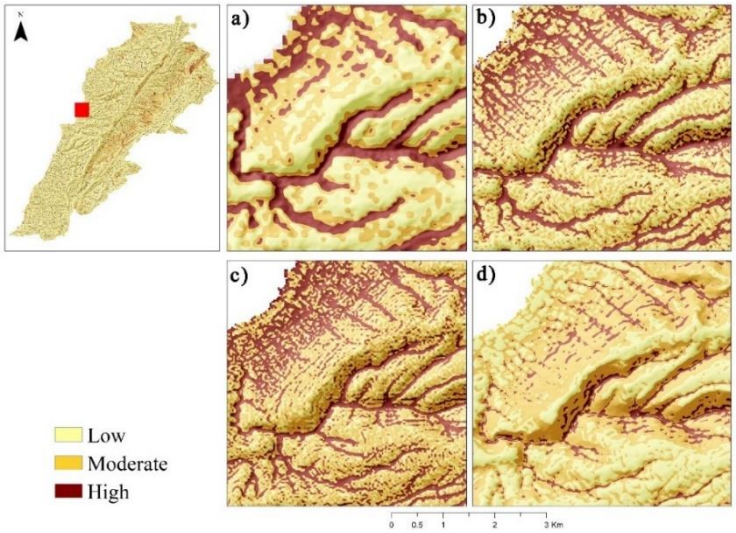

Fig.2.4 Erosion susceptible areas based on Terrain Derivatives, a) TD_{MERIT}, b) TD_{SRTM}, c) TD_{AW3D} d) TD_{ALOS}

The evaluation of the terrain derivatives LS, SPI, Kv, and TWI is directly related to the structure of the landforms and lithological characteristics. Significantly high LS, SPI, Kv, and TWI values are noticed in stream channels over the study area (Figures 4a, 4b, 4c, and 4d). This indicates high mountainous relief and runoff conditions, intensifying erosion mechanisms.

The multiresolution soil erosion susceptibility maps based on terrain derivatives of Lebanon show the relative potential areas to erosion, generated from fuzzy logic AND equation with weighted composite scores. The greater the susceptibility of erosion, indicated by high scores, and vice versa. The dark color zones of Figure 2.4 represent high receptiveness to erosion.

Figure 2.4a of TD_{MERIT} shows high values of ESA in channels and deep valleys and low values on the top of ridges

These results are due to higher TWI values representing depressions in the landscape, where water is likely to concentrate through runoff (Martínez & Correa, 2016).

Moreover, SPI high values indicating the erosive power in the water flow correspond to lower and concave shapes of the terrain and, therefore, present values of membership degree close to 1

TD_{SRTM} and TD_{AW3D} of Figure 2.4b and 2.4c are very similar in values and shape, which proves that Terrain Derivatives are only influenced by the spatial resolution, not the type of DEM. At large scales figure 2.4d of TD_{ALOS} shows ESA on cracks and high terrain amplitude zones

The percentage of areas in Table 2.1 of TD increases for high and moderate values, with the scale from small to large.

Kv values less than zero presented a low incidence of erosion risk and corresponded to concave terrain in the vertical direction to the slope, while the convex terrain had a higher incidence. Kv values influence flow acceleration, erosion, and deposition rate; a convex curvature accelerates the flow and erosion process, while a concave one has a big influence on the sedimentation process (Wilson & Gallant, 2000; Neteler & Mitasova, 2008; Kennelly, 2008).

Zhang and Montgomery (1994) investigated the effects of different DEM resolutions on the TWI and found that higher resolutions lead to lower TWI values. We found that all other terrain derivative parameters (LS, SPI, and Kv) are also influenced by spatial resolution, and their values increase with the scale increase.

The maps of Figures 2.3 and 2.4, based on topography parameters and terrain derivatives, demonstrate the qualitative classification of the areas susceptible to erosion.

The visual and quantitative analysis of multiscale TP and TD shows similarity in all datasets, with some differences due to the variation in spatial resolution.

A GIS combination algorithm combines the generated maps of topography and terrain derivative erosion susceptible areas into four final Erosion Susceptible Areas maps (ESA_{MERIT}, ESA_{SRTM}, ESA_{AW3D}, and ESA_{ALOS}).

The algorithm takes multiple input raster and assigns a new value for each unique combination of input values in the output raster, giving the highest values to areas of high erosion and the lowest values to areas of low erosion.

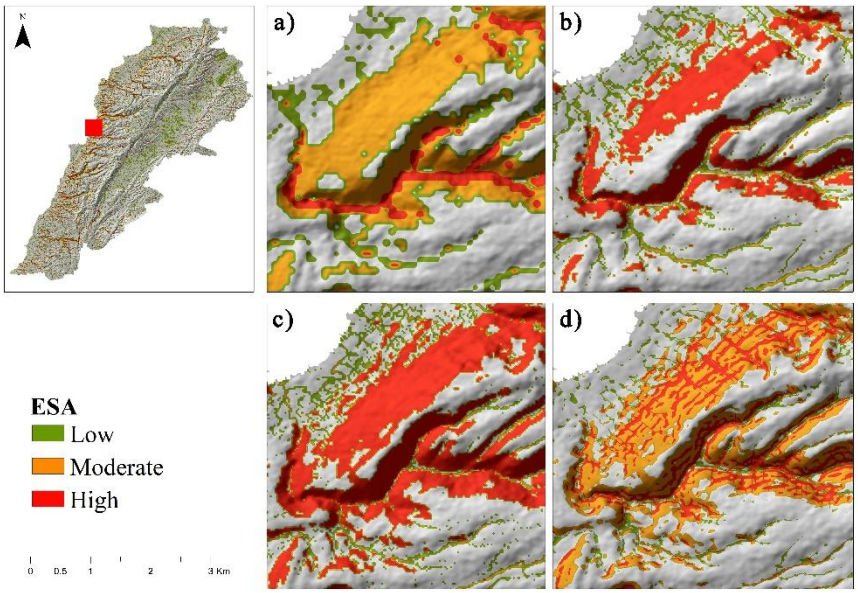

Fig.2.5 Erosion Susceptible Areas maps, a) ESA_{MERIT}, b) ESA_{SRTM}, c) ESA_{AW3D} d) ESA_{ALOS}

The resulting ESA maps illustrated in Figure 2.5a show a very high degree of ESA in channels and moderate ESA in convex breaks (between ridges and channels).
In ESA_{SRTM} and ESA_{AW3D} of 30 meters resolution, the high degree of ESA is found in convex breaks, and the low degree of ESA in the plain areas in another way in Figure 2.5d of high-resolution ESA_{ALOS} convex breaks have moderate and high degree of ESA, the evolution of ESA with the scale passed by two phases,1) spatial changes of high ESA from channels to convex breaks between ESA_{MERIT} and ESA_{AW3D}. 2) shape changes by the decrease of the high ESA surfaces between ESA_{AW3D} and ESA_{ALOS}.

Table 2.2: Percentage of areas susceptible to erosion.

	ESA_{MERIT}	ESA_{SRTM}	ESA_{AW3D}	ESA_{ALOS}
Low	79.88	82.99	80.03	83.24
Moderate	11.75	12.05	11.20	9.63
High	8.37	4.96	8.77	7.13

The quantitative analysis of ESA area percentages in Table 2.2 proves the evolution of the generalization from 8.37 % of high ESA degrees to 7.13%. The decrease in the area percentage of high ESA degree ESAMERIT to ESAALOS increases the low ESA area percentage.
To test the similarity between the multiscale erosion susceptible areas maps, a correlation analysis done in Figure 2.6

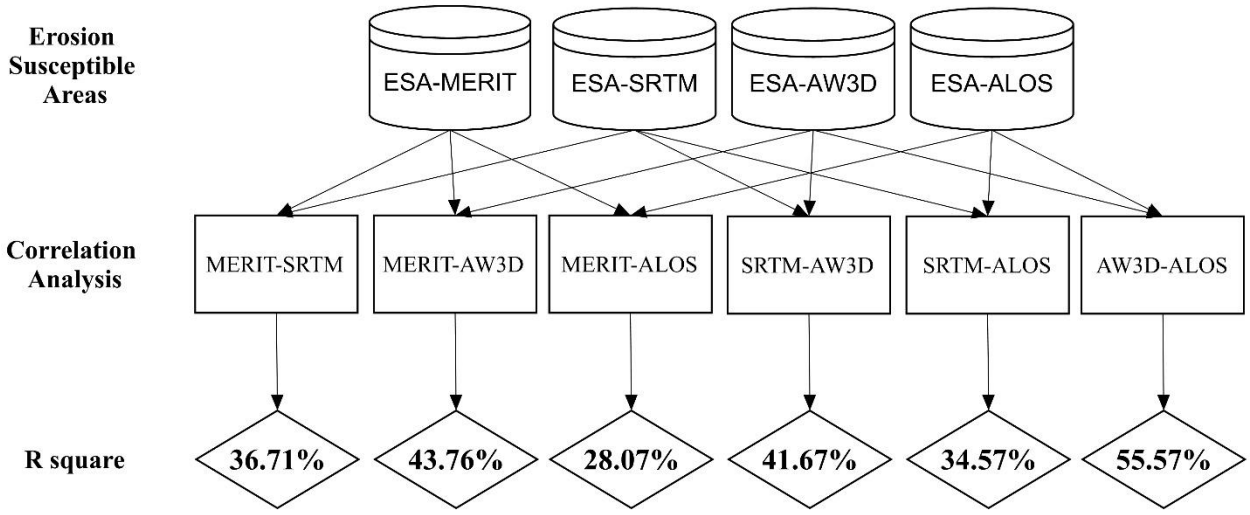

Fig.2.6 Correlation analysis schema between different scale ESA maps.

The correlation analysis schema begins from the four multiscale erosion susceptible maps generated from digital elevation models compared to each for the calculation of R^2.
There is a very low percentage of similarity between ESAMERIT and ESAALOS due to the difference in scale; the spatial resolution of ESAALOS is seven times smaller than that of ESA_{MERIT}.
The R2 values of ESASRTM and ESAAW3D with similar scales are 41.67%, which is not a high degree of similarity. Hence, the Erosion-Susceptible Areas depend on scales and defer to the type of data source (the way of DEM generation).
ESA_{AW3D} and ESA_{ALOS} had a higher degree of similarity of 55.57%, proved in the above visual and quantitative analysis in Figure 2.5 and Table 2.2.
The modeling of erosion-susceptible areas predicts the highest erosion in strongly convergent areas, indicating the creation of channels.
These results were due to the higher resolution of the ALOS DEM (12.5 m) and the better representation of the Earth's surface, which led to very high accuracy in defining the Erosion-Susceptible Areas.

CONCLUSION

The multiscale details of ESA required the application of a very precise quantitative model. Open-source high-spatial-resolution DEMs improve information on erosion and the level of detail of the information by using multi-spatial resolution. Calculating geomorphometric parameters facilitates understanding of the factors affecting erosion. Fuzzy logic provides a more realistic approach to the erosive phenomenon based on DEMs with considerable uncertainty.
The present chapter delineates the erosion areas of the Lebanese territory using the geospatial method, considering Topography and Terrain Derivative. The study revealed that almost (7%) of the area is potentially erosive; fuzzy logic in geosciences, more precisely ESA, has several advantages that improve conventional logic. We mentioned that digital modeling has many factors influencing data uncertainty in complex erosion processes; the fuzzy approach has a great potential for modeling Low and high-resolution DEMS.
Micro features increase and slow runoff, therefore, erosion at small scales. Thus, as DEM resolution and accuracy increase, erosion estimation will improve, and the landscape will be more accurately described.
Finally, we can conclude that erosion modeling depends on data source type and scale, which influence the shape and geometry of the Erosion-Susceptible areas.

Chapter 3

Multiscale Geometric Analysis of Ephemeral Gullies

The appearance of drones, the fast evolution in close-range photogrammetry, and its applications for digital surface extraction led to multiscale high-resolution terrain analysis. The scale is predominantly considered a function of the resolution of Digital Surface Models (DSM) (Hengl & Evans, 2009; Mac et al., 2009).

Pike et al. (2009) remarked that no digital elevation models derived map is definitive, as the generated parameters differ with algorithms and can vary with resolution and scale (Doumit, 2018).

Soil erosion from water runoff occurs predominantly through three processes: sheet erosion, rill erosion, and ephemeral gullying (Smith, 1993). Doumit and Awad (2019) analyzed the effect of multiscale DEM on the delineation of sheet and rill erosion, whereas, in this chapter, we focus only on ephemeral gullies (EG) erosion based on a multiscale drone-based DSM.

Ephemeral gullies are small channels eroded by concentrated flow in the exact location due to subsequent runoff events (Castillo et al., 2012).

Time series aerial photography and DEM were used to map gully erosion (Nachtergaele & Poesen, 1999; Ries & Marzolff, 2003; Parkner et al., 2006; Thorne et al., 1986; Martínez-Casasnovas et al., 2002). More recently, drone-based close-range photogrammetry and structure from motion (SfM), including different spatial scales, have been used in geomorphic studies (James & Robson, 2012; Turner et al., 2012; Westoby et al., 2012; Doumit& Kiselev, 2016). Close-range photogrammetry is based on computer visualization tools for three-dimensional surface reconstruction algorithms. Structure from Motion (SfM) creates massive point clouds based on pixel matching from which highly accurate digital surface models (DSM), and orthophotos can be derived (Doumit& Kiselev, 2016; James & Robson, 2012).

Several studies have documented the relationship between ephemeral gully formation and runoff erosivity using terrain derivatives, especially drainage area and local slope (Patton & Schumm, 1975; Thorne et al., 1986; Montgomery & Dietrich, 1994).

From the terrain derivatives, stream power is widely used to identify the location of ephemeral gullies, which depends on the "generation of concentrated surface runoff of sufficient magnitude and duration to initiate and maintain erosion, leading to channelization" (Thorne & Zevenbergen, 1984; Desmet et al., 1999). Plan curvature measures the degree of flow convergence along a flow path leading to an ephemeral gullies' formation model (Zevenbergen & Thorne, 1987). Zevenbergen (1989) describes five factors as influencing ephemeral gully formation, including:

1. Overland flow discharge and duration.
2. Slope and flow depth determine the magnitude of the flow's downslope.
3. Planform curvature determining the convergence of the flow.
4. Soil characteristics determine the erodibility of the soil.
5. Vegetation characteristics reduce soil susceptibility to erosion (Zevenbergen, 1989).

This study is based on drone DSM multiscale, and it focused only on topographic controls of overland flow influencing ephemeral gully development, considering only the first three Zevenbergen's terrain factors: discharge, slope, and plan curvature, which is the primary key of topographic controls in ephemeral gully formation process (Thorne et al. (1984).

Plan curvature as a second terrain derivative contributes to ephemeral gully formation in multiple ways: a) Convergence runoff and discharge are related to slope length to a power greater than unity (Zevenbergen, 1989).

b) plan curvature degree determines local flow geometry and the degree of flow concentration.

c) plan curvature represents the degree of concentration of stream power.

Thorne et al. (1986) used these parameters to calculate a Compound Topographic Index (CTI) to identify ephemeral gullies. Parker et al. (2007) tested the CTI model to predict ephemeral gully locations in a GIS environment for different sites. Moore et al. (1988) used two methods to estimate EG location: the slope area index and the wetness topographic index; Casalí et al. (2006) tested several methods for estimating ephemeral gullies and concluded that CTI is probably the most widely used approach for predicting ephemeral gullies' location.
After we presented the facts of the studies concerning the identification of ephemeral gully erosion, we submit the specific objectives of this chapter:

- to apply the work carried out by Zevenbergen and Thorne, utilizing Geographical Information Science (GIS) for multiscale ephemeral gullies delineation from CTI parameters.
- Compare and evaluate the impacts of multiscale expressions by drone flight heights on ephemeral gullies' geomorphological parameters (length, depth, and volume).

Our project is situated in the western chain of Mount Lebanon in the Zaarour region, covering an area of about 15 hectares. Mount Lebanon forms a barrier against rain movement and precipitations reaching more than 1400 mm yearly (Traboulsi, 2010).

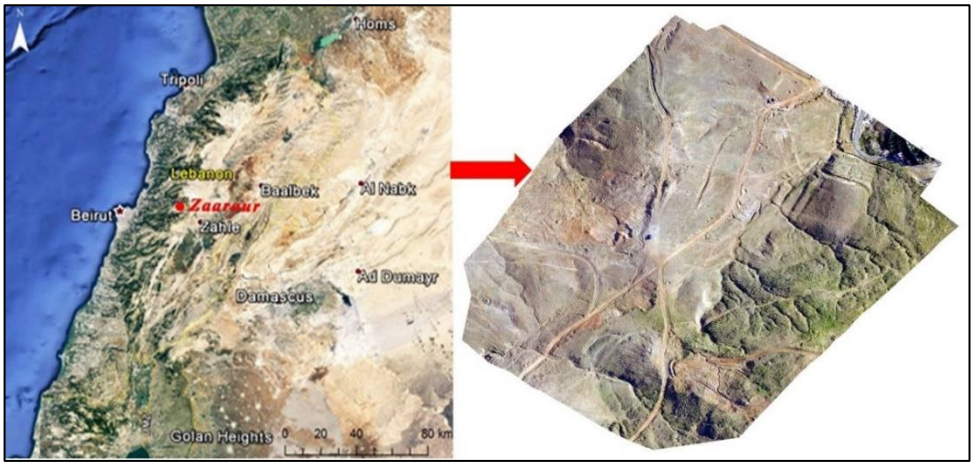

Fig 3.1 Google Earth Spatio-image of Lebanon and an orthophoto of the study area.

Several geological formations from the second era characterize the study area. The eroded and permeable formations of the Cenomanian (C4), Upper Aptian (C2b), Albian (C3), Lower Aptian (C2a), and Neocomian (C1) show effective physical water erosion (Dubertret, 1960).
The Zaarour area is characterized by light soil, mainly sandy and grayish clayey soils, and very limited limestone surfaces. Erosion and runoff are effective in sandy soils (Hakim, 1985).

MATERIAL AND METHODS

A DJI Phantom 3 drone with a 14-megapixel camera flew through the study area, capturing aerial images at different flight heights; the experiment consisted of three flight missions at 120, 240, and 360 meters (FH-120, FH-240, and FH-360).
Flight planning was designed using a mobile application called DJI ground station based on Google Maps images; the flight height's datum was the same as the drone takeoff point for all missions.
The flight path followed by the UAV was identical for all the flights FH-120, FH-240, and FH-360. After drawing flight paths for all missions, the camera shutter interval was set to 2 seconds in the DJI ground station application. The acquired images overlapping was set at 80 % and side lapping at 70%.
The flight missions' photogrammetric processing was completed using Meta shape Photo scan, a Russian photogrammetric software. The processing workflow begins with stitching derived aerial images and then produces point clouds, 3D mesh interpolation, Digital Surface Model (DSM), and Digital Ortho Model (DOM) generations.

Throughout the assessment, we used this drone to acquire aerial images and generate and interpret Digital Surface Models (DSM) and Digital Ortho Models (DOM) by applying structure from motion technology.
A three-processed DSM and DOM from different flight heights with several spatial resolutions: FH-120, at 120 meters' flight altitude, with a high resolution, highlighted all the terrain details, even rocks' texture. Passing by FH-240, the terrain is smoothed with some concave and convex areas, ending with FH-360, which has a very low spatial resolution and a very smoothed terrain of 360 meters' flight height.

Table 3.1: DSM and DOM spatial resolution at different flight heights.

Flight height	120 m	240 m	360 m
DSM	10 cm	20 cm	30 cm
DOM	5 cm	10 cm	20 cm

As per the table, a different flight altitude leads to different spatial resolutions (pixel size). As per the photogrammetry law, the higher the flight height, the smaller the scale. The minimum spatial resolution for DOM is 5 cm, which expresses a high level of details showing ephemeral gullies traces, and 10 cm DSM for accurate terrain analysis.
The generated DSM provides the critical data for calculating the Compound Topographic Index from terrain derivatives, such as slope, upstream drainage area, and plan curvature.
Thorne et al. (1986) introduced the compound topographic index model (CTI) to measure stream power to erode soils. CTI considers topographic attributes such as slope, upstream drainage area, and plan curvature as topographic controls in the formation process of ephemeral gullies (Daggupati et al., 2013). The CTI is defined by:

$$\mathrm{CTI} = \mathrm{A} \times \mathrm{S} \times \mathrm{PC} \qquad (1)$$

where: A = upstream drainage area, S = slope and PC = plan curvature.

The resulting positive CTI values were only considered ephemeral gully since negative values result from negative plan curvature (ridges). Maps of positive CTI values were generated for the flight heights of 120m, 240m, and 360m (Figure 3.2).

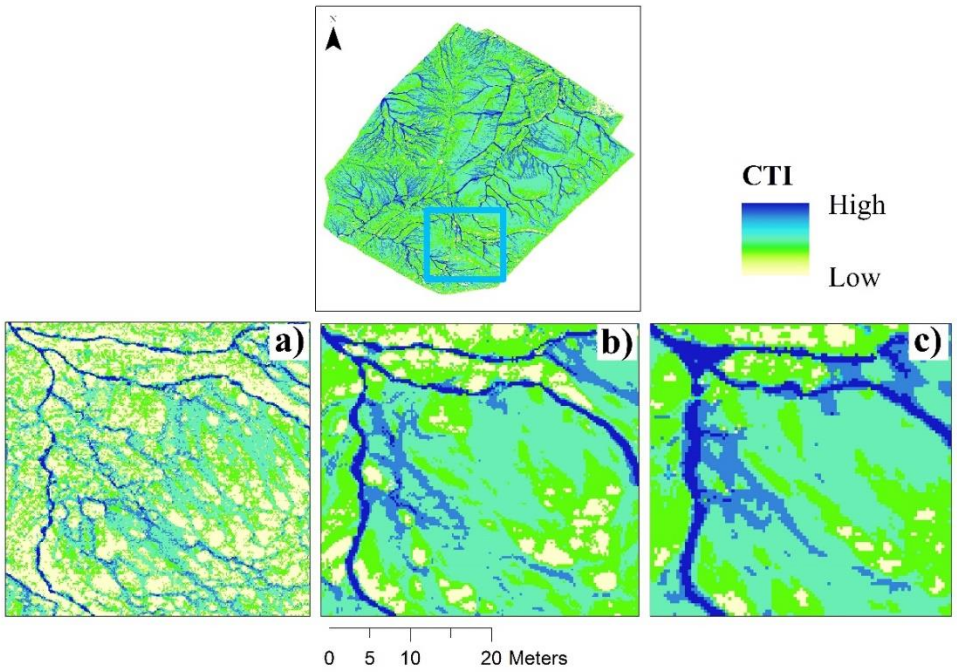

Fig.3.2 a) CTI map of flight height 120, b) CTI map of flight height 240, c) CTI map of flight height 360.

Many studies concluded that DEM resolution substantially affects topographic attributes and model results (Doumit, 2018; Holmes et al., 2000; Chaubey et al., 2005; Parker et al., 2007; Momm et al., 2011).
the impacts of DSM resolution (10 cm, 20 cm, and 30 cm) on the performance of CTI were evaluated by the delineation of ephemeral gullies in three different scales EG_{120}, EG_{240}, and EG_{360}, with an output of different percentages of areas (1.2 %, 3.2%,3.8%)
The main morphological characteristics of the delineated EG are its length, depth, and volume. These provide a better understanding of the soil volume that can be transported within a channel (Nachtergaele et al., 2001).
From the hydro tools GIS algorithm and each DSM, we calculated flow direction, flow accumulation, and streamlines (Figure 3.3). These generated streamlines were draped on ephemeral gully shapes for the EG length calculation.
The three levels of DSM are cropped using the EG shapes to calculate the depth and volume of each pixel in the raster data format. The spatial resolution of all DSM and the height, depth, and volume are trigonometrically calculated in a raster.

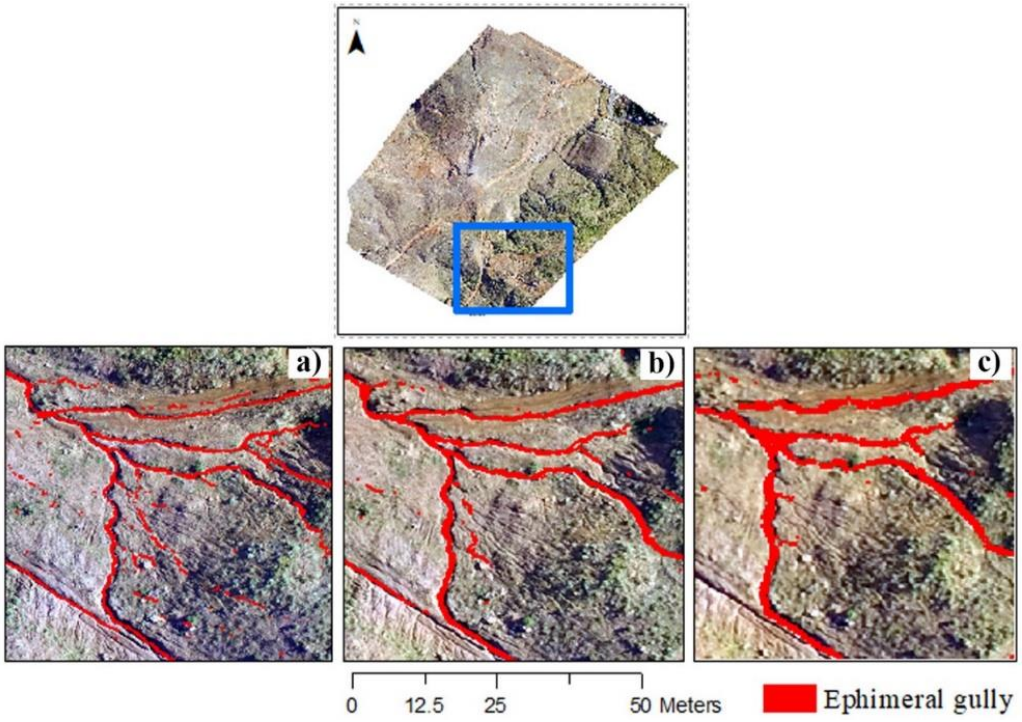

Fig.3.3 a) EG map of flight height 120, b) EG map of flight height 240, c) EG map of flight height 360.

RESULTS AND DISCUSSIONS

After delineating EG from the positive CTI values, Figure 3.3 shows a scale series of CTI maps highlighting EG in dark colors, and the small area of EG120 is due to the thin channels generated from high spatial resolution Figure 3.3a. With the change in flight height, gully channels became thicker, and their areas became more considerable, as shown in the higher flight results of EG_{240} and EG_{360}.
To understand the effect of CTI values with the scale, we calculated the statistics of CTI values inside each of the gully shapes EG_{120}, EG_{240}, and EG_{360}. Table 3.2

Table 3.2: CTI statistical values

	Min.	Max	Mean
EG_{120}	-18.06	7.56	-14.78
EG_{240}	-18.06	7.55	-14.12
EG_{360}	-18.06	7.54	-13.76

Table 3.2 shows statistical CTI values within gully shapes. It shows identical minimum values in all scales and a decrease in maximum values with decreased spatial resolution (pixel size).
From the Ephemeral gullies CTI delineation, we can understand that the thickness of gully channels decreases with spatial resolution, resulting in a difference in areas and CTI values and influencing research results.
We calculated each EG shape's geometrical characteristics (length, depth, and volume) after EG delineation. Multiscale ephemeral gullies were classified based on depth (GD). Table 3.3 describes small, medium, and large gullies and is commonly used in erosion manuals.

Table 3.3: Gully classes based on depth

Gully depth percentage of area			
Interval (m)	GD_{120}	GD_{240}	GD_{360}
0-1	85.72	83.04	80.13
1-2	9.05	12.50	15.31
>2	5.22	4.44	4.55

As per Table 3.3, small gullies occupied more than 80% of the gullies' total area. The percentage of the area of medium gullies increased with the flight height; otherwise, the areas of small and large gullies decreased.
The results of the morphological characteristics statistics of Table 3.4 show that pixel quantities decrease with flight heights, and gully length increases with flight height due to the decreasing spatial resolution of raster data formats having gully length as pixel values.

Table 3.4: Statistics of multiscale Morphological characteristics

Morph. Charc.	E.G.	Pixel	Mean	Std Dev	Skew.	Kurt.	Max.	75% M.	50% M.	25% M.	Min.
Gully Length (m)	120	118957	0.01	0.023	4.161	22.47	0.235	0.01	0.002	0	0
	240	89664	0.089	0.122	2.618	8.74	0.91	0.12	0.044	0.011	0
	360	47187	0.117	0.151	2.07	4.872	0.967	0.162	0.054	0.015	0
Gully Depth (m)	120	118957	0.302	0.656	2.11	3.12	2.679	0	0	0	0
	240	89664	0.354	0.674	1.786	1.874	2.619	0.341	0	0	0
	360	47187	0.387	0.698	1.584	1.079	2.613	0.507	0	0	0
Gully Volume (sq.m)	120	118957	0.004	0.009	2.11	3.13	0.038	0	0	0	0
	240	89664	0	0	2	2	0	0	0	0	0
	360	47187	0	0	2	1	0	0	0	0	0

At EG_{120}, the gully length skewness tends to the left with high kurtosis toward the low-length EG pixels; otherwise, at EG240 and EG360, gully length skewness values tend to the right near the pixels of mean length values.
The mean gully depth values differ from EG_{120} to EG_{360} by 8 cm, influencing standard deviation and skewness depth values approximately in the same order.
Gully volume is calculated in square meters, and due to small gully volumes in pixels of low spatial resolution, EG_{240} and EG_{360} statistical values are rounded to zero.
To solve this issue, we graphically represented gully length and volume values on a Log histogram for EG_{120}, EG_{240}, and EG360 in Figures 3.4, 3.5, and 3.6.

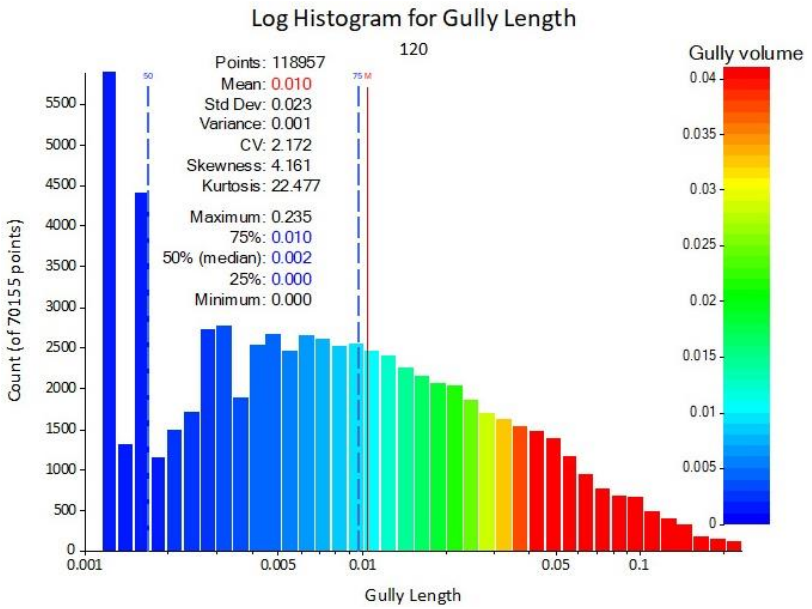

Fig.3.4 Log histogram of gully length and volume of the flight height 120

At EG_{120}, 50% of the median goes for the small-length gully less than 0.002 m. The 75% median is approximately equal to the mean of the gully length value of 0.01 m, which means most of the pixels have small-length values due to the high spatial resolution. High gully volumes are detected in pixels of high gully length, with a maximum length of 0.235 m and 0.038 sq. meters. High EG volume begins at 0.04 m EG length.

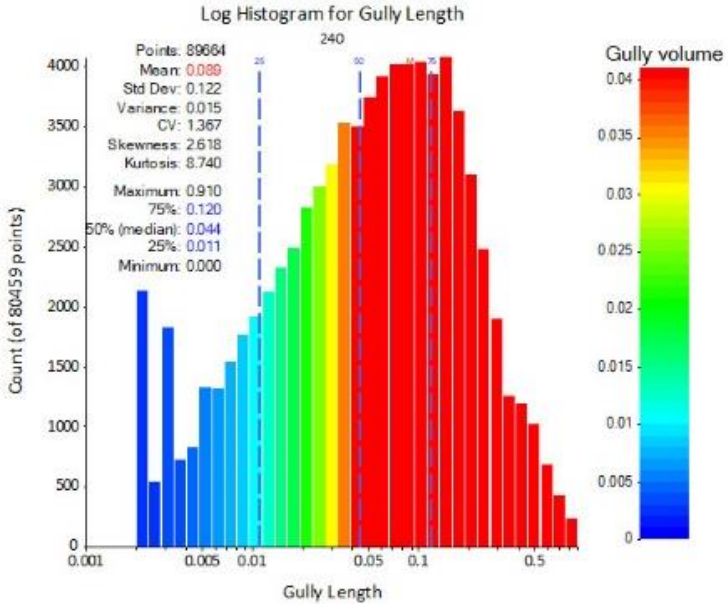

Fig.3.5 Log histogram of gully length and volume of the flight height 240 m.

For EG_{240}, the 50% median of gully length between 0.011 and 0.044 m is approximately two times bigger than the results of EG_{120}; also, the mean value of gully length is two times bigger than the 50% median value.

A high gully volume of 0.04 sq. m is between 0.04 m and 0.91m of gully length and near the 50% median of the EG length value.

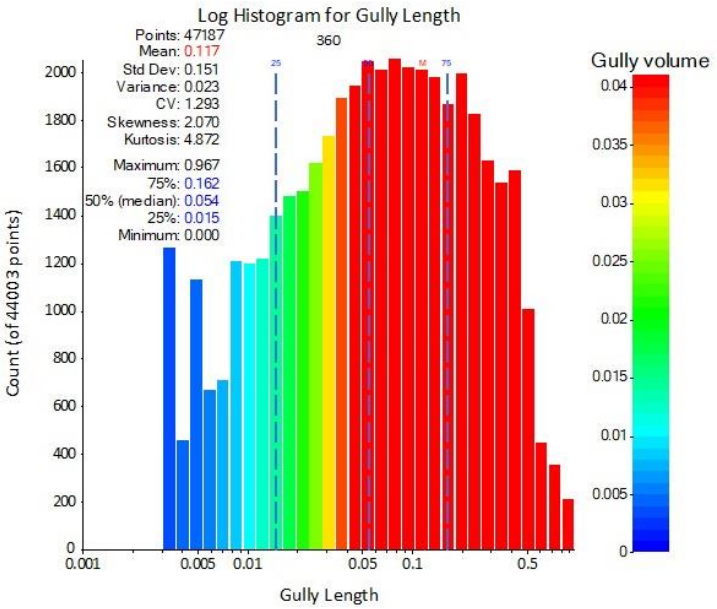

Fig.3.6 Log histogram of gully length and volume of the flight height 360

The Log histogram of Figure 3.6 of EG_{360} with the low spatial resolution is very similar to the Log histogram of EG_{240} with a slight shift in the degree of 0.028 m in EG mean length values between the two datasets.

A high gully volume of 0.04 sq. m is between 0.035 m and 0.96m of gully length and near the 50% median of the EG length value.

From Table 3.4 and the histograms of Figures 3.4, 3.5, and 3.6, we can see that EG240 and EG360 have very similar values, not like the values of EG120. This is due to the dataset's high spatial resolution.

We can say that there is a scale transition from relief to micro-relief between EG_{240} and EG_{120}, and there is a presence of two scales: a small-scale ephemeral gully expressed by the flight heights 240 and 360 m and a much smaller scale in the level of microrelief of the flight height 120 m.

CONCLUSION

Drone Digital Surface Models (DSM) at different flight heights were used as input data, and the Compound Topographic Index was applied to delineate the ephemeral gully at three flight heights: 120, 240, and 360.

A methodology for applying Thorne and Zevenbergen's (1990) CTI technique within a GIS environment has been achieved.

This is an essential step as it demonstrates the potential for incorporating the CTI approach into drone-based DSM's digital terrain analysis tools, allowing the delineation of ephemeral gully channels. The CTI is a rational equation that predicts the potential for ephemeral gullying based on local values of specific stream power.

The results of this paper have demonstrated that the elevation grid resolution influences the CTI predictor's performance. This demonstrates a need for more widespread availability of accurate elevation data before applying the CTI technique.

Also, results show that the effect of cartographic generalization on scale change is very high between flight heights of 120 m and 240m due to the big difference in the areas of ephemeral gullies.

Ephemeral gullies extracted from drone DSM and GIS quickly presented results and discussion by integrating the geospatial multiscale approach.

The information and methods discussed in this paper provide valuable results for cartographic multiscale studies of ephemeral gullies. Areas and shapes of EG are dissolving as scales compete, some gaining areas and some disappearing.

The morphological characteristics of ephemeral gullies in terms of length, depth, and volume show a big similarity in values of EG240 and EG360 and very different values from those of EG120 due to the high spatial resolution. These results highlight the presence of two scales: a small-scale ephemeral gully expressed by the flight heights of 240 and 360 m and a much smaller scale in the level of microrelief of the flight height of 120 m.

Future studies may apply scaling techniques, including other factors such as land cover, precipitation, and soil type, which would likely improve EG model performance and may help simulate ephemeral gullies.

Chapter 4

Multiscale Analysis of Digital Surface Models

In geoinformatics, scale is predominantly considered a function of the resolution of Digital Elevation Models (DEMs) (Hengl & Evans, 2009; Mac et al., 2009).
Technological progress, especially unmanned aerial vehicles (UAV) and new photogrammetry software encourages acquiring and processing Digital Surface Models (DSM) at ever finer resolutions. The scale dependency of land-surface parameters was noted by Evans (1972) as «a basic problem in geomorphometry» (Shary et al., 2002). Meanwhile, the scale dependency of land-surface parameters and land-surface objects has been confirmed by several researchers (Chang & Tsai, 1991; Wood, 1996; Florinsky & Kuryakova, 2000; Evans, 2003; Hengl, 2006; Arrell et al., 2007; Deng et al., 2007; Pogorelov & Doumit, 2009; Wood, 2009).
Measurement: Scale and resolution are essential in using digital models in GIS research. The scale may range from micro to macro and at different measurement levels. This chapter will only discuss the spatial scale with the UAV flight Heights. The selection of an image with an appropriate spatial resolution for a study demands the examination of the characteristics, especially the changing pattern as a function of changes in scale and resolution.
As per Li and Zhilin (1993), based on different kinds of philosophy, three types of approaches can be identified to the generation of multi-scale representations for a given DTM (Digital Terrain Model): critical-points-based, smoothing-based, and scale-driven (Li, 1993).
Woodcock and Strahler (1987) suggested using the local variance method to find images with the optimum scale and resolution.
In their experiment, Woodcock and Strahler (1987) used image data that were degraded to coarser spatial resolution by resampling the neighbors' cells, and the pixel value of the coarse resolution is an average of a group of finer resolution. Our experiment has 6 DSM for the same study area with different spatial resolutions obtained from UAV different heights survey. The effect of scale (spatial resolution) on these surface models is analyzed according to the morphometric indices by calculating their direct indicators of spatial correlation. Therefore, the experiment implemented the opportunities for multi-scale measurement technology based on UAVs.
For multi-scale analysis, we applied Wood and Strahler's (1987) method of Local Variance, the texture method measuring surface properties such as coarseness and smoothness, and as a third index of fractal dimension.

STUDY AREA AND DATASETS

Our experimental research was carried out on an area of about 2 hectares at a relative altitude of 1700 meters above sea level in the Zaarour region, situated on the western Lebanese mountainous chain (Figure 4.1). We chose this bare, unurbanized mountainous area because of its representative morphological terrain forms.
The study area has a slight natural slope, represented by bare lands with elements of anthropogenic relief. Anthropologic micro-relief was included in the study area due to the representativeness requirements and the complicated microform for the experimental modeling of the terrain concave and convex smoothed areas.

Fig 4.1 Spatio-map of Lebanon showing the study area of Zaarour region (Google Earth).

An autopiloted Dji Phantom 3 Unmanned aerial vehicle (UAV) with a camera of 14 megapixels at a focal length of 3.61 mm flies the study area at different Heights. The flight Heights are measured from the quadcopter's takeoff point; the experiment constituted six missions: FA-20, FA-40, FA-60, FA-120, FA-240, and FA-360 of 20, 40, 60, 120, 240, and 360 meters in height. The quadcopter's flight path was identical for all the flights, and it was designed in a mobile application called Litchi (Figure 4.2). The printed screen of the Litchi application, Figure 4.2, shows the quadcopter's flight path, the study area, and the flight parameters (coordinates, height, time, etc....). All datasets (photos) of the six missions of different flight heights were processed in Agisoft photo scan software to extract Digital Surface Models (DSM).

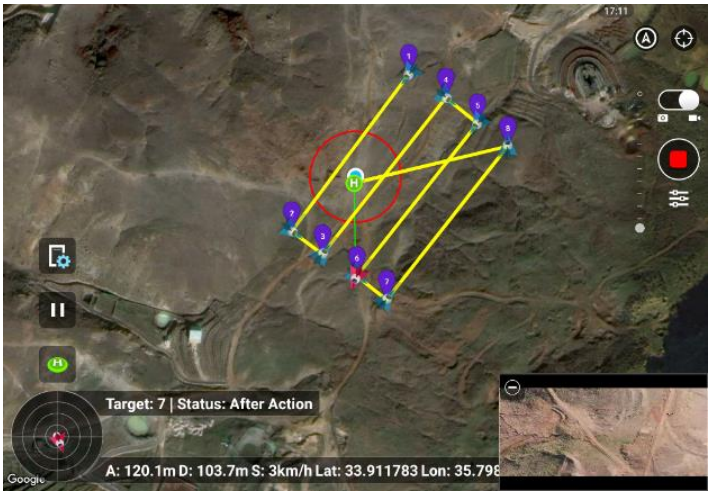

Fig 4.2 The designed path of the six missions.

If the camera focal length and the flying Height of the UAV are known, the scale is determined by this formula:

$$\frac{1}{S} = \frac{f}{H}$$

With S =scale, f = focal length of the camera, H= flying height.
The result of scale calculations for each flight Height is listed in Table 1.

Table 4.1 Each DSM type's spatial resolution, calculated scale, and approximated scale.

DSM	Spatial resolution (m)	Calculated Scale	Approximated Scale	Category
FA-20	0.37	1/5540	1/5000	Plans
FA-40	0.55	1/11080	1/10000	
FA-60	0.80	1/16620	1/15000	
FA-120	1.73	1/33241	1/30000	Maps
FA-240	3.20	1/66481	1/60000	
FA-360	4.47	1/99722	1/100000	

Figure 4.2 shows six DSM of the study area of different spatial resolutions: FA-20 of 20 meters flight Height with a very high-resolution data set highlighting all the terrain details, even rock textures, passing by FA-60 and ending by FA-360 of 360 meters flight Height with a very low spatial resolution and high generalization effect with the «disappear» and «growth» of some terrain morphological features.

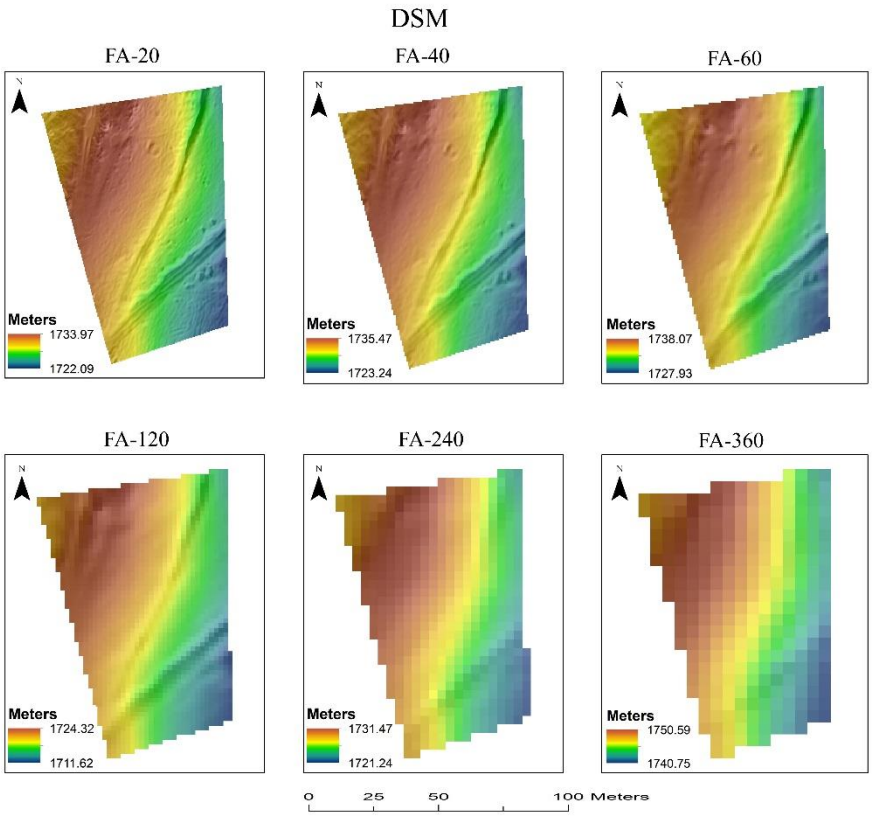

Fig.4.3: Multi-scale DSM extracted from UAV photogrammetry methods.

These 6 DSM can be visually classified from Figure 4.3 as rough and smooth: FA-20, FA-40, and FA-60 for rough and FA-120, FA-240, and FA-360 for smooth. Also, Figure 4.3 constitutes an interval of scales and smoothness, showing the generalization at different scales.

As per Table 4.1, different flight Height led to different spatial resolutions (pixel size); the minimum spatial resolution is 0.37 m, which is high enough to show all terrain details, and the maximum resolution is 4.47 m, which is quite good for geomorphological analysis at a local scale. After the scale calculation, we categorized our data into two categories: plans and maps. The first three DSM of flight Height 20, 40, and 60 are related to the category of plans, and the others are related to the category of geographical maps.

MATERIALS AND METHODS

Many scientists quantitively discussed the optimal resolution of digital elevation models. Our study summarized the methods expressing the relation between UAV flight Height and spatial resolution: local variance, texture analysis, and the fractal method. The first two methods are relatively simple and very useful in a practical sense, while the third fractal dimension method has great potential in detecting the resolution effects and is used especially in several geoscience types of research.

The local variance method proposed by Woodcock and Strahler (Woodcock et al. A H. 1987) is such a method, originally developed in image analysis, with the potential for dealing with scale in DEM analysis (Li, 2008). Local variance measures the mean of standard deviation within 3 by 3 pixels in a moving window; the mean of all local standard deviation values over the entire image was then used as an indicator of local variability contained by the image.

The local variance is the degree of similarity between the values of two points depending on their spatial distance. The longer the distance, the higher the degree of similarity and the smaller the variance.

According to Schmidt and Andrew (2005), the land surface is hierarchically structured and can be represented differently across scales; for example, a convex hillslope can be embedded into a concave hillslope, which can be bedded into a valley. These cases can be detected and seen only on high spatial resolution DSM and are homogeneous relative to scale levels.

In Figure 4.4, the variance maps of the study area at FA-20 show all morphological forms in detail, even slight concave and convex forms with some finesse in FA-40; the same forms became bigger in size and dimensions. In the last stage of plan categories FA-60, the ridges boarding the roads became more highlighted with the disappearance of the small morphological forms. Hence, in the second category of scales FA-120, FA-240, and FA-360, the degree of smoothness increases with the scale.

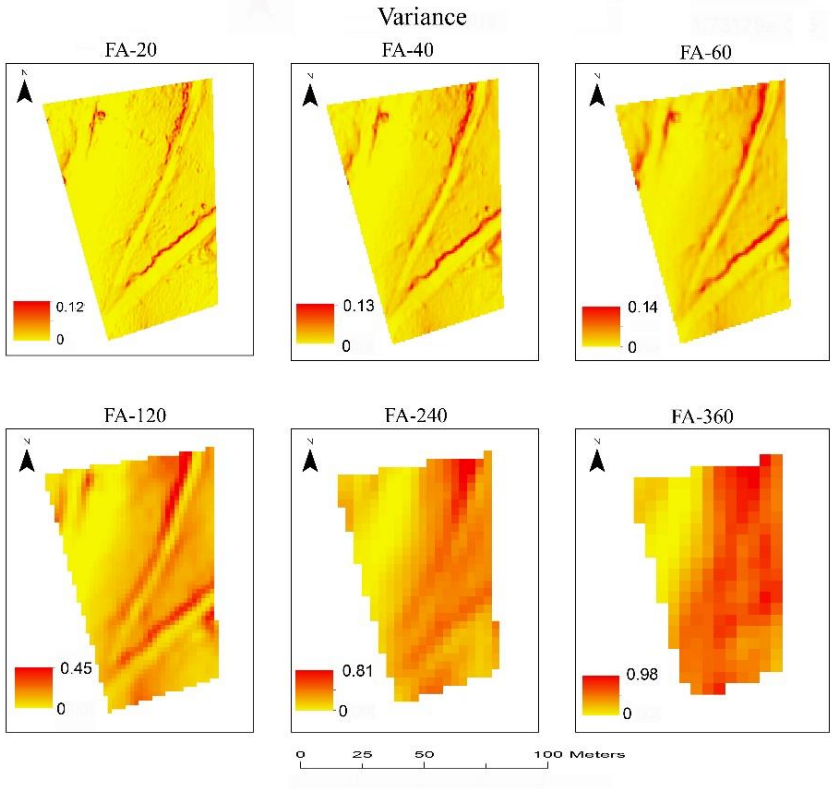

Fig 4.4 Variance digital models of the six-flight Heights.

The texture is a measure of coarseness, smoothness, and regularity of the surface (Gonzalez & Wintz, 1987); texture analysis can measure the spatial variability of image data and can improve the statistical separation of the otherwise similarly reflecting surfaces (Nellis & Briggs, 1989). The differences in texture for images covering the same area with different scales and resolutions (the case of our study) can indicate the heterogeneity of the scene under observation (Nellis & Briggs, 1989). In that way, we can compare the data; in this case, the highest texture index indicates the highest variation.

Texture is calculated by extracting grid cells that outline the distribution of valleys and ridges. Each grid cell value represents the relative frequency (in percent) of the number of pits and peaks within a radius of ten cells (Iwahashi & Pike, 2007).

Like local variance methods, the texture analysis method is also based on the variability of the geographic data change of scale and resolution. The scale at which the maximum variability occurs is where most of the relief formation processes operate. By finding the maximum variability of the dataset, we could find the operational scale of the geographic phenomenon and, therefore, decide the observational scale of the study.

The texture index in Figure 4.5 shows stability in the morphological forms in the first three scales and an unclear form in the last three scales. Consequently, the first three scales allow us to determine the Genesis of the relief-forming processes.

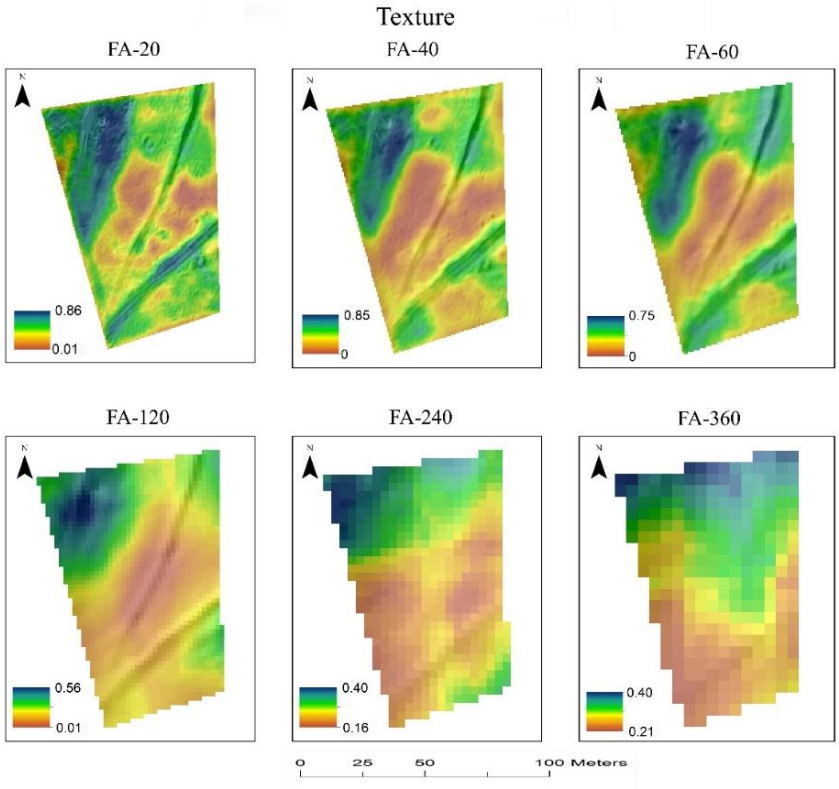

Fig 4.5 Texture digital models of the six-flight Heights.

Fractal dimension: Fractals fascinate geographers because all-natural patterns are too irregular and fragmented to be quantified using the traditional measure of geometric shapes. In the real world, curves and surfaces are pure fractals, so fractals could be important in detecting the scale and resolution effects in remote sensing and GIS.

Eastman (1985) developed a single-pass technique for measuring the fractional dimension of lines. The procedure considers each slope segment to provide evidence of an underlying angularity that can be considered as the generating angle of the fractal form. The formula is based on calculated slopes as follows:

$$D = \frac{\log(2)}{\log(2) + \log(\sin(\frac{180 - slope}{2}))}$$

We applied Eastman's method to calculate the fractal dimension of the six DSMs (Figure 4.6). As it is known, surface fractal dimension values vary inside the interval between 2 and 3. Empirical studies indicate that the fractal dimensions of curves and surfaces change with scale and resolution. The scale at which the highest fractal dimension is measured may be the scale at which most processes operate (Goodchild & Mark, 1987; Lam & Quattrochi, 1992).

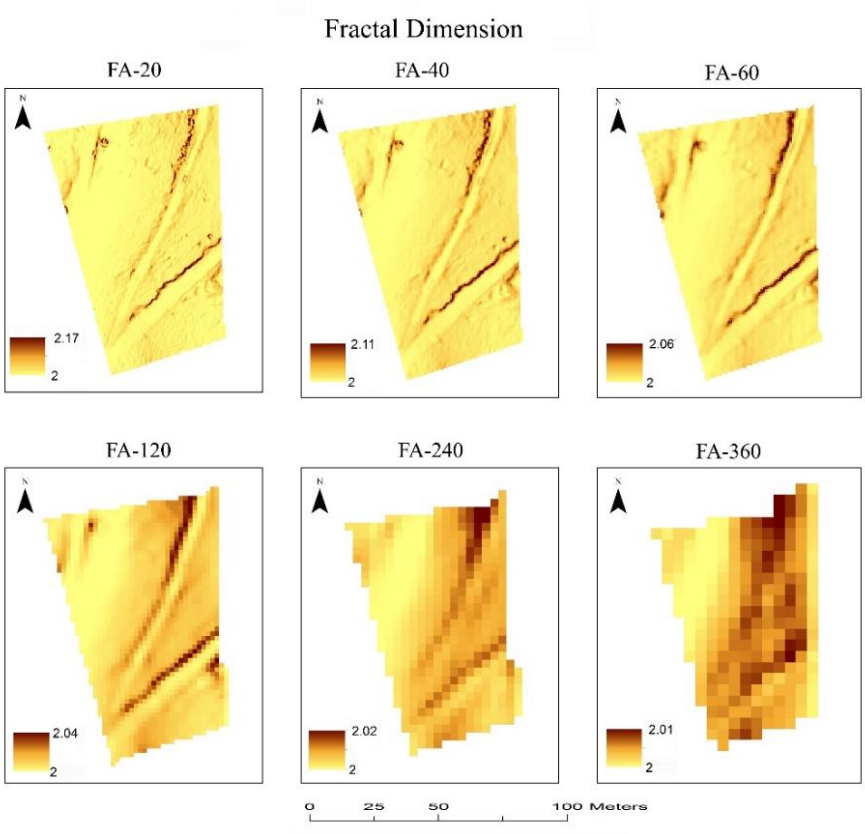

Fig 4.6 Fractal dimension digital models of the six flight Heights.

The fractal dimensions show roughness and complexity. Goodchild (1980) found that the fractal dimension could be used to predict the effects of cartographic generalization; many scientists used fractals to characterize landscape environmental data, soil, and topography (Burrough, 1983; Mark & Aronson, 1984; Pogorelov & Doumit, 2009).

The fractal dimension of an image is expected to be lower as the resolution becomes coarser; because coarser resolution is likely to result in low variability in digital surface models, it is argued that the best resolution level for a study is the one that has the highest fractal dimension within a stable scale range, the results of fractal dimensions calculations shown on figure 4.6.

If we compare Figure 4.4, which shows the local variance index maps, with Figure 5.6, which shows fractal dimensions, a high degree of similarity is seen, which indicates the usefulness of using indices in this analysis.

RESULTS AND DISCUSSIONS

After the three scale indices are applied to the six levels of detail, a statistical table summarizing the generalization between them is created.

Table 4.2 Local variance, texture, and fractal dimension statistical values over the six DSM's

DSM	Local Variance				Texture				Fractal Dimension			
	Min*	Max	Mean	STD	Min	Max	Mean	STD	Min	Max	Mean	STD
FA-20	0	0.129	0.005	0.007	0.189	0.864	0.457	0.170	2.0	2.179	2.008	0.011
FA-40	0	0.136	0.010	0.012	0.000	0.851	0.337	0.182	2.0	2.112	2.008	0.009
FA-60	0	0.143	0.015	0.017	0.000	0.75	0.333	0.157	2.0	2.067	2.006	0.007
FA-120	0	0.458	0.088	0.065	0.009	0.561	0.221	0.125	2.0	2.042	2.007	0.006
FA-240	0	0.811	0.222	0.141	0.160	0.408	0.252	0.059	2.0	2.023	2.006	0.004
FA-360	0	0.985	0.414	0.231	0.211	0.401	0.295	0.050	2.0	2.016	2.005	0.003

*Min – minimal value, Max – maximum value, mean – mean of the values, STD – standard deviation of the values.

The local variance maximum values increase with flight Height and scale, and the standard deviation and mean increase proportionally in all scales. Contrary to local variance values, the maximum, mean, and standard deviation of texture and fractal dimensions decrease with flight height and scale because of the smoothing effect.
We applied spatial correlation, a simple and effective tool, to determine the spatial distribution of the analyzed indices at different scales.
Figure 4.6 shows correlation scatterplots of each DSM's elevation values compared to the main DSM, the FA-20. We can see a good correlation between FA-20 and FA-40 (coefficient of determination R^2 equals 78.7%), which decreases between DSM FA-20 and FA-60 (R^2=65.4%).
The scatterplots of the last three levels show a very poor similarity compared to FA-20. They show a lack of connection between DSM at various scales. This means we are losing accuracy and have a big generalization lost in the maps category built using the UAV. Similar results were obtained when comparing the estimated parameters of the texture.

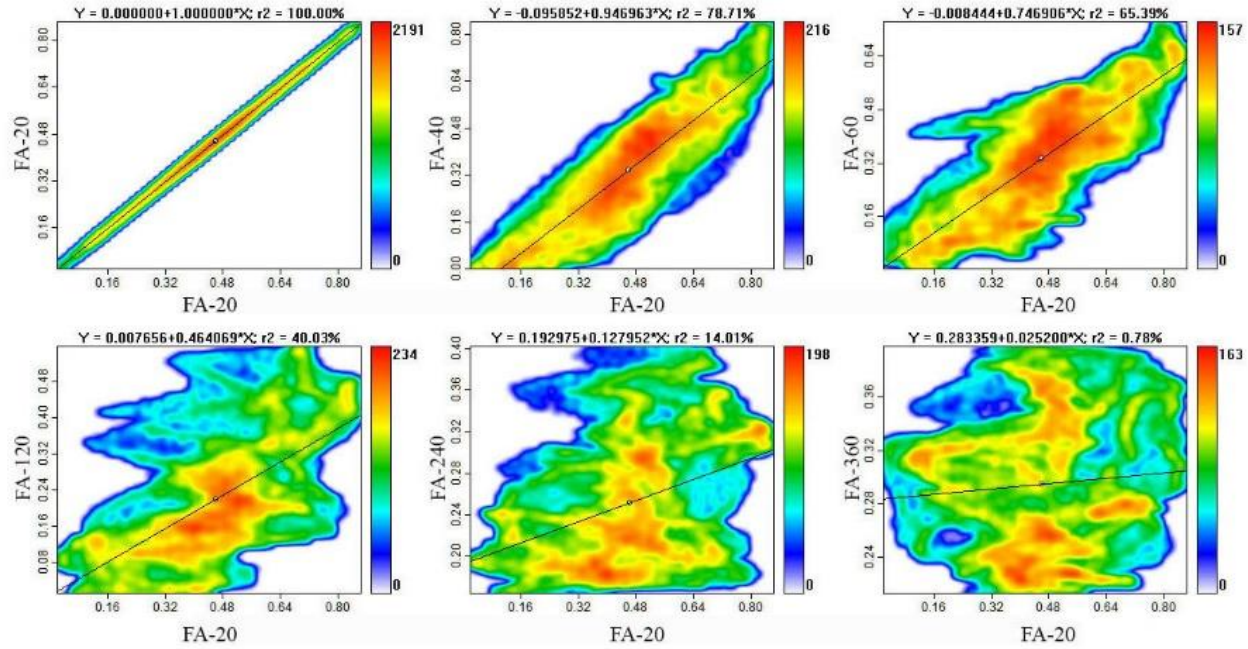

Fig. 4.7 Correlation scatterplots of the DSMs values.

When interpreting the values of local variance, we consider the following: If the spatial resolution is considerably finer than the objects in the scene, most of the measurements in the image will be highly correlated with their neighbors, and the local variance will be low. If the objects to be studied approximate the size of the resolution cells, the value tends to differ from each other, and therefore, the local variance increases. The resulting correlation values in Table 4.3 of DSM and texture are decreasing proportionally with the scale; otherwise,

Table 4.3 Correlation analysis values between different scales of different indices.

	Values of R2%			
DSMs	DSM	Fractal	Local Variance	Texture
FA-20/FA-40	78.71	63.9	71.79	78.68
FA-20/FA-60	65.39	24.95	25.09	65.28
FA-20/FA-120	40.03	27.04	26.07	39.49
FA-20/FA-240	14.01	20.72	18.39	13.15
FA-20/FA-360	0.78	13.55	11.89	0.79

FA-20/FA-120 at fractal and local variance constitute a barrier of values due to a raised amplitude in R2 values, which gives a similarity in scale changes between fractal and local variance in one way and another between DSM and Texture.
The correlation between the values of the local variance is statistically reliable (significant) only for the DSM with a spatial resolution close to FA-20 and FA-40. For cases with large differences in spatial resolution, these indices become essentially independent on the same site.
We can conclude that the correlation in local variance decreases with flight Height.

CONCLUSION

Drones are a relatively new survey instrument for the earth's surface and DSM processing. For a representative area in the mountains of Lebanon, drone experiments have been performed with variable flight heights (scale), DSM processing, and calculation of derived morphometric indices. Scale and resolution effects have been and will continue to be important issues in geographic research. A good understanding of the scale's effects on analysis results is essential. In this paper, we tested three morphological indexes (local variance, texture, fractal dimension) that can be used to detect scale and resolution effects.
The results showed a weak relationship of spatial characteristics when comparing the images to scale plans and maps. Simultaneously, the survey showed that the local variance and texture characteristics are good indicators of the optimal spatial resolution of the morphometric analysis of the earth's surface.

Chapter 5

Multiscale Evaluation of Geomorphological Surface Textures

Surface roughness could be defined as a value ranging between smooth and complex surfaces; this chapter specifically focuses on the broad area at different scales of general geomorphology (Evans, 1729) and, more explicitly, on the quantification of surface-roughness variability using Digital Surface Models (DSMs) generated from UAV. Surface roughness is treated here as a geomorphometric variable influencing the physiography of the terrain, not as a parameter due to the precision and accuracy of the generated digital surface models.

Measuring terrain roughness is important for several disciplines that quantify terrain characteristics evolving within fields, such as geomorphology, engineering, biologists, and ecologists (Doumit, 2017).

In terrain descriptions, roughness parameters should be established that can be used to describe surface irregularities, and they should fulfill some requirements. The parameters should be descriptive and give the reader an image of the physical characteristics of the study area. They should also be easily measurable in the field to quickly sample large sites. Roughness parameters requiring similar field measurements with minimal equipment should be selected if possible. Nowadays, with the appearance of Unmanned aerial vehicles and the advancement of Geographical Information Systems, these parameters can be measured and compared at several scales and are suitable for statistical and numerical analysis.

The profile method is the simplest traditional method of evaluating terrain complexity. Providing multi-sections of the terrain makes it very easy to evaluate its roughness.

Hobson was among the first scientists to calculate terrain Roughness using computer technologies. He wrote Fortran language modules for calculating roughness parameters, such as comparing the estimated actual surface area with the corresponding planar area, bump elevation frequency distribution, and plane distribution (Hobson, 1967).

With the fast evolution of GIS and geoinformatics methods, many scientists worked on the development of other methods for calculating terrain roughness, such as the application of Fourier analysis (Stone, Dugundji, 1965) geostatistics (Herzfeld, et al., 2000), the fractal dimension of a surface (Elliot, 1989; Doumit, Pogorelov, 2017).

One of the first recognized traditional methods for quantifying roughness was the land surface roughness index (LSRI) developed by Beasom et al. (1983). This index is a function of each area's total length of topographic contour lines.

Riley et al. (1999) developed a terrain roughness index (TRI) that is derived from digital elevation models (DEM) implemented in a geographical information system (GIS). TRI uses the sum of changes in elevation within an area as an index of terrain roughness.

Based on the (Hobson, 1972) method developed for measuring surface roughness in geomorphology, a Vector Roughness Measure (VRM) quantifies terrain roughness by measuring the dispersion of vectors orthogonal to the terrain surface.

In this study, we tested the regression between VRM and TRI values at six different levels and provided a correlation analysis between the raster datasets of VRM and TRI to examine their distributions within each scale. We generated scatterplots and calculated descriptive statistics (Min, Max, SD, skewness, kurtosis, and r2) to characterize terrain heterogeneity at different levels.

MATERIALS AND METHODS

A mountainous region of 1700 m, an average elevation above sea level occupying an area of 2 hectares, the Zaarour region on the western Lebanese mountainous chain is characterized by bare land without urbanization and vegetation cover. The benefit of the study of the bare area is that

Digital Surface Models act as Digital Terrain models because the empty area is excluded from manmade activities and vegetation.

Figure 5.1 Google map background with the study area location of Zaarour region (Lebanon) after (Doumit, Pogorelov, 2016).

On a big scale, the study area's micro-relief highlights small terrain structures (ridges and valleys) due to small streams from snow melting processes. These structures are very narrow and give the terrain a heterogeneity of textures and forms influenced by the changing scale.
Drones have been widely used as aerial photography apparatus for many agricultural and terrain analysis applications. One advantage of UAVs is their availability and fast photogrammetry mission execution at different altitudes.
An autopilot DJI Phantom 3 with a camera of 14 megapixels at a focal length of 3.61 mm flies the study area at different Heights. The flight paths of all missions were identical and designed in a mobile application called Litchi, the study area and the flight parameters (coordinates, height, time, etc…). All datasets (photos) of the six missions of different flight heights were processed in Agisoft photo scan software to extract Digital Surface Models (DSM). Before starting the aerial surveying, 10 well-distinguishable control points were evenly distributed within the area of interest for scaling and georeferencing the resulting data. Ground control points (GCP) were collected with a Global Positioning System (GPS) in a stereographic coordinate system.
The drone took Aerial photography with 60% overlapping and 50% side lapping. SfM-based 3D methods operate on overlapping images. The drone flight in an autonomous way, defined by waypoints to avoid image coverage gaps, every surface that will be reconstructed needs, at the minimum, to be covered by at least 2 images taken from different positions.
After executing the flight missions and data capturing, image processing was done in Agisoft Photo scan, following these steps: control points establishment, Image capturing, Feature detection and image alignments, point cloud generation, surface interpolation, and generation of Digital Surface Models.
The project consisted of field and office parts. The fieldwork allowed us to install and survey ground control points. The office part of data processing was repeated six times, englobing the above-listed workflow steps. It began with key point detection and ended with the generation of the six DSMs.

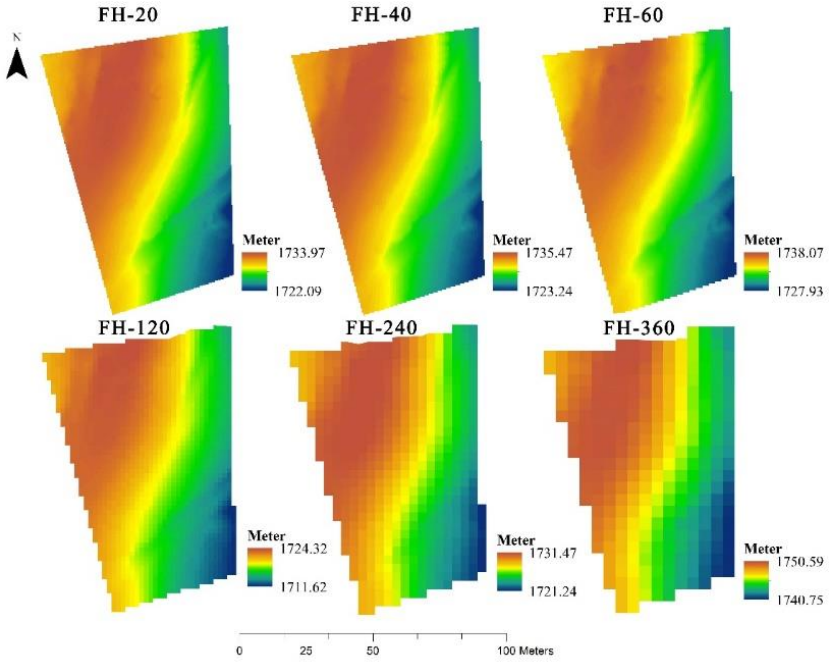

Figure 5.2 Multiscale DSM obtained from image acquisition and processing.

Figure 5.1 shows six DSMs of the study area at different spatial resolutions. FH-20 is at 20 meters' flight height, and a very high-resolution data set highlights all the terrain details, even rock texture. Passing by FH-60, the terrain is smoothed with some concave and convex areas, and it ends by FH-360 at 360 meters.
These 6 DSM can be visually classified from Figure 2 by roughness and smoothness: FH-20, FH-40, and FH-60 for roughness and FH-120, FH-240, and FH-360 for smoothness. Also, Figure 2 constitutes an interval of scales and smoothness, showing the generalization at different scales.

Table 5.1 spatial resolutions of the six generated DSMs.

DSM	Spatial resolution (m)
FH-20	0.4
FH-40	0.6
FH-60	0.80
FH-120	1.70
FH-240	3.20
FH-360	4.50

As per the table, one different flight altitude leads to a different spatial resolution (pixel size). The higher spatial resolution of 0.40 m shows all terrain details and textures, while the lower spatial resolution of 4.50 m is quite good for geomorphological analysis at a local scale.
Our study is independent of DSM accuracy and precision. It will test roughness at six different levels expressed by the drone's flight height at 20, 40, 60, 120, 240, and 360 meters. The flight datum was calculated from the same drone takeoff points for the six flights.
As this study is restricted to evaluating array-based geomorphometric methods for calculating surface Roughness, an input DSM is required for further analysis. DSM selection criteria were based on spatial resolution, with a high-spatial-resolution DSM required to test the heterogeneity across a range of resolutions and within the study area presenting multiscale Roughness features.
The Terrain Roughness Index (TRI) is based on an index described by (Riley et al. 1999) that calculated the sum change in elevation between a grid cell and its eight neighboring grid cells Table 5.2 by squaring the eight differences in elevation, summing the squared differences, and taking the square root of the sum.

Valentine et al. (2004) Calculated the average of the absolute values of the eight differences in elevation by using the TRI equation given:

$$TRI = [abs\{grid(0,0) - grid(-1,-1)\} + abs\{grid(0,0) - grid(0,-1)\} + abs\{grid\ (0,0) - grid(1,-1)\} + abs\{grid(0,0) - grid(1,0)\} + abs\{grid(0,0) - grid(-1,1)\} + abs\{grid\ (0,0) - grid(0,1)\} + abs\{grid(0,0) - grid(-1,0)\} + +abs\{grid(0,0) - grid(1,1)\}]/8 \quad (1)$$

Table 5.23x3 grid of the TRI equation values.

1,-1	0,-1	1,-1
-1,0	0,0	1,0
-1,1	0,1	1,1

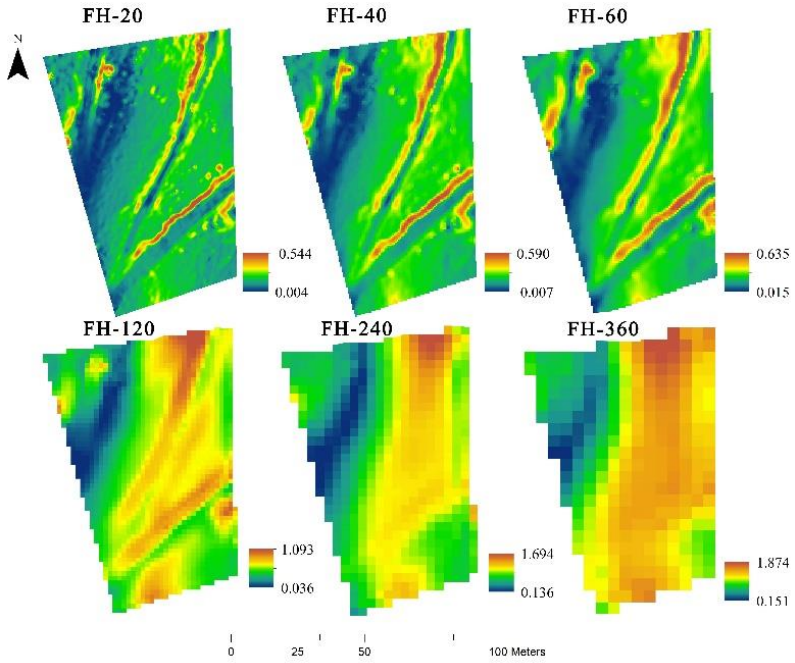

Fig. 5.3 TRI maps at different flight altitudes 20, 40, 60, 120, 240, and 360 above the datum.

TRI high values at FH-20 show details in ridges and water erosion traces. In FH-60, structures are very smooth. FH-120 shows the pixel's boundaries, and at FH-360, the map is pixelated. It is very clear in this map that the small structures disappear with the loss of spatial resolution, running from coarse to smooth and then to pixelated surfaces.

Based on a method developed for measuring surface roughness in geomorphology (Hobson, 1972), the surface of elevation values can be divided into planar triangles very similar to Triangulated Irregular Networks (TIN models) and expected to these planes represented by unit vectors. The vector mean strength (R) and dispersion (k) values can be calculated for each square cell. In smooth areas with similar elevations, the vector strength is expected to be high and the vector dispersion low since the vectors will become parallel Figure 4. In rough areas, the nonsystematic variation in elevation will result in low vector strength and high vector dispersion. The inverse of k can better represent roughness (Mark, 1975).

Based on slope and aspect definitions, normal unit vectors of every grid cell of a digital elevation model (DEM) are decomposed into x, y, and z components.

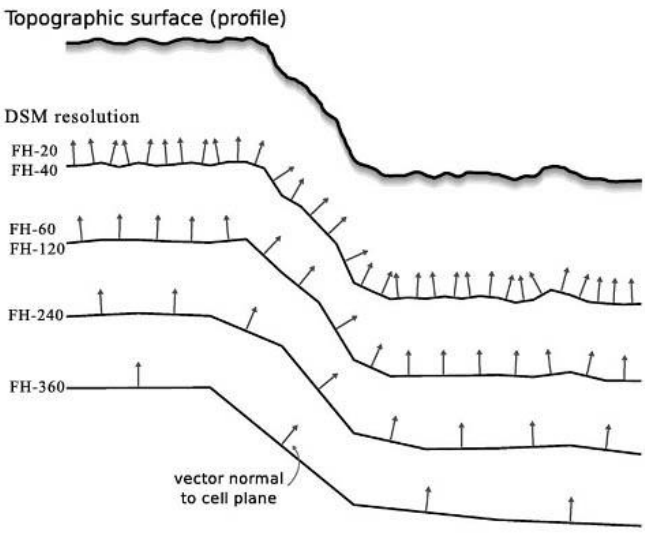

Fig. 5.4 Vector dispersion method used to calculate surface roughness at different scales for a topographical surface. Graphic from (Grohmann, et al. 2011).

DSM resolution is dependent on the flight height. Figure 4 shows the topographic surface profile and the terrain variation. At high spatial resolution, vectors are very dense and orientated in several directions; otherwise, for low spatial DSM resolution, as per example, FH-360 vectors, they are far from each other perpendicular to segments expressing geometrical terrain forms. The translation from the vector dispersion traditional method applied on topographic maps to Vector Roughness Measure (VRM) calculated by GIS algorithms was done by applying the method and formulas used by (Veitinger et al. 2016). Based on slope and aspect definition, the average unit vector of every Digital Surface Model grid cell is decomposed into x, y, and z. A resultant vector R is then obtained for every pixel by summing up the single components of the center pixel and its neighbors using a moving window technique.

$$R = \sqrt{(\sum x)^2 + (\sum y)^2 + (\sum z)^2} \qquad (2)$$

The magnitude of the resultant vector is then normalized by the number of grid cells and subtracted from 1

$$VRM = 1 - \frac{R}{9} \qquad (3)$$

Where VRM is the vector ruggedness measure (Veitinger et al. 2016).

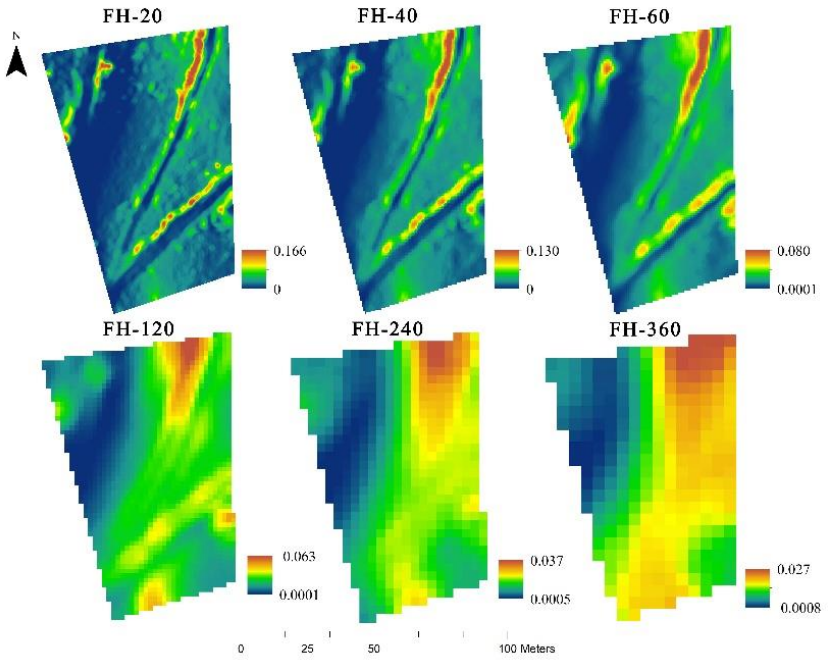

Figure 5.5: VRM maps of the six DSMs

Figure 5.5 shows the six VRM maps generated from DSM using formulae 3; for the first three high spatial resolutions, FH-20, FH-40- 40, and FH-60, terrain structures are very fine highlighted, like the TRI map of Figure 3. The two indices TRI and VRM of the resulted roughness maps showed a loss in terrain heterogeneity and a trend to terrain homogeneity by a high degree of smoothness, especially in the last three DSMs FH-120, FH-240, and FH-360. VRM measures the variation in terrain independent of its overall gradient; VRM can differentiate among terrain types.

RESULTS

In this chapter, we have tested two widely used methods: Terrain Roughness Index (TRI) and vector Roughness Measure (VRM); Terrain et al. (TRI) calculates the sum change in elevation between a grid cell and its neighborhood according to the algorithm by (Valentine et al. 2004).

Table 5.3: Terrain Ruggedness Index statistical values at each level. Std., standard deviation; Skew. Skewness; n, number of cells in a raster grid.

	Mean	Std	Skew.	Kurtosis	n	Min.	Max.	Median	r^2
TRI-20	0.116	0.062	1.202	2.861	40436	0.005	0.544	0.112	0.0014
TRI-40	0.171	0.085	0.702	1.233	18522	0.008	0.591	0.172	0.00006
TRI-60	0.211	0.101	0.602	0.575	8891	0.016	0.636	0.208	0.0059
TRI-120	0.520	0.198	-0.424	-0.045	1901	0.037	1.093	0.552	0.0081
TRI-240	0.822	0.302	-0.385	-0.323	559	0.136	1.695	0.879	0.0033
TRI-360	1.113	0.381	-0.723	-0.448	286	0.152	1.874	1.234	0.0292

Table 5.3 lists the statistics of the TRI values at each flight height, with the values of Min., Max., Mean, and Std. The values of r2 show that the TRI values increased with the flight height and, hence, with the scale. The values of r2 prove that there is no homogeneity of TRI values with their neighborhoods in each layer. This is normal, especially for the high spatial resolution layers TRI-20, TRI-40, and TRI-60 with high n values.
There is no symmetric data distribution for TRI-20 because of the high skewness value of 1.202. However, the evidence is that negative values for the skewness at TRI-120, TRI-240, and TRI-360 indicate data that are skewed left, and positive values for the skewness indicate that the high spatial resolutions layer TRI-20, TRI-40, and TRI-60 are skewed right.

Table 5.4 Vector Ruggedness Measure statistical values at each level.

	Mean	Std	Skew.	Kurtosis	n	Min.	Max.	Median	r^2
VRM-20	0.021	0.019	2.219	6.906	40436	0	0.166	0.017	0.013
VRM-40	0.021	0.017	1.753	4.757	18522	0	0.130	0.018	0.007
VRM-60	0.015	0.012	1.512	3.137	8891	0.0001	0.080	0.013	0.026
VRM-120	0.019	0.011	0.384	0.563	1901	0.0001	0.063	0.020	0.0001
VRM-240	0.015	0.008	0.119	-0.561	559	0.0006	0.037	0.015	0.0009
VRM-360	0.014	0.006	-0.289	-0.914	286	0.0009	0.027	0.015	0.0081

The distributions of roughness values (VRM) for the five levels were highly skewed to the right, with the highest proportion of VRM values at the mean instead of FH-360 values skewed to the left.

Our results showed that TRI and VRM directly measured terrain heterogeneity more independently of scale. Both indices exhibited a pattern of bias in that the minimum value of roughness increased with increasing spatial resolution.

A correlation analysis was provided to understand the similarity between TRI and VRM.

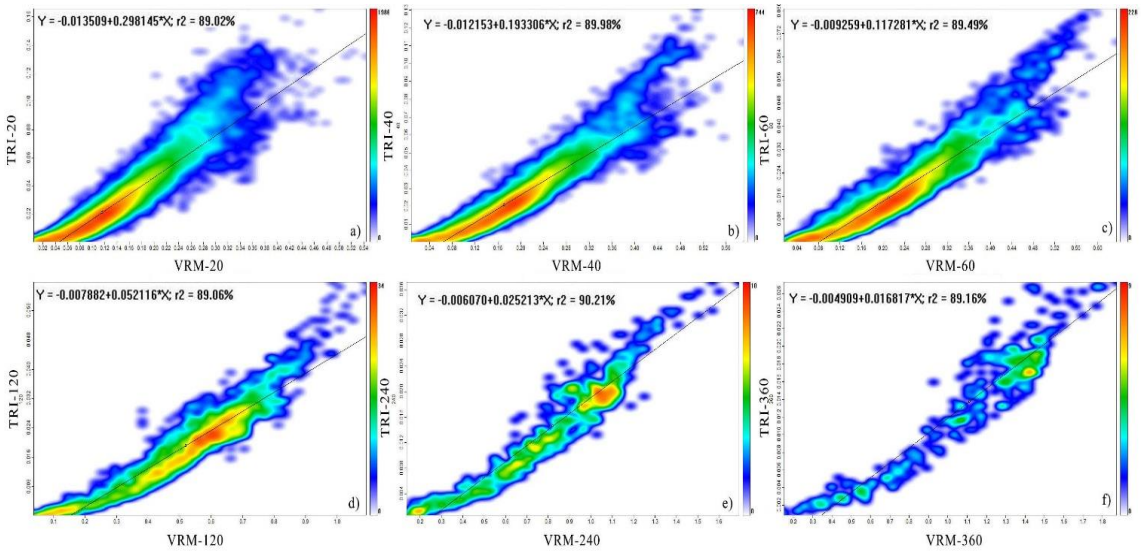

Fig.5.6 Scatterplot of TRI and VRM ruggedness values at all levels of details. a) FH-20, b) FH-40, c) FH-60, d) FH-120, e) FH-240, f) FH-360.

High correlation recorder at all flight heights. The scattered plot of Figure 5.6 shows a high degree of similarity in small values at FH-20, FH-40, and FH-60 expressed in the red elongated areas of Figures 5.6 a, b, and c.

At high flight height, the concentration of the correlated values moves from small to mean values with a trend to the right (Figure 5.6e). Otherwise, the correlation values of TRI and VRM in Figure 5.6f become more scattered and less dense due to a dilution of similarity resulting from changing the spatial resolution (pixel size).

Figure 5.6 shows that the two roughness indices are very similar and have a high correlation. The degree of terrain roughness varies with the spatial resolution. Differences in roughness distributions, measured by VRM and TRI, reflected the terrain's characteristic physiography.

CONCLUSION

Surface Roughness is used as an explanatory index in earth sciences. It is dependent upon exogenic and endogenic geographical processes. Many methods for measuring surface roughness, such as area ratio, vector dispersion, and the standard deviation of the first and second terrain derivative (elevation, slope, and curvature), have been implemented in GIS and based on digital models.

The possibility of producing digital models at different spatial resolutions, spatially UAV-based ones, allows fast and inexpensive multiscale analysis of surface Roughness. At different scale levels, two applied indices, the Topographic Roughness Index (TRI) and Vector Roughness Measure (VRM), express various terrain heterogeneity at a UAV flight height of 20, 40, 60, 120, 240, and 360.

Both indices show a roughness variation with scales and a transition from coarse to smooth between FH-60 and FH-120; a cartographic generalization influenced by flight height is very clear in Figures 5.4 and 5.5. Our statistical and correlation analysis of roughness indices prove that multiscale and multilevel UAV flight datasets are a visual cartographic generalization, a transition scale from one level to another, a live roughness monitoring apparatus leads to the detection of fine scale/regional relief and performance at a variety of scales.

Researchers must know potential biases originating in DSM at multiscale (different spatial resolution) when TRI and VRM values are interpreted. All DSMs contain inherent inaccuracies due to the source errors in the original data. A DSM's elevation accuracy is excellent in flat terrain and decreases in steep terrain where the roughness incises (Koeln et al. 1996). Terrain roughness is a complicated geomorphometric parameter; it can be calculated in many ways under many names, such as roughness, microrelief, and others.

Chapter 6

Multiscale Digital Surface Models for Planar Areas.

Rugosity measures topographic heterogeneity: it describes and counts discrete structures, from categorical to quantitative (McCormick, 1994). Rugosity is an index of surface roughness that is widely used as a measure of landscape structural complexity.
Rugosity is traditionally evaluated in situ across a two-dimensional terrain profile by draping a chain over the surface and comparing the length of the chain with the linear length of the profile Figure 6.1.
Two-dimensional rugosity is the ratio between the surface contour distance and the linear distance between two points (Risk, 1972). It is synonymous with tortuosity or the arc-chord ratio (Moser et al., 2007).
Multiple measures of structural complexity exist (McCormick, 1994). For over forty years, many scientists have used the rugosity index for topographic (elevation) or bathymetric (depth) datasets; rugosity can be calculated from two—or three-dimensional data at any scale.
Drone-based digital surface models at different flight heights and on different scales could be good material for rugosity analysis.

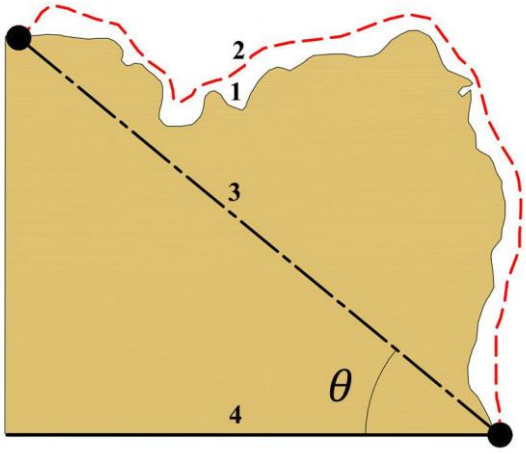

Fig. 6.1 The rugosity of a surface (e.g., the yellow profile of a terrain № 1) is the ratio between the contoured distance (dashed line № 2) and the planar distance (or area for three-dimensional data).

The standard surface ratio (SR) method for calculating a planar distance is to project the surface onto a horizontal plane (solid line); this method confounds rugosity with the slope (θ) at the scale of the surface (solid line).
Figure 1 shows the very expressive section length of section number 1; the natural terrain is 5.8 km, a very complex terrain. Section 2 shows smoothed terrain like the natural terrain but 5.3 km in length. Section three expresses a slope projection of the natural terrain with a 3.5 km length. The last section, horizontal planar section 4 with 2.8 km, is influenced by the slope angle (θ). The significant change in length from section 1 to horizontal section 4 is approximately half. The idea here is not the length or surface change but the rugosity changes at different DSM spatial resolutions.
Six DSM generated from different UAV flight heights constitute the base of our study, which compares the transition to planar areas at different levels.
In the early 1970s, Risk (1972; Dahl, 1973) introduced the standard surface ratio (SR) method for measuring rugosity. They calculated rugosity by projecting the surface onto a horizontal plane (Lundblad et al., 2006; Wright & Heyman, 2008; Friedman et al., 2012), thereby coupling rugosity with the slope at the scale of the surface equation 1.

$$Rugosity = \frac{Contoured\ area}{Planar\ area} \qquad (1)$$

In the case of equation 1, rugosity increases with increasing slope (figure 1); the law of cosines, where cos (θ) = adjacent side ÷ hypotenuse side), presents the fundamental issue presented by the traditional methods for measuring rugosity.
A flat surface has a rugosity value of one, while a rougher surface or a surface with more relief has a higher rugosity value than one. Rugosity combines structural relief and roughness (Moser et al., 2007).
Du Preez (2014) developed a new arc–chord ratio (ACR) rugosity index to quantify landscape structural complexity and overcome significant issues presented by traditional rugosity indices. Compared to other methods for measuring rugosity, ACR rugosity is separated from the slope, and it is easy to execute an ACR rugosity analysis using GIS software (Du Preez, 2014).
Many marine and land studies use rugosity such as environmental risk assessment, species management, distribution and conservation, and predictive mapping of vulnerable marine and land ecosystems (Stambaugh & Guyette, 2008; Wedding et al. 2008; Galparsoro et al., 2009; Woodby et al., 2009).
In this Chapter, the ACR three-dimensional method is tested on the six generated DSM and compared at different levels of spatial resolution by correlation and statistical analysis.
Spatial resolution is an important factor in scale influence on rugosity. Our paper will prove that by answering the question: Did the transition of the multiscale Digital Surface Models to planar areas have the same results?

MATERIALS AND METHODS

The Zaarour region of the western Lebanese mountainous chain is a mountainous region with an average elevation above sea level of 1700 m and an area of 2 hectares. It is characterized by bare land without urbanization and vegetation cover. The benefit of this study's bare area is that Digital Surface Models act as Digital Terrain models.
An autopilot DJI Phantom 3 drone with a camera of 14 megapixels at a focal length of 3.61 mm flies the study area at different Heights.
The flight paths of all missions are identical and designed in a mobile application called Litchi, along with the study area and the flight parameters (coordinates, height, time, etc....). All datasets (photos) of the six missions with different flight heights were processed in Agisoft photo scan software to generate Digital Surface Models (DSM).
Drones have been widely used for aerial photography and many agricultural and terrain analysis applications.
One advantage of UAVs is their availability and fast photogrammetry mission execution at different altitudes. This paper will only discuss the spatial scale with the UAV flight altitudes. Our study will test the rugosity index at six different levels, expressed by the flight height of a drone at 20, 40, 60, 120, 240, and 360 meters. The flight datum was calculated from the same drone takeoff points for the six flights.

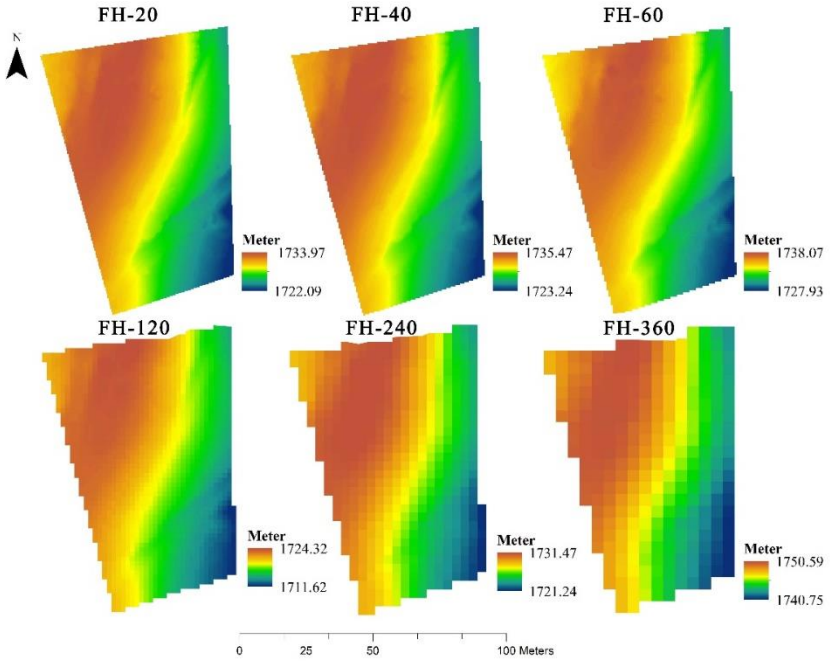

Fig.6.2 multiscale DSM obtained from image acquisition and processing.

Figure 2 shows six DSMs of the study area at different spatial resolutions: FA-20, at 20 meters' flight altitude, with a very high-resolution data set highlighting all the terrain details, even rock texture. Passing FA-60, the terrain is smoothed with some concave and convex areas, ending with FA-360 at 360 meters.
These 6 DSM can be visually classified from Figure 6.2 as rough and smooth: FA-20, FA-40, and FA-60 for rough and FA-120, FA-240, and FA-360 for smooth. Also, Figure 1 constitutes an interval of scales and smoothness, showing the generalization at different scales.

Table 6.1: Spatial resolutions of the six generated DSMs.

DSM	Spatial resolution (m)
FH-20	0.4
FH-40	0.6
FH-60	0.80
FH-120	1.70
FH-240	3.20
FH-360	4.50

The table shows that each flight altitude leads to a different spatial resolution (pixel size). The minimum spatial resolution is 0.40 m, which is high enough to show all terrain details, and the maximum resolution is 4.50 m, which is quite good for geomorphological analysis at a local scale.
Many methods of evaluating rugosity on a three-dimensional surface have been proposed. These methods measure a ratio of areas rather than lengths, as shown in Equation (1).
The surface area to Planar Area (SAPA) method introduced by Jeff Jenness evaluates rugosity using a 3 x 3 neighborhood by drawing a line from the center of each cell in the window to the center of the central cell in three dimensions. The result is a network of eight triangles in the central cell approximating the contoured surface at the cell location. The sum area of these triangles is divided by the two-dimensional cell area to measure rugosity (Jenness, 2004).
Du Preez and Tunnicliffe (2012) propose a novel method for measuring rugosity that decouples rugosity from the slope and is consistently independent of data dimensionality and scale. It is a simple adaptation of an Arc Chord Ratio (ACR). The method replaces the horizontal plane with a plane of best fit (POBF), where the POBF is a function of boundary data interpolation (Preez & Tunnicliffe, 2012). The ACR method can be used in multi-scale analyses, an essential attribute

of spatial analysis, as morphological processes act at various spatial scales (Levin, 1992) and differ in effects and importance with scale (Wu, 2013).
Based on Du Preez (2014), Jeff Jenness developed a new technique that operates on a 3x3 neighborhood. It uses the triangulated area of each adjacent cell and applies the Pythagorean theorem to compute the surface area. By default, the planar area of each grid cell is corrected by dividing the cell area by the cosine slope (Jenness, 2004).
Our study calculated ACR using a GIS tool installed on ArcGIS® Software, available for download in Du Preez 2014. From the six generated DSMs, we calculated the Arc-Chord ratio (ACR). The ACR rugosity index is a measure of three-dimensional structural complexity defined as the contoured area of the surface divided by the area of the surface orthogonally projected onto a plane of best fit.
The arc-chord ratio (ACR) method calculates the planar distance by projecting the surface boundary onto a boundary data section 1 figure 1 (Red dashed line) plane of best-fit section 3 figure 6.1 (POBF; dashed-dotted line; 3) effectively decoupling rugosity from the slope at the scale of the surface. ACR is calculated by creating two TINs, a contoured surface and a planar one representing the plane of best fit (POBF) Figure 3a. The POBF is a function (interpolation) of the boundary data only of the area of interest. The area of interest is the boundary of the study area. The surface area of the first TIN is divided by that of the second TIN to obtain a single ACR value for the area of interest (Du Preez, 2014).

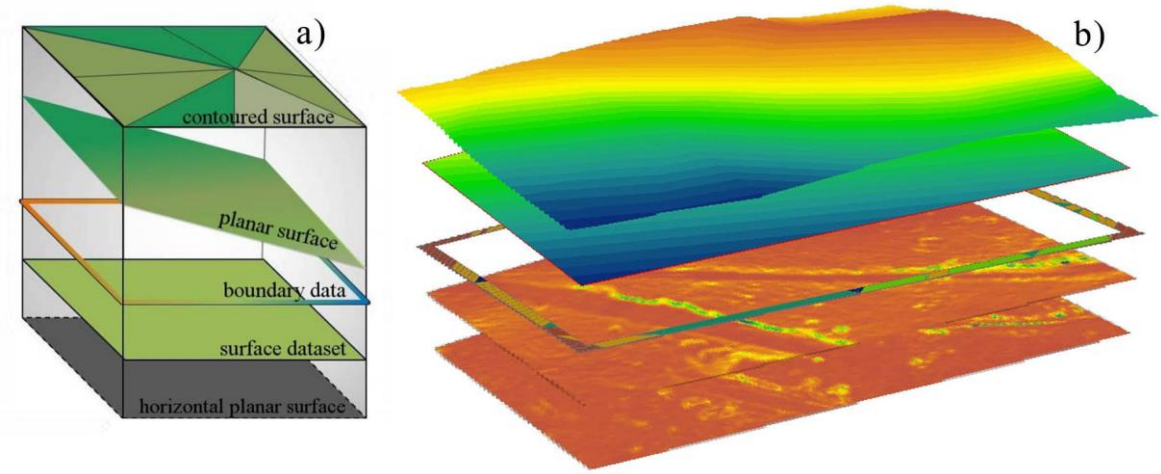

Fig.6.3 a) ACR simultaneous surfaces leading to the horizontal planar one, b) an example of ACR surfaces of FH-20.

As a first step, the conversation from raster to TIN for the six DSMs to form contour surfaces at different scales.

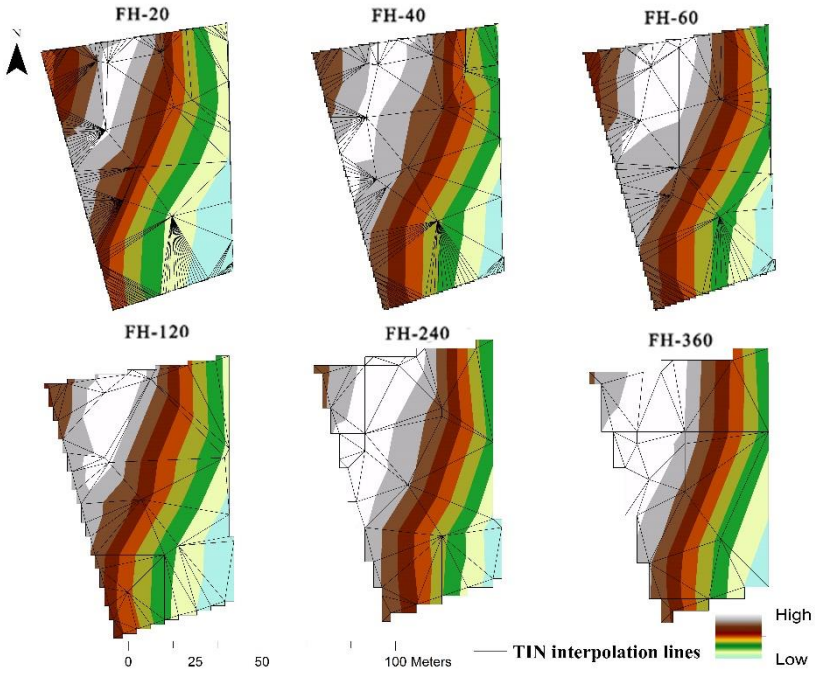

Fig.6.4 TIN models of contour surface at the six flight heights.

All six TIN models expressed the terrain morphology, with some variations detected on the colored contour lines and a generalization in the triangle quantity.

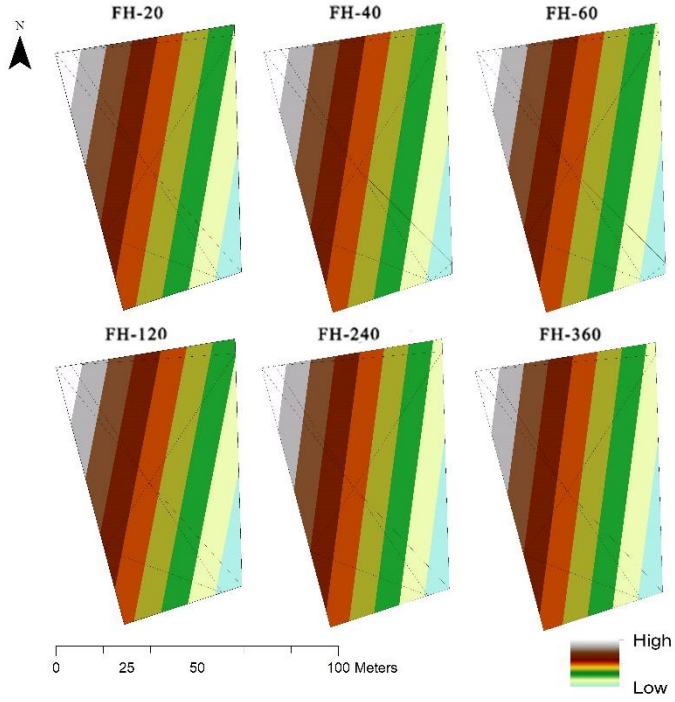

Fig.6.5 The POBF of the six flight heights

In step two, the contoured surface is translated to a plane of best fit (POBF), decoupling rugosity from the slope at the surface's scale (Du Preez & Tunnicliffe, 2012; Friedman et al., 2012). Figure 6.5 shows six similar planar surfaces owning the same trend of values by simplifying the elevation values of the contour surfaces.
The innovation of the ACR method lies in the analysis used to generate the POBF: identify and isolate the boundary data (step three). Figure 6.3a illustrates the boundary data of FH-20, the triangulated irregular network data frame.

To generate surface datasets (step four), a linear polynomial interpolation of the boundary data at the six levels is used.
Some software is unable to interpolate the actual planar area. An alternative is to interpolate the angle of the POBF and use the cosine equation (and the horizontal planar area) to extract the planar area of step five (Du Preez, 2014).
To solve for the ACR rugosity index, apply Formula 1 using the contoured and planar areas (step six).
By following Du Preez and Tunnicliffe's (2012) arc–chord ratio (ACR), we Computed a ratio between the surface's three-dimensional surface area and the planar area. This tool uses a novel methodology to develop a surface area dataset. The output values represent ratios between the surface area and planar area, typically ranging from 1 in flat areas to 4 in areas of high variation.

DISCUSSION AND RESULTS

Figure 6.4 shows the first step of Du Preez's methodology of conversation from raster to TIN for the similar six TIN models. The same study area at different spatial resolutions leads to visual data similarity. A statistical comparison was made to test this degree of similarity, as shown in Table 6.3.

Table 6.3 Elevation TIN statistics, quantity of triangles, average minimum and maximum elevations, and the slope average.

Contoured area TIN				
Flight height	Quantity of triangles	Average Min. Elev	Average Max. Elev	Average Slope %
20	321	1728.95	1729.94	15.89
40	230	1730.26	1731.53	16.70
60	172	1733.58	1734.85	14.52
120	85	1718.65	1720.76	17.03
240	58	1727.14	1729.25	14.48
360	41	1746.67	1748.87	13.00

The statistical values of Table 6.3 show a decrease in triangle numbers from 321 to 41 due to a decrease in spatial resolution and the difference in average maximum and minimum elevations due to the interpolated predicted values.
The quantity of triangles from the elevation area to the planar area of Tables 3 and 4 is reduced more than twenty times in high spatial resolution data of 20, 40, and 60-meter flight heights; otherwise, low spatial resolution data with low triangle quantities in contoured areas are reduced less than ten times in planar areas TIN models.
The average maximum and minimum elevations at all levels are reduced by 2 meters between surface and planar areas, reducing the average slope by 2 percent.

Table 6.4 POBF, planar TIN area statistics quantity of triangles, average minimum and maximum elevations, and the slope average.

Planar area TIN				
Flight height	Quantity of triangles	Average Min. Elev	Average Max. Elev	Average Slope %
20	10	1725.72	1731.67	13.23
40	9	1726.72	1732.41	14.13
60	9	1732.90	1732.98	10.44
120	8	1715.46	1722.23	14.87
240	8	1724.62	1729.84	11.72
360	7	1746.22	1746.66	10.75

In planar area TIN, the average values of the minimum and maximum elevations in all six flights are reduced with the number of triangles due to the transition from contoured to planar area.

The variation in values between Table 3 and Table 4 showed an unstable change in elevations and slope.
The first part of the transition from contoured area TIN to planar area TIN (POBF) is very similar to trend analysis, which simplifies the complexity of values by conserving the same datum.
Otherwise, the second transition from surface area two to planar one records a loss of initial datum elevation to zero (Table 6.5).

Table 5: Surface area statistics at different flight heights.

Surface Area				
Flight heights	Min	Max	Mean	Std
20	0.141	0.227	0.144	0.005
40	0.312	0.415	0.319	0.008
60	0.645	0.756	0.657	0.013
120	3.007	3.342	3.073	0.048
240	10.7	11.3	10.867	0.105
360	19.976	20.705	20.291	0.172

High spatial resolution data of 20, 40, and 60 have submeter surface area values, rising approximately in double values between flight heights.
The surface area is designed to determine the amount of similarity between the tested area surface and the planar surface. It is hypothesized that the surface area increases with surface irregularity. Because there is a definite interplay between the number and magnitude of terrain irregularities, similar surface area estimates could arise from different manipulations of these two variables.

Table 6.6: Planar area statistics and different flight heights.

Planar Area				
Flight height	Min	Max	Mean	Std
20	0.99	1.154	1	0.005
40	0.99	1.132	1	0.003
60	0.99	1.045	1	0.002
120	0.99	1.013	1	0.001
240	0.99	1.003	1	0.0006
360	0.99	1.003	1	0.0005

The values of the planar area at different scales are practically the same, with small variations at low flight heights. Based on the results of Table 6, especially the similar mean values, we can answer the above question constituting the target of our paper by saying: yes, the transition of the multiscale Digital Surface Models to planar areas has *the same results.*
Visual and statistical results prove the similarity of multiscale planar data. A regression analysis was run to test this similarity in the planar surface at multiscale.

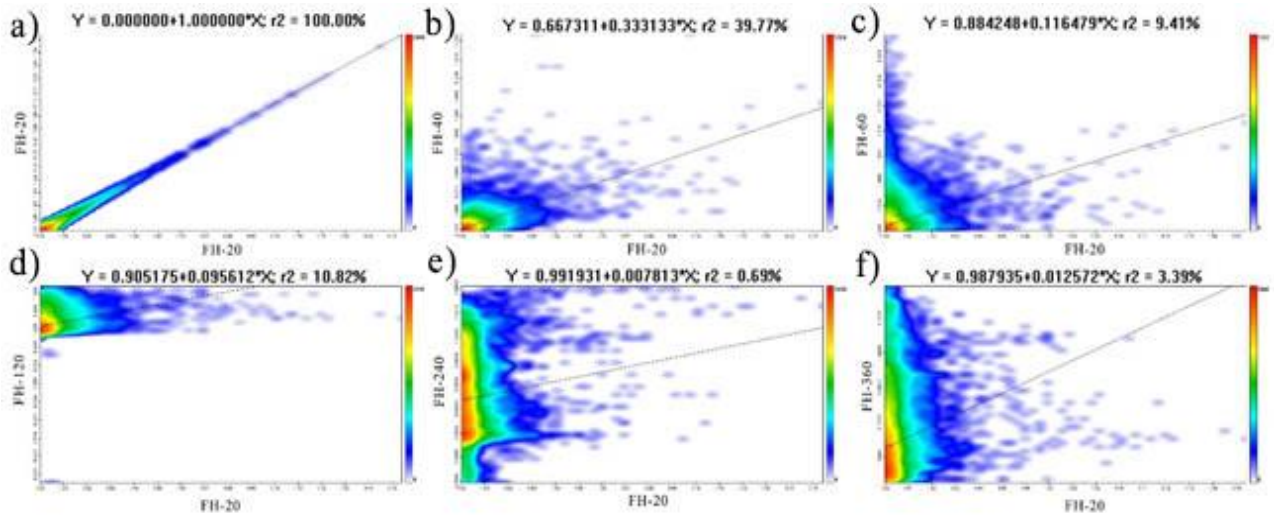

Fig. 6.6 Scattered plots of planar areas at different scales.

The correlation analysis between the highest spatial resolution data of FH-20 as a reference and the other datasets, Figure 6.6a, shows a test scatterplot with the same data set in the X and Y axes of FH-20, with a hundred percent similarity.
The graph FH-40 with FH-20 gives 39.77 % similarity (Figure 6.6b). The r square values of FH-60, FH-120, FH-240, and FH-360 against FH-20 are less than 11 %. The core of the scatterplots for the high spatial resolution datasets are in the lower left corners, moving positively with the Y axes in FH-120 and then falling negatively for FH-360.
Unlike visual and statistical correlation analysis, it showed a difference in multiscale planar areas.

CONCLUSION

Nowadays, using UAVs for terrain analysis presents an initial tool for multiscale Digital Surface interpretations. Our research aims to understand how the rugosity evolution acts on the six flight heights deriving different spatial resolution datasets.
The paper provides a multiscale DSM analysis by adapting and improving ACR geo-processing model tools and step-by-step application of the Du Preez 2014 module. Improving standard methods for the detection and investigation of geomorphological patterns at different spatial resolutions will lead to better scientific information for generalizations, terrain analysis, management and conservation initiatives.
This paper concludes that Scale and resolution effects on terrain data are important issues in geographic research. DSM UAVs based on high flights should be tested before use.
It is essential to understand the effects of scale on the analysis results. Each elevation data point has its own surface-to-planar result, terrain rugosity depends on spatial resolution, and visual analysis should follow a correlation one.

Chapter 7

Multiscale landforms classification.

The fast evolution in technologies, especially in geoinformatics, data, and software, and the appearance of Unmanned Aerial Vehicle (UAV) and their applications for digital surface extraction leads to multiscale terrain analysis. Scale is predominantly considered a function of the resolution of Digital Surface Models (DSMs) (Hengl & Evans, 2009; Mac et al., 2009). The dependency on the land surface has been confirmed by several researchers. (Chang and Tsai 1991, Wood 1996, Florinsky and Kuryakova 2000, Evans 2003, Hengl 2006, Arrell et al. 2007, Deng et al. 2007, Pogorelov and Doumit 2009, Wood 2009).
The factor of scale plays a very important role in Landform classification. Different levels of measurement (nominal, ordinal, interval, and ratio) are used. This paper will discuss terrain analysis using the Terrain Position Index (TPI), Iwahashi and Pike index, morphometric features, and their effects on generalization and spatial resolution at different UAV flight altitudes.
Pike et al. (2009) remarked that no digital elevation models derived from maps are definitive, as the generated parameters differ with algorithms and can vary with resolution and scale.
Landform classification stands out because of terrain complexity, necessitating specific methods to quantify its shape and subdivide it into more manageable components (Evans, 1990; Gercek 2010). This constitutes a central research topic in geomorphometry (Pike, 2002; Rasemann et Al. 2004).
An Arc Map Jenness module GIS software for landforms and terrain computations was applied to three different spatial resolution drone-based DSMs to extract the Topographic Position Index (TPI), Iwahashi, and Pike landforms, and morphometric features at different scales.

MATERIALS AND METHODS

On the western Lebanese mountainous chain, our project location lies in an area of about 2 hectares in the Zaarour region (figure 1). Bare lands represent the chosen nonurbanized mountainous area with a slight natural slope with elements of anthropogenic relief. The inclusion of anthropogenic micro-relief in the studying area is due not only to the requirements of representativeness but also the presence of a complicated microform for the experimental modeling of the terrain concave and convex smoothed areas.

Fig 7.1 Google Earth Spatio-image of Lebanon showing the study area.

A DJI Phantom 3 UAV, equipped with a camera of 14 megapixels at a focal length of 3.61 mm, was used to scan the study area at different Heights. Flight Heights are measured from the UAV's takeoff point; the experiment consisted of three missions at 120, 240, and 360-meters height (FA-120, FA-240, and FA-360).

The three UAV missions have the same flight path designed in a mobile autopilot application called Litchi (Figure 2). The autopilot's on-screen display shows the flight path, the study area, and the flight parameters (coordinates, height, time, etc....). All datasets of the three missions with different flight heights were processed in Agisoft photo scan software to extract Digital Surface Models (DSM).

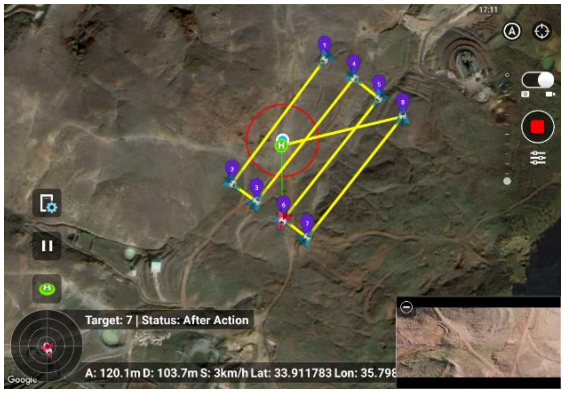

Fig 7.2 shows the designed path of the three flight missions.

Throughout the assessment, we used this UAV to acquire aerial images to generate and interpret Digital Surface Models (DSM) using new photogrammetry technologies.
Figure 7.3 shows three DSM of different spatial resolutions. FA-20 of 20 meters flight altitude with a high resolution highlighted all the terrain details, even the rock texture; passing by FA-120, the terrain is smoothed with some concave and convex areas, and ending by FA-360, a very low spatial resolution and a very smoothed terrain of 360 meters' flight altitude.

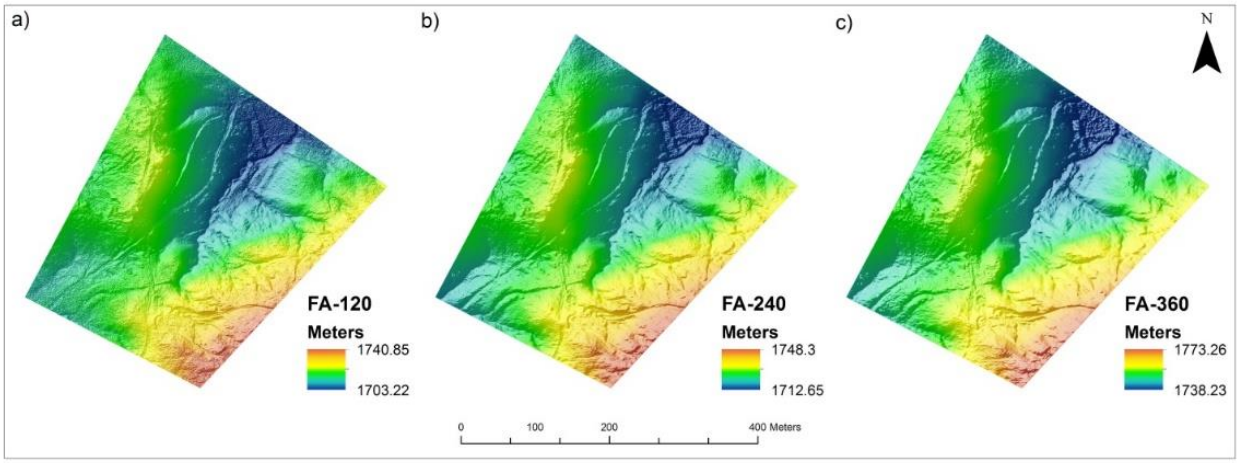

Fig.7.3 multiscale DSM extracted based on UAV photogrammetry, a) DSM of flight height 120 meters, b) DSM of flight height 240 meters, and c) DSM 360 meters.

These 3 DSMs can be classified visually from Figure 1, from rough to smooth: FA-120, FA-240, and FA-360. Also, Figure 7.1 constitutes an interval of scales and smoothness, showing the generalization at different scales.
Table 7.1: DSM spatial resolution at different flight scales.

DSM	Spatial resolution (m)
FA-120	1.73
FA-240	3.20
FA-360	4.47

According to the table, each different flight altitude led to different spatial resolutions (pixel size). According to the photogrammetry law, the higher the flight altitude, the greater the scale. The minimum spatial resolution is 1.73 m, which expresses a level of detail, and the maximum resolution is 4.47 m, which is quite good for geomorphological analysis at a local scale.
Topographic Position Index (TPI) DSM's simulation performed the analysis to obtain the topographic position index (TPI). The process of formulae (1) calculates the difference between elevation at a specific cell and the average elevation of the neighborhood surrounding cells (Tagil & Jenness, 2008), describing higher and lower areas for the classification of the terrain into different morphological forms (Jenness 2005).
The simulation required adjusting the radius of the neighborhood and its geometric shape based on two different scales or sizes (Barka et al. 2011). This study applied a radius between 5 m and 25 m to determine the slope positions.

$$\mathrm{TPI} = Z_0 - \frac{\sum_{1-n} Z_n}{n} \qquad (1)$$

Were.
Z_0 = elevation of the model point under evaluation
Z_n = elevation of the grid within the local window
n = the total number of surrounding points employed in the evaluation
These neighborhood radius values were applied for all DSMs spatial resolutions to be similar in parameters for best comparison analysis.
Positive TPI values represent high locations, e.g., ridges. Negative values represent low terrain, e.g., valleys. Otherwise, flat areas have TPI values near zero. High positive values go to high-elevation geomorphological structures, such as peaks and ridges (Jenness, J. 2010).
The flight altitude FA-20 has a maximum positive value of 1.03, FA-60 of 0.71, and the higher flight altitude FA-360 with 0.48, a decrease in maximum and minimum values with increasing flight altitude.
Iwahashi and Pike developed an unsupervised landform classification method based on only three terrain attributes: slope gradient, surface texture, and local convexity (Iwahashi & Pike, 2007). This method restricts several landform classes 8, 12, or 16 with a physical meaning of statistical landscape properties.
The unsupervised approach treats topography as a continuous random surface, especially for the three levels of details FA-120, FA-240, and FA-360, independent of any spatial or morphological orderliness imposed by fluvial activity and other geomorphic processes.
Morphometric elements, the standard method for identifying morphological elements, establish a mutual position for the central cell relative to its neighbors (Peucker, Douglas, 1974; Evans, 1979). The classification algorithm can be done by maintaining the continuity of linear elements, which gives advantages over the method of selection based on logical comparison of neighboring cells (Peucker, Douglas, 1974; Jenson, 1985; Bennett, Armstrong, 1989; Skidmore, 1990; Pogorelov, Doumit, 2009).
Morphological elements include Planar, pit, channel (thalweg), pass, ridge (division line), and peak. Although the names of morphological elements may vary between sources, they can be uniquely explained in terms of changes in the three orthogonal components x, y, and z (Wood J, 1996; Pogorelov, Doumit 2009).

RESULTS AND DISCUSSIONS

Landform classifications delineated using the TPI method are shown in Figure 4; TPI values present a powerful way to classify the landscape into morphological classes (Jenness, 2005). Landform Classifications consist of "Canyons, Deeply Incised Streams'', ''Midslope Drainages, Shallow Valleys'' and ''Upland Drainages, Headwaters'' all tended to have strongly negative curvature values of a concave shape, while "Local Ridges or Hills," ''Midslope Ridges, Small Hills in Plains'' and ''Mountain Tops, High Ridges'' all tended to have strongly positive curvature values of a convex shape.
Figure 2 of the three maps shows landforms classification of all morphological forms listed above at different scale levels; visual analysis of these maps highlights a cartographic generalization between them, making a very clear evolution in morphological forms at each stage.

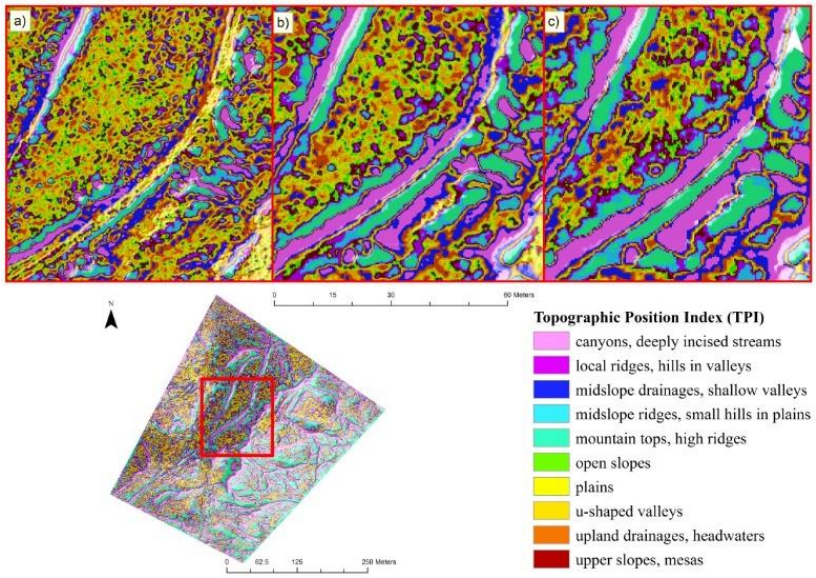

Fig.7.4 maps of the three DSM landform elements derived from TPI classification analysis. a) FA-120, b) FA-240, c) FA-360.

The results of Table 7.2 show how the area of some morphological elements is increasing against other elements relating to scale variations. In Table 3, the area percentages of some morphological elements are increasing in value, and others are decreasing with the scale variation. Streams, plains, open slopes, and high ridges are increasing in area and geometrical forms due to the variations in spatial resolution. Some morphological elements, such as Upland drainage type, are not found in any of the three maps, and others, like Local ridges, are disappearing with scale variation and constituting a basis for generalization processes.

Table 7.2: Percentage of Morphological elements and pixel numbers of each Morphological element in the three DSM levels based on TPI classification.

	Area (%)			Number of pixels		
Type	FA-120	FA-240	FA-360	FA-120	FA-240	FA-360
Canyons, deeply incised streams	5.87	9.32	14.7	6155	1036	800
Midslope drainages, shallow valleys	9.75	10.6	11.46	31823	6684	5984
Upland drainages, headwaters	12.82	11.58	9.7	79684	19287	14025
U-shaped valleys	17.24	13.02	9.01	112465	29124	18901

Plains	13.1	9.69	6.39	158603	42986	22098
Open slopes	10.94	9.1	6.35	153612	42504	21892
Upper slopes, mesas	10.9	10.77	8.87	110730	30022	18910
Local ridges, hills in valleys	7.99	9.49	9.53	76494	19574	14150
Midslope ridges, small hills in plains	6.4	8.88	10.72	35575	6902	6227
Mountain tops, high ridges	4.99	7.55	13.28	6818	1663	1086
Total number of pixels				**771959**	**199782**	**124073**

Open slopes comprised between 6 and 11% of the total area at all flight altitudes, while midslope drainages increased with the flight heights, ranging between 9.75% and 11.46% of the total study area.

Landforms show a decreasing number, with a dilution of 647886 pixels of different morphological elements from the flight height FA-120 to the flight height FA-360. All ten morphological elements are affected by scale generalization.

To understand the degree of generalization between the big scale of FA-120 and the small scale of FA-360, we provided an ascending classification of the geomorphological forms: ridges (Local, Midslope, and high) and drainage areas (upland and midslope). Hence, generalization positively affects all other morphological forms by raising their areas.

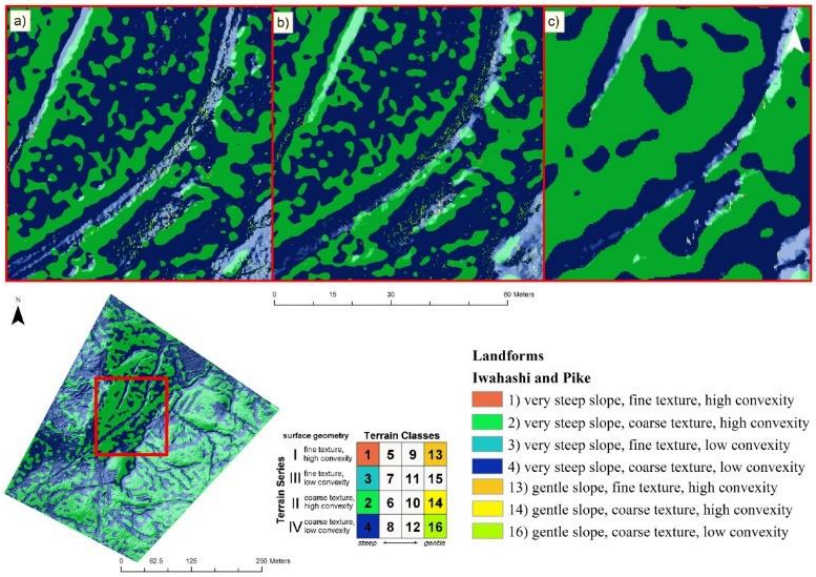

Fig.7.5 Landform maps of unsupervised classification (Iwahashi and Pike method), a) FA-120, b) FA-240, c) FA-360.

Table 3: Iwahashi and Pike landform percentage of areas at different scales.

	Area (%)		
Type	FA-120	FA-240	FA-360
1) very steep slope, fine texture, high convexity	0.00987	–	–
2) very steep slope, coarse texture, high convexity	47.33649	48.5	49.9
3) very steep slope, fine texture, low convexity	0.00144	–	–
4) very steep slope, coarse texture, low convexity	51.13720	51.2	49.9

5) steep slope, fine texture, high convexity	–	–	–
6) steep slope, coarse texture, high convexity	–	–	–
7) steep slope, fine texture, low convexity	–	–	–
8) steep slope, coarse texture, low convexity	–	–	–
9) moderate slope, fine texture, high convexity	–	–	–
10) moderate slope, coarse texture, high convexity	–	–	–
11) moderate slope, fine texture, low convexity	–	–	–
12) moderate slope, coarse texture, low convexity	–	–	–
13) gentle slope, fine texture, high convexity	–	–	–
14) gentle slope, coarse texture, high convexity	0.67723	0.2	0.1
15) gentle slope, fine texture, low convexity	–	–	–
16) gentle slope, coarse texture, low convexity	0.83771	0.2	0.1

The concavity and convexity of the very steep slope have fine textures found only in high spatial resolution models (FA-120), with the coarse texture of high convexity increasing with the pixel size.
Step and moderate slopes are not detected in all three models. Gentle slopes, coarse texture, and high and low convexity increase with the flight altitude.
Varying DSM spatial resolution can achieve an element's separation of appropriate scale, without the need for generalization.

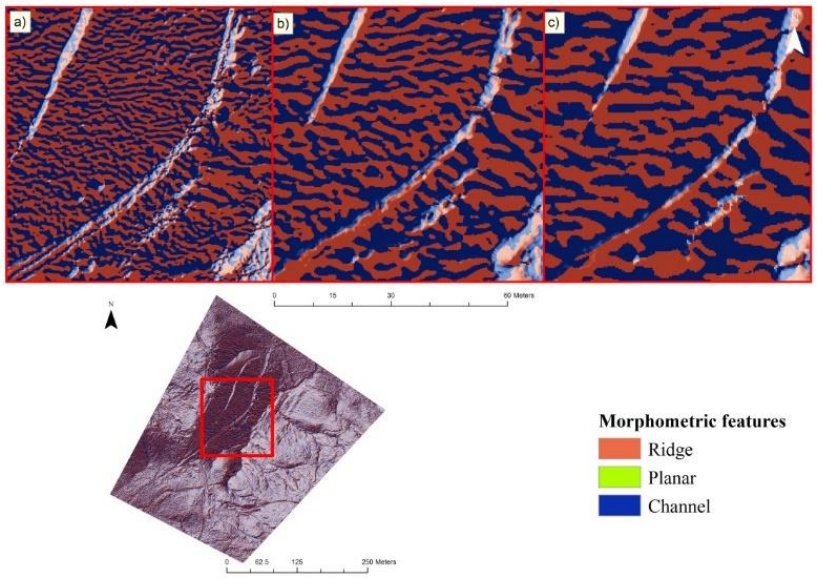

Fig.7.6 Morphometric features maps, a) FA-120, b) FA-240, c) FA-360.

Table 7.4 Surface-specific points area percentages of the study area are at different scales.

	Area (%)		
Type	FA-120	FA-240	FA-360
Planar	0.00001	–	–
Pit	–	–	–
Channel	49.72501	48.3	47.4
Pass (saddle)	–	–	–
Ridge	50.27497	51.7	52.6
Peak	–	–	–

As per Table 7.4, some morphometric features like pit, pass, and peak are not detected in all flight altitudes. Otherwise, planar areas are detected in FA-120 at the lower flight altitude at a very low percentage of area, in the order of 0.00001 %. We cannot judge this result because the value of this pixel could be a processing artifact. The area of channels increases with the flight altitude, and the ridge area decreases against channel one.
The dominating landforms of surface-specific points channels and ridges of the study area form comparison models of each flight height with TPI landforms. By splitting channels and Ridges of FA-120, FA-240, and FA-360 and excluding which TPI landforms are included in each type, Table 7.5 shows the area percentage of each landform.

Table 7.5: Percentage of TPI landforms contained in Ridges and Channels at each flight altitude.

TPI Landforms	**Percentage of area**					
	Ridge-120	**Channel-120**	**Ridge-240**	**Channel-240**	**Ridge-360**	**Channel-360**
Canyons, deeply incised streams	1.5	10.4	2.4	16.8	4.3	26.3
Midslope drainages, shallow valleys	3.3	16.3	3.9	17.8	4.9	18.6
Upland drainages, headwaters	5.7	19.7	5.4	18.0	5.6	14.4
U-shaped valleys	11.9	23.1	9.3	17.1	7.0	11.2
Plains	13.7	12.4	9.6	9.6	6.3	6.5
Open slopes	14.7	7.1	11.4	6.8	7.1	5.4
Upper slopes, mesas	16.5	5.3	15.3	5.7	11.5	6.0
Local ridges, hills in valleys	12.9	3.0	14.9	3.7	13.8	4.9
Midslope ridges, small hills in plains	10.7	1.9	14.6	2.7	16.8	3.9
Mountain tops, high ridges	9.1	0.9	13.1	1.6	22.7	2.9

Upper slope areas in ridge-120 and ridge-240 occupy a high percentage of the area; for ridge-360, the higher percentage goes to Mountain tops. Upland drainage has high values in channels FA-120 and FA-240, but FA-360's higher area goes to Canyons. From these results, we can see a TPI landform transition with scales.

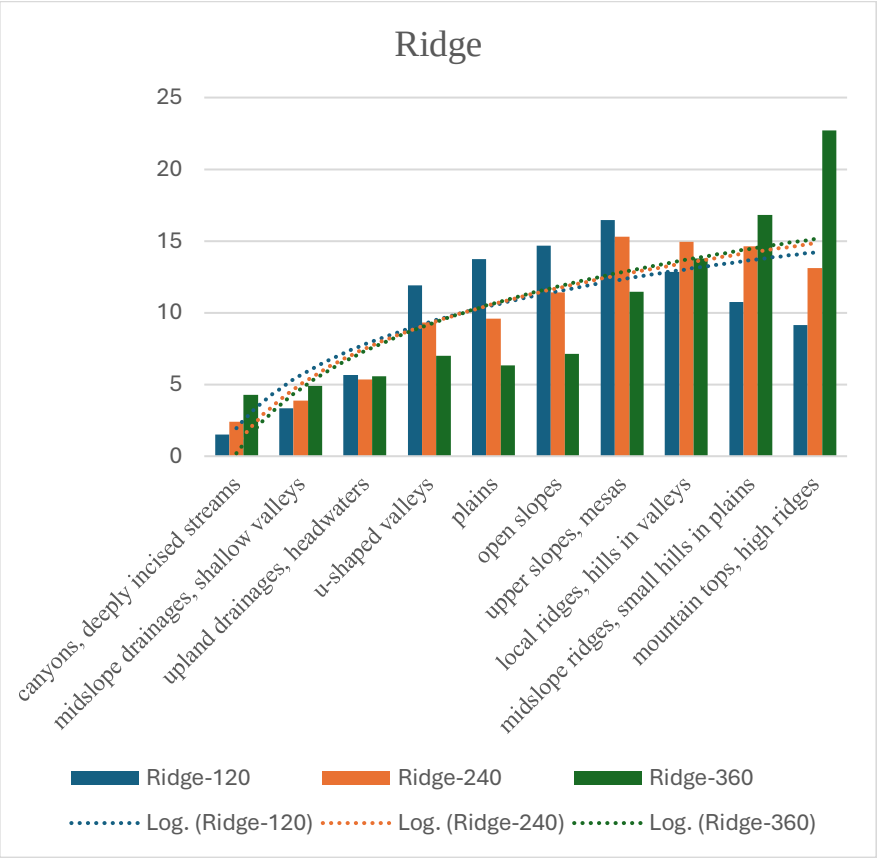

Fig.7.7 Diagram of area percentage of TPI landforms contained in Ridge at flight altitudes of 120,240 and 360 meters.

The diagram of Figure 7.7 shows the percentage of TPI landforms area in ridges at different scales; the log curves of 120,240, and 360 have an intersection point at the upper slope. This point transitions values from a low percentage to a higher percentage of areas.
The correlation value of R^2 between landforms of FA-120 is 0.6. FA-240 is 0.9 well correlated because of the area's proportionality and small percentage interval. For FA-360, the correlation value is 0.6, like FA-120.

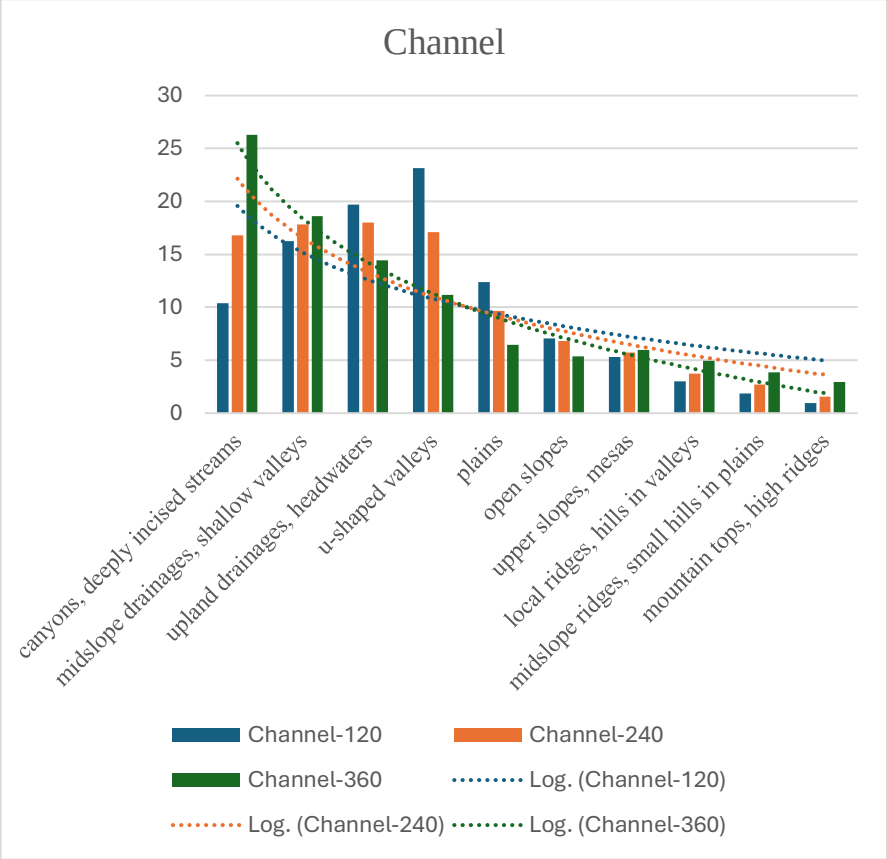

Fig.7.8 diagram of area percentage of TPI landforms containing in Channel at flight altitudes of 120, 240, and 360 meters.

Channels are usually concave areas. In Figure 8, we can see that canyons dominate the area of FA-360. The correlation of area percentage between the landforms of FA-360 is very high, with R^2= 0.97 and a concave logarithmic trend line.
Otherwise, FA-240 has a less concavity logarithmic trend line with R^2= 0.75 due to the proportional percentage of areas between landforms.
Fa-120 has a low correlation between landforms, with R2= 0.35, even less than the average.
We can conclude from these values that due to cartographic generalization and the transition from flight altitude to other, the degree of similarity for channel landform areas rises with the flight altitude. Hence, for ridge land types, the area of canyons and midslope, upper slope local ridge, midslope ridge, and mountain tops increase with flight altitude, upland drainage, u-shaped valley, plain and open slope area decrease with the flight heights.

CONCLUSION

In this study, drone Digital Surface Models (DSM) at diverse flight heights were used as input data. Using the Topographic Position Index and unsupervised classification of Iwahashi and Pike, the study area was classified into landform categories of different-scale DSM. The result shows that ridges and drainage forms are more susceptible to generalization than other forms. The landform classes obtained for the three scales differentiate the dynamic terrain characteristics of the study area. Landform classifications extracted from drone DSM and GIS fast-track the presented results and discussion by integrating the geospatial multiscale approach of terrain analysis.
The result shows that TPI provided a powerful tool for describing topographic attributes of a study area, and there is a relationship between landform maps and spatial resolution. A deep understanding of the terrain characteristics and potential and specific constraints of cartographic generalization. The information and methods discussed in this paper are valuable results for

cartographic multiscale studies and analysis. Landforms are dissolving with scales against each other, some gaining areas and some disappearing. This paper analyzed the generalization at three different scales (flight altitude); for future research, we plan to examine and monitor landform changes at micro, local, and global scales.

Chapter 8

Multiscale Air Temperature Analysis

Many studies on UAVs were conducted, especially for terrain analysis, structure monitoring, and vegetation studies, but meteorological studies, especially in Lebanon, are still very rare.
This paper describes a methodology for collecting meteorological data from UAV platforms and sensors at different flight altitudes. Technological progress, especially unmanned aerial vehicles (UAV) and new photogrammetry software, encourages acquiring and processing Digital Surface Models (DSM) at high spatial resolutions. The scale dependency of land-surface parameters and land-surface objects has been confirmed by several researchers (Chang and Tsai, 1991; Wood, 1996; Florinsky & Kuryakova, 2000; Evans, 2003; Hengl, 2006; Arrell et al., 2007, Deng et al., 2007, Pogorelov and Doumit, 2009, Wood, 2009).
Usually, UAV components are onboard GPS, autonomous chipset, altimeter sensor, wind speed sensor, inertial navigation sensor, and electronic speed controller (Mondragon et al., 2010).
This study aims to add a meteorological sensor to a UAV system for meteorological mapping purposes at very low altitudes, such as 150, 100, and 50 meters.
All flights included sensors to measure relative humidity and air temperatures. The acquired data were then interpolated and mapped, providing additional information for comparison purposes
The primary objectives of the study using UAV include:

- Building reliable high spatial resolution DSM and DOM at different flight heights.
- Sensing air temperature and relative humidity from the aerial platform to characterize a horizontal and vertical profile and evaluate the feasibility of mapping.

Our experiment generated 3 DSMs for the same study area with different spatial resolutions obtained from a UAV survey of different heights. Therefore, the experiment implemented the opportunities for multi-scale measurement technology based on UAVs.
Using unmanned aerial vehicles (UAVs) to conduct measurements in the atmospheric boundary layer can potentially address this need to obtain a spatial description of the structure.
The use of UAVs for meteorological measurements and research is still in its infancy, especially in Lebanon, although initially focusing on remotely piloted meteorological measurements of relative humidity and temperature.

MATERIALS AND METHODS

Our research was carried out on an area of about 5 hectares at a relative altitude of 1250 meters above sea level in the Baskinta region, situated on the western Lebanese mountainous chain (located on the eastern shore of the Mediterranean basin) (Figure 8.1).
Baskinta region. This study area was chosen because it has a varied terrain structure covered by pine trees (Figures 8.1a,8.1b).

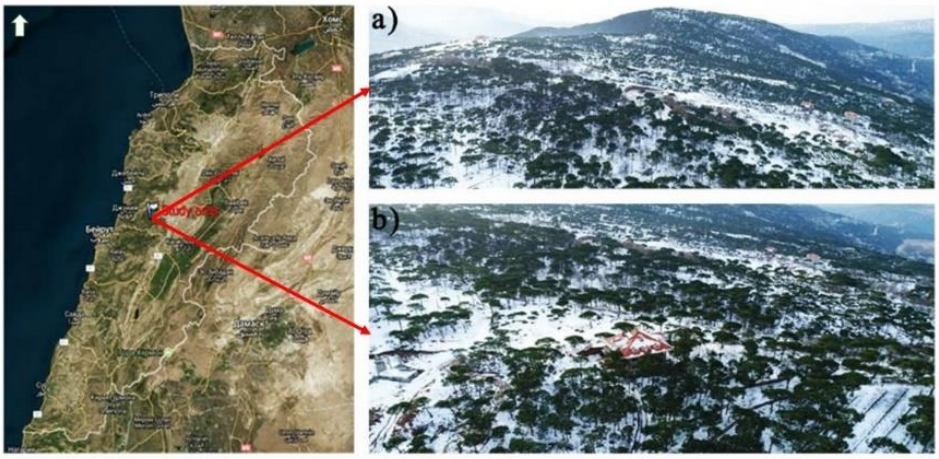

Fig.8.1: The study area is located on the satellite image, with aerial views a) a western view of the location and b) a northern view.

The UAV is a DJI Phantom 4 Pro with a 20-megapixel camera and 4864 x 3648 frame dimensions.
DJI quadcopters have onboard parameters such as navigation systems based on GPS receivers and Inertial measurement units (IMU). These parameters allow the user to set and read waypoints that can be pre-programmed to form a designed flight path.
The meteorological sensor mounted on the DJI Phantom is a Voltcraft DL-120 data logger that records 16000 temperature and humidity readings. It can record an interval from 2 seconds to 24 hours.
DJI ground station flight planning mobile application is used to draw the flight paths of three missions to acquire data over a region of interest at a nominated image scale (Figure 8.2).

Fig.8.2. Flight paths are designed in the DJI ground control flight planning mobile application. The flight rectangle is approximately 196 x 180 m, representing a single flight sequence. a) flight path of 1337 m altitude, b) flight path of 1387 m altitude, c) flight path of 1437m altitude.

Figure 8.2 shows the display of the DJI ground control flight planning mobile application, which is based on Google Maps images and street maps. Three flight missions were designed at different flight altitudes above the sea level, with a flight altitude of 1337 meters (FA-1337) above the sea level translated to a flight height of 50 above a datum (FH-50). The datum of flight heights is the same UAV takeoff point for all missions, figure 8.2b flight altitude of 1387 meters above the sea level (FA-1387) or FH-100, figure 8.2c of FA-1437 meters above the sea level or FH-150.
The flight path followed by the UAV was identical for all the flights FH-50, FH-100, and FH-150. The only difference between them is the flight length. FH-50 consisted of seven parallel strip lines totaling 1566 meters, FH-100 had three strip lines totaling 713 meters, and the last mission, FH-150, had two lines totaling 486 meters.
After drawing flight paths for all missions, the Dji ground station application set the camera shutter interval at 2 seconds synchronized with the meteorological sensor placed on board the UAV. The

acquired images overlapping were set at 80 % and side lapping at 70%. On the first mission, FH-50, 155 vertical frames were acquired at FH-100/40 frames and FH-150/19 frames.
The Angle view for each flying height is the same a1=a2=a3 because the focal length (9 mm) is fixed during aerial image acquisition. Figure 8.3 describes the angle view, scale, and spatial coverage.

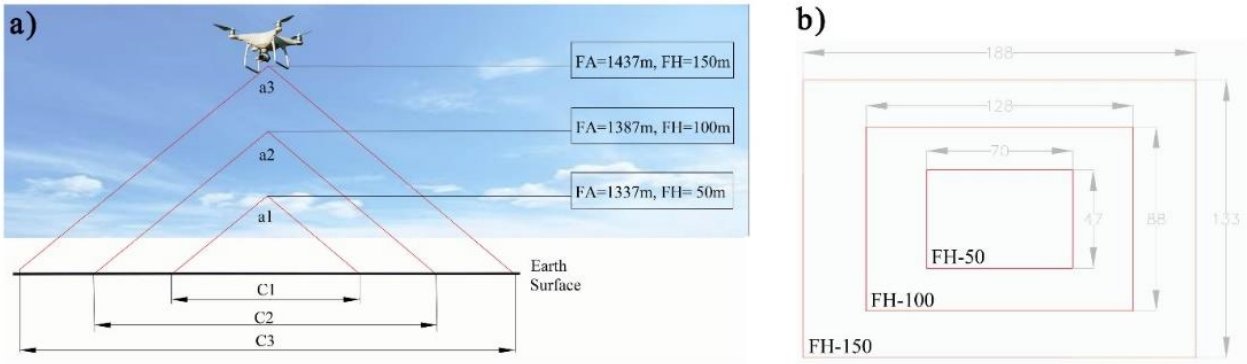

Fig.8.3: a) angles view and image coverage at the three flight heights, b) images ground coverage dimensions.

At the flight height of 150 m, the ground coverage area of one image is C1=188m, and the thickness is 153m. For FH-100, the dimensions of the coverage are 128 x 88 meters, and for FH-50, 70 x 47, three times less than for FH-150.

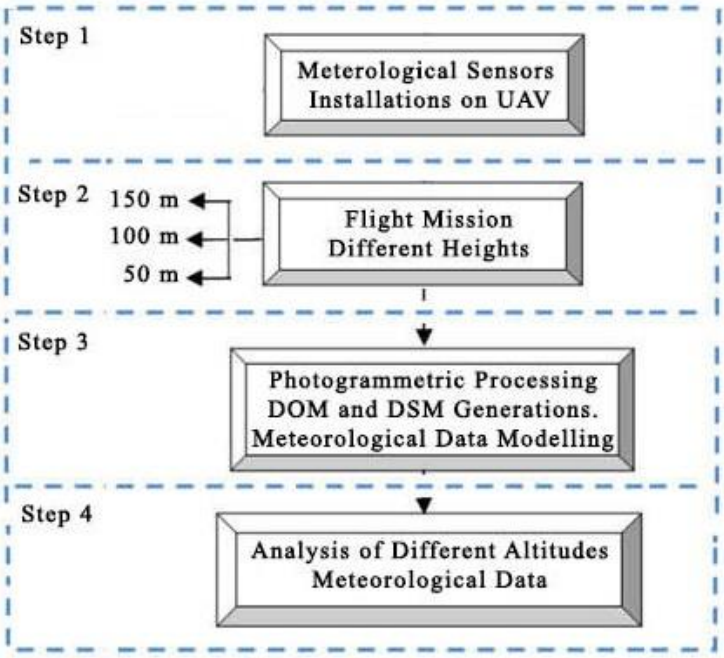

Fig.8.4 Research methodology constituted from four simultaneous steps.

As mentioned above the project begins with step one of figure 8.4, climatological sensor installation on board of the UAV. After the flight planning of step 2, the photogrammetric processes of the flight missions were done in Agisoft Photo scan, a Russian photogrammetric software.
The collected aerial images must be processed to produce usable information.
The processing workflow begins with the stitching of derived aerial images, followed by the production of point clouds, 3D mesh interpolation, and Digital Surface Model (DSM) and Digital Ortho Model (DOM) generations.

The sensor meteorological data are in Excel sheets showing the project date, 21 January 2018, the time of capture, and the temperature and relative humidity values.
The capturing time of each measure is synchronized with the exposure time of aerial frames. The coordinates of the aerial images are known by the UAV GPS and are found in EXIF files. In that way, we associate location data latitudes and Longitudes for the meteorological databases and convert them to points.
These points contain relative humidity and temperature at FH-50, FH-100, and FH-150. The data modeling was done by kriging interpolation.

DISCUSSIONS AND RESULTS

At the end of the geo-processing stage, we summarized a GIS data package containing terrain information (DSM, DOM) and meteorological data (temperature and relative humidity).
Figure 4 shows three DSM of the study area of different spatial resolutions: FA-50 of 50 meters' flight Height with a very good spatial resolution data set of 5 cm highlighting all the terrain details, even rock textures, passing by FA-100 with 10 cm and ending by FA-150 with 15 cm spatial resolution. From the spatial resolution variation of 5 cm between DSMs, we can detect a generalization effect with the «disappear» and «growth» of some terrain morphological features.

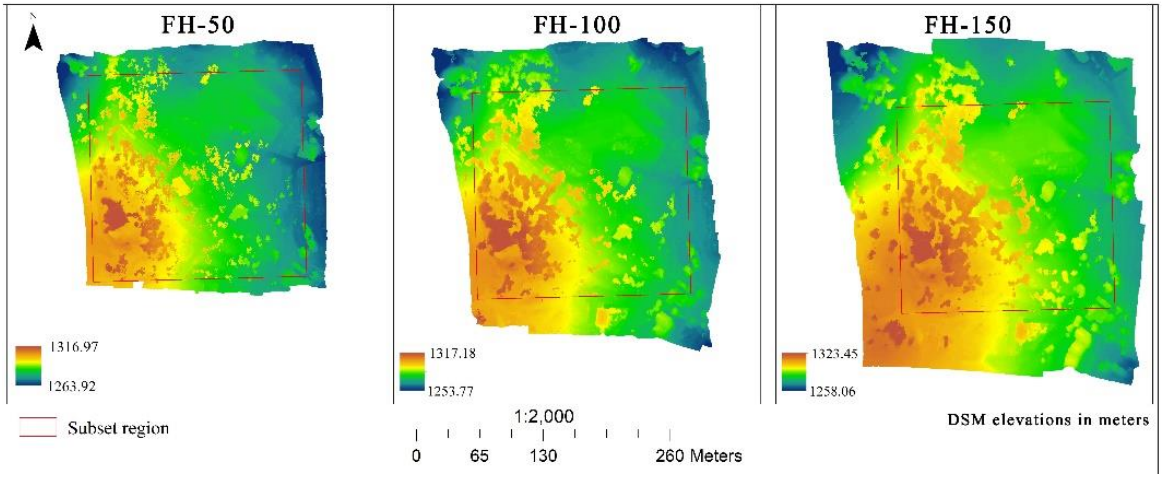

Fig. 8.5 DSMs at different flight heights generated from photogrammetric image processing.

These 3 DSMs were subset by a rectangular region (Figure 8.5) to be similar for all spatial analysis processes and suitable for generalization comparison.

Digital Surface Models (DSM) generated from UAVs contain elevations of all surface elements, such as trees, houses, cars, etc. To get a terrain elevation without surface elements, the DSMs are transformed into DTMs by distributing and interpolating 181 scattered points of natural terrain. In addition to DSMs and DTMS, Digital Ortho Models were generated from photogrammetric processing; Figure 8.6 shows the three DOMs.

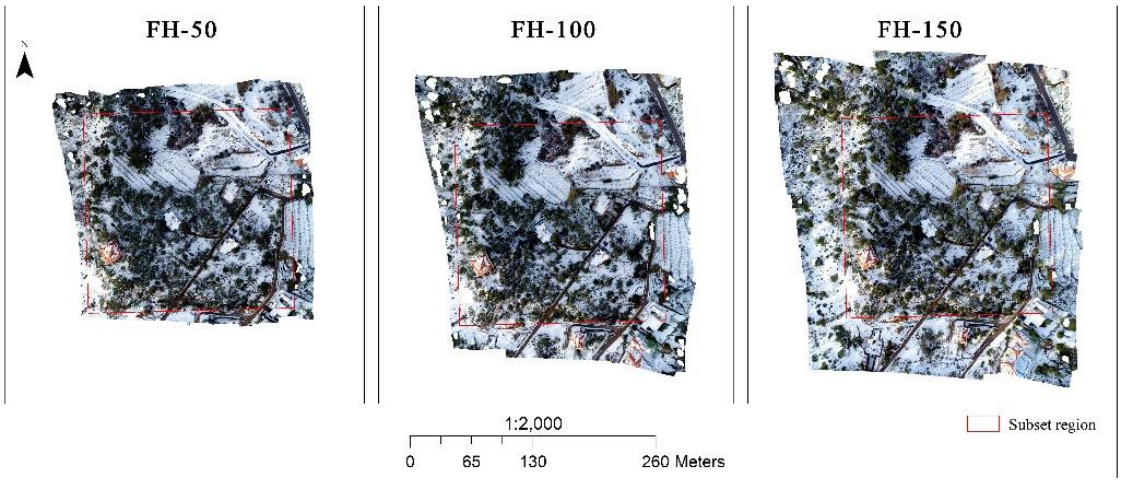

Fig.8.6 DOMs at different flight heights generated from photogrammetric image processing.

In Table 1a, the elevation difference mean values between FH-50 and FH-100 are 30 cm for both models DSM and DTM, which is a good result with a flight altitude of 50 m higher. Otherwise, the difference in mean elevation values between FH-100 and FH-150 is very high, about 7 m; the interval of errors of the difference in mean elevations (DSM, DTM) between FH-100 and FH-150 is very big due to the wind speed recorded at 150 m height and to the absence of ground control points (GCP) corrections.

The comparison value of the minimum elevations in both DSM and DTM at FH-50 and FH-100 is less than 10 cm, contrary to maximum values with an interval of less than one meter.

Based on the captured meteorological data, an Air Temperature and Relative Humidity gradient was observed while a UAV flew in three flights inside the subset polygon. The flight areas recorded measurements of horizontal spatial variation.

Figure 8.7 Atmospheric temperature and humidity horizontal interpolated planes (kriging method).

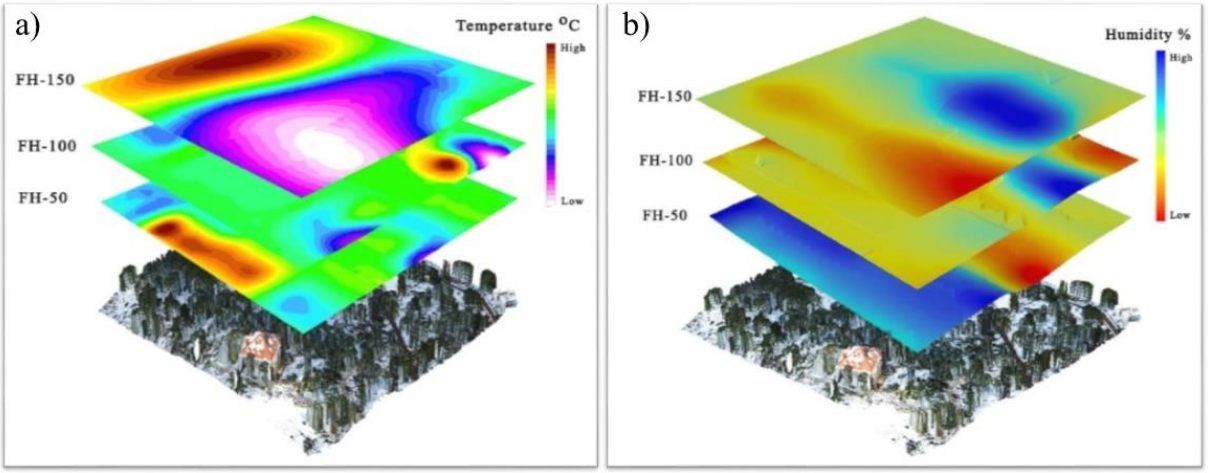

Fig.8.7: a) Temperature maps of three heights, b) Relative humidity at three levels.

The time traces of temperature measured by the UAVs over the three flights are shown in Figure 8.7 and reveal the combined altitude above the ground level and time dependence of temperature over the three flights. For flight FH-50 shown in Figure 8.7a, the profile shows an inversion of temperature at 50 m, decreasing slightly with z below 50 m and increasing at a much higher rate above it. Thus, the first flight FH-50 took place within a developing convective layer with a thickness of approximately 50 m, with the residual stable layer above it. Figure 8.7a also shows the time dependence of the temperature, indicated by the color of the symbol used.

Table 8.1: a) DSM and DTM statistics of the three flight heights, b) Humidity and temperature statistics at the three levels.

a)	DSM (m)				DTM (m)			
	Min	Max	Mean	STD	Min	Max	Mean	STD
FH-50	1269.93	1316.97	1287.79	9.48	1270.19	1312.53	1285.75	8.7
FH-100	1269.81	1317.21	1288.07	10.07	1270.12	1312.11	1286.79	9.49
FH-150	1275.75	1323.52	1294.74	10.18	1277.79	1318.57	1293.12	8.98
b)	Humidity (%)				Temperature (degree Celsius)			
	Min	Max	Mean	STD	Min	Max	Mean	STD
FH-50	24.33	33.17	29.03	1.93	6.82	7.47	7.17	0.09
FH-100	28.24	33.4	30.13	0.78	5.41	8.06	6.82	0.22
FH-150	29.99	34.08	31.99	0.82	5.77	6.35	6.02	0.17

The general atmospheric situation on January 21st, 2018, is characterized by stability. The synoptic situation of the surface shows a center of high pressure above Lebanon (1020 hpa) and the Middle East. At an altitude of 500 hpa, a peak reigns above the area to accentuate stability (Figure 8.8). This stability is favorable for measuring humidity and temperature at different altitudes.

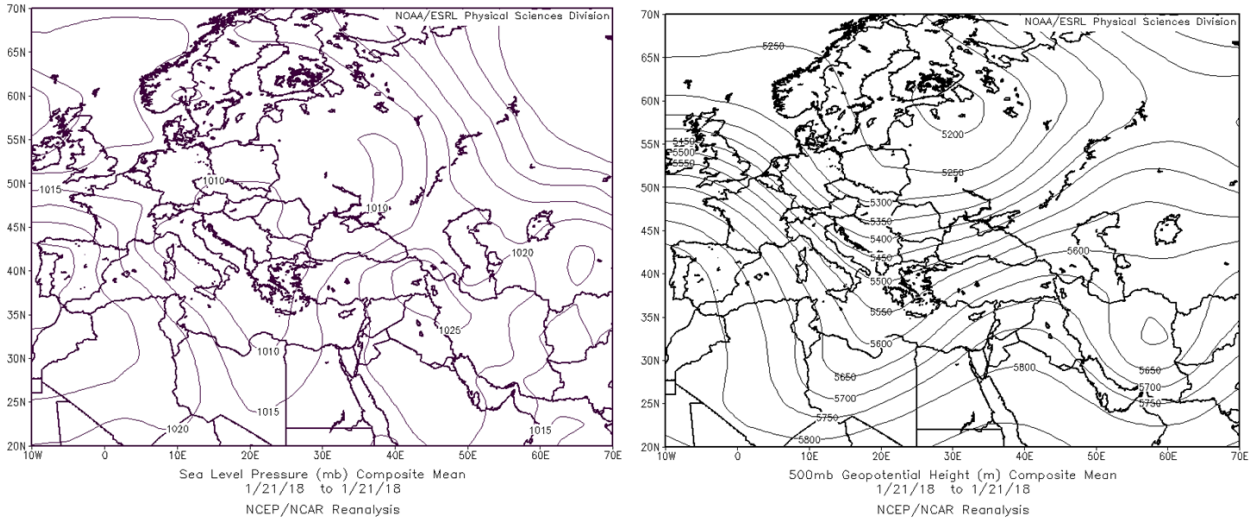

Fig. 8.8: Map of surface pressure and altitude on 1/21/2018 above the Middle East.

In a general way, the temperature depends on the pressure. The more the pressure increases, the more the temperature is high. Under comparable weather conditions, the highest temperatures are measured with the sea level, with the highest air pressure on the sea level. With the rise in altitude, the expressed temperature decreases with pressure, and the air temperature decreases with the altitude at an average of 0.6°C per meter. It is the "vertical atmospheric variation in temperature" (figure 8.9).

In addition to the pressure, the type of atmosphere warming plays a central role. The surface of the Earth mainly heats the atmosphere. That means that the solar radiation short wavelengths heat the terrestrial surface. The surface, thus heated, emits a large thermal radiation wavelength to the atmosphere above.

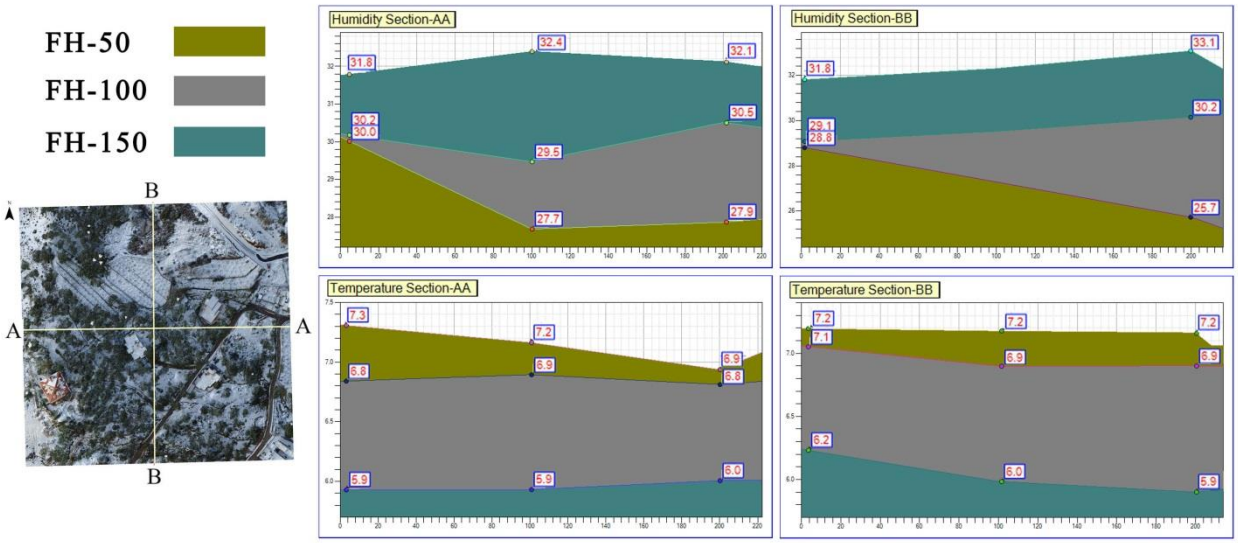

Fig. 8.9 Map of the temperature reduction on 3 levels: 50, 100, and 150 meters.

The more the atmosphere contains steam (gas, invisible), the more it can absorb thermal radiation. An atmospheric layer, thus heated, becomes a thermal radiation source, re-emitting the heat it absorbs. Most of this heat of the atmosphere is returned in the direction of the terrestrial surface. It is called atmospheric against-radiation; it acts here in the form of long waves. This against-radiation is also active during the night. (The process, including the entering radiation short wavelengths and the atmospheric against-radiation big wavelengths, is anything else, only the natural greenhouse effect.)

The content of humidity in the atmosphere depends on the pressure. The pressure decreases with altitude, and humidity content becomes increasingly weak (Table 8.1, b). This is why the higher one reaches altitude, the less the atmosphere can absorb thermal radiation and reflect it toward the Earth. With altitude, the atmosphere becomes increasingly permeable to the heat sent by the Earth's surface. No absorptive heat is lost then in space.

When hot air rises, it dilates upwards as the pressure decreases. The expansion of the air requires energy, which is drawn from transported heat. Thus, the ascending air cools as it goes up in altitude and dilates.

CONCLUSION

UAVs are new surveying instruments for the earth's surface using DSM and DOM processing. For a representative area in the mountains of Lebanon, drone experiments have been performed with variable flight heights at 50, 100, and 150 meters.

Scale and resolution effects on terrain data have been and will continue to be important issues in geographic research. DSM UAV-based methods should be tested before their application. A good understanding of the effects of scale on the analysis results is essential.

A recording sensor of type HD-200 measures the temperature and relative humidity. It is fixed on the drone used to make a vertical and horizontal cut of the atmosphere, dividing it into three layers: 50, 100, and 150 meters. The temperature and relative humidity results showed that these weather parameters decrease with altitude.

For future meteorological experiments, we plan to integrate pollution detection sensors, temperature, and relative humidity to model multi-temporal pollution maps.

REFERENCES

1. Aksoy, H., Kavvas, M.L. (2005). A review of hillslope and watershed scale erosion and sediment transport models. Catena 64, 247-271. Doi: 10.1016/j.catena.2005.08.008
2. Angima, S. D., Stott, D. E., O'Neill, M. K., Ong, C. K. & Weesies, G. A. (2003). Soil erosion prediction using RUSLE for central Kenya highland conditions. Agric. Ecosys. Environ., 97: 295-308. Doi: 10.1016/S0167- 8809(03)00011-2
3. Arrell K, Fisher P.F, Tate N.J, Bastin L (2007). A fuzzy c-means classification of elevation derivatives to extract the morphometric classification of landforms in Snowdonia, Wales. Computers & Geosciences 33, pp.1366–1381.
4. Barka I, Vladovic J, Malis F (2011). Landform classification and its application in predictive mapping of soil and forest units. Proceedings: GIS Ostrava 2011.
5. Beasom S. L., Wiggers E. P., Giordono R. J. (1983). A technique for assessing land surface ruggedness. Journal of Wildlife Management. 47: pp. 1163–1166.
6. Beven K. J.: Rainfall-Runoff Modelling. The Primer. John Wiley & Sons Ltd., Chichester (2001).
7. Blyth E. M., Finch J., Robinson M., Rosier P. (2004). Can soil moisture be mapped onto the terrain? Hydrology and Earth System Sciences 8,923-930.
8. Burrough, P.A. (1983). Multiscale sources of spatial variation in soil- the application of fractal concepts to nested levels of soil variation, J. Soil Sci., 34, 577, 1983.
9. Canuto, A., M. Fairhurst, & G. Howells. (2003). Fuzzy connectives as a combination tool in a hybrid multi-neural system. Int. J. Neural Syst. 13, 67–76. Doi: 10.1142/S0129065703001455.
10. Cao, C., N. Lam, S.N. (1997). Understanding the scale and resolution effects in remote sensing and GIS. D. A. Quattrochi and M. F. Goodchild, eds., Scale in Remote Sensing and GIS., pp.57-72.
11. Casalí, J., Loizu, J., Campo, M. A., De Santisteban, L. M., and Álvarez-Mozos, J. (2006). Accuracy of methods for field rill and ephemeral gully erosion assessment, Catena, 67. pp. 128–138.
12. Casasnovas, J.A., Ramos, M.C., Ribes-Dasi, M. (2002). Soil erosion caused by extreme rainfall events: mapping and quantifying agricultural plots from detailed digital elevation models. Geoderma 105. pp.125–140. DOI: 10.1016/S0016-7061(01)00096-9.
13. Castillo, C., Pérez, R., James, M.R., Quinton, N.J., Taguas, E.V., Gómez, A. (2012). Comparing the accuracy of several field methods for measuring gully erosion. Soil Science Society of America Journal 76. pp.1319–1332.
14. Chang, K., Tsai, B. (1991). The effect of DEM resolution on slope and aspect mapping. Cartography and Geographic Information Science 18, pp. 69–77
15. Chaubey, I., Cotter, A. S., Costello, T. A. and Soerens, T. (2005). Effect of DEM data resolution on SWAT output uncertainty. Hydrol. Proc. 19(3). pp. 621-628.
16. Daggupati, P., Douglas-Mankin, K. R., Sheshukov, A.Y. (2013). Predicting ephemeral gully location and length using topographic index models. Transactions of the ASABE, American Society of Agricultural and Biological Engineers Vol. 56(4). pp. 1427–1440. ISSN 2151-0032.
17. Dahl, A.L. (1973). Surface area in ecological analysis: quantification of benthic coral-reef algae. Mar Biol., 23, pp.239–249.
18. Deng, Y., Wilson, J.P., Bauer, B.O. (2007). DEM resolution dependencies of terrain attributes across a landscape. International Journal of Geographical Information Science 21, pp. 187–213.
19. Desmet, P. J. J., & Govers, G. (1996). Comparison of routing algorithms for digital elevation models and their implications for predicting ephemeral gullies. Int J Geogr Inf Sci, 10, 311-332.

20. Desmet, P. J. J., Poesen, J. Govers, G. and Vandaele, K. (1999). Importance of slope gradient and contributing area for optimal prediction of the initiation and trajectory of ephemeral gullies. Catena 37(3-4) pp. 377-392.
21. Doumit, J.A. (2017). Digital Terrain Analysis of Lebanon: A Study of Geomorphometry-Krasnodar, Kuban State University,2017, p.161.
22. Doumit, J.A., Kiselev, E.N. (2018). Measurement of Lebanese river basin dissection (erosion intensity) based on ALOS WORLD 3D.// "National scientific and practical conference, Integral and differential paradigms of science and practical development of Russia." St Petersburg- Russia, pp.23-28.
23. Doumit, J.A., Pogorelov, A.V. (2017). Multi-scale Analysis of Digital Surface Models Based on UAV Datasets. Modern Environmental Science and Engineering (ISSN 2333-2581), Volume 3, No. 7, pp. 460-468.
24. Doumit, J. A. (2017). Digital Terrain Analysis of Lebanon: A Study of Geomorphometry-Krasnodar. In Scientific edition polygraph center Kuban State University (p. 161).
25. Doumit, J.A. (2018). Multiscale Landforms Classification Based on UAV Datasets. Sustainability in Environment, Vol. 3, No. 2. doi:10.22158/se. v3n2p128. www.scholink.org/ojs/index.php/se
26. Doumit, J.A., Awad, S.F. (2019). DEM Spatial Resolution Impact on Hillslope Erosion and Deposition Modeling, an Application on Lebanese Watersheds. Sustainability in Environment, Vol. 4, No. 2, 2019. http://dx.doi.org/10.22158/se.v4n2p75.
27. Doumit, J.A., Kiselev, E.N. (2016). Structure from motion technology for macro-scale objects cartography// Breakthrough scientific research as the modern engine of sciences, St. Petersburg.: Publishers "Cult Inform Press." pp 42-47.
28. Du Preez, C. (2014). "A new arc-chord ratio (ACR) rugosity index for quantifying three-dimensional landscape structural complexity." Landscape Ecology. 2014, 30, pp. 181–192.
29. Du Preez, C., Tunnicliffe V. (2011). Shortspine thornyhead and rockfish (Scorpaenidae) distribution in response to substratum, biogenic structures, and trawling. Mar. Ecol. Prog. Ser. 2011, 425, pp. 217-231. (doi:10.3354/meps09005).
30. Dubertret, L. and Wetzel, R. (1951). 1 / 50,000 Geological Map, Zahleh Sheet, Explanatory Note, Lebanese Republic, Min. public works, Beirut, Lebanon, 68p.
31. Dunn, M., & Hickey, R. (1998). The effect of slope algorithms on slope estimates within a GIS. Cartography, vol. 27, no. 1, pp. 9–15.
32. Eastman, J.R. (1985). Single-Pass Measurement of the Fractional Dimensionality of Digitized Cartographic Lines. Paper presented to the Canadian Cartographic Association, Annual Meeting, June 1985.
33. Elliot J. K. (1989). An investigation of the change in surface roughness through time on the foreland of Austre Okstindbreen, North Norway," Comput. Geosci., vol. 15, no. 2, pp. 209–217.
34. Environmental Systems Research Institute (ESRI) (1997). Arc/Info, version 7.2, Online Users Guide.
35. Evans, I. (2003). Scale-specific landforms and aspects of the land surface. In: Evans, I.S., Dikau R., Tokunaga E, Ohmori H, Hirano M. (Eds.), Concepts and Modelling in Geomorphology: International Perspectives. Terrapub, Tokyo, pp. 61–84.
36. Evans, I. S. (1972). General geomorphometry, derivatives of altitude, and descriptive statistics in Spatial Analysis in Geomorphology. New York: Harper & Row, 1972, pp. 17–90.
37. Evans, S. (1990). "General Geomorphometry". In: Goudie, A.S., Anderson M., Burt T., Lewin, J., Richards, Whalley K., Worsley B., Geomorphological Techniques. 2nd edition. Unwin Hyman, London, pp.44–56.

38. Evans, I.S. (2003). Scale-specific landforms and aspects of the land surface. In: Evans, I.S., Dikau, R., Tokunaga, E., Ohmori, H., Hirano, M. (Eds.), Concepts and Modelling in Geomorphology: International Perspectives. Terrapub, Tokyo, pp. 61–84.
39. Flacke, W.,Auerswald, K.,Neufang, L. (1990). Combining a modified USLE with a digital terrain model for computing high-resolution maps of soil loss resulting from rain wash. Catena, 17, 383-397.
40. Florinsky I. V, Kuryakova G.A. (2000). Determination of grid size for digital terrain modeling in landscape investigations-exemplified by soil moisture distribution at a micro-scale. International Journal of Geographical Information Science 14, pp. 815–832.
41. Florinsky, I. V. (1998). Accuracy of local topographic variables derived from digital elevation models. International Journal of Geographical Information Systems, pp. 12, 47–61.
42. Foster, G.R. Wischmeier, W.H. (1974). "Evaluating Irregular Slopes for Soil Loss Prediction". American Society of Agricultural Engineers Transactions 17. 305-309.
43. Friedman, A., Pizarro, O., Williams, S.B., Johnson-Roberson, M. (2012). Multi-scale measures of rugosity, slope, and aspect from benthic stereo image reconstructions. PLoS One 7, 12, pp. 1–14.
44. Galparsoro, I., Borja,A., Bald, J., Liria, P., Chust, G. (2009). Predicting suitable habitat for the European lobster (Homarus gammarus), on the Basque continental shelf (Bay of Biscay), using Ecological-Niche Factor analysis. Ecol Model, 220, pp. 556–567.
45. Garcia Rodriguez, J. L., & Gimenez Suarez, M. C. (2012). Methodology for estimating the topographic factor LS of RUSLE3D and USPED using GIS. Geomorphology, 175-176, 98-106.
46. Gerçek, D. (2010). "Object-based classification of landforms based on their local geometry and geomorphometric.
47. Gonzalez, M.F. and Wintz, P. (1987). Digital Image Processing, Addison Wesley, Menlo Park, CA, 414, 1987.
48. Goodchild, M.F. & Mark, D.M. (1987). The fractal nature of geographic phenomena. Ann. Assoc. Am. Geogr., 77, 265.
49. Grohmann, C., Smith, M., Riccomini, C. (2011). Multiscale analysis of topographic surface roughness in the Midland Valley, Scotland, IEEE T. Geosci. Remote, 49, 1200–1213.
50. Grunwald, S. (2006). What do we really know about the space-time continuum of soil-landscapes? In S. Grunwald (Ed.), Environmental soil-landscape modeling (pp. 3-36). CRC Press, Taylor & Francis Group, Boca Raton.
51. Guntner A., Seibert J., Uhlenbrook S. (2004). Modeling spatial patterns of saturated areas: An evaluation of different terrain indices. Water Resources Research ,40,W05114.
52. Haan, C.T., B.J. Barfield, & J.C. Hayes (1994). Design Hydrology and Sedimentology for Small Catchments. Academic Press, San Diego, California, USA. 588 pp.
53. Hakim, B. (1985). Hydrological and hydrochemical research on some Mediterranean karsts Lebanon, Syria, and Morocco. Publications of the Lebanese University, Beirut, Lebanon. 701 p., 6 maps.
54. Hengl, T. (2006). Finding the right pixel size. Computers & Geosciences 32, pp. 1283–1298.
55. Hengl, T., Evans, I.S. (2009). Mathematical and digital models of the land surface. In: Hengl T, Reuter, H.I (Eds.), Geomorphometry — Concepts, Software, Applications. Developments in Soil Science, vol. 33. Elsevier, Amsterdam, pp. 31–63.
56. Hengl, T. (2006). Finding the right pixel size. Computers & Geosciences 32, 1283–1298, 2006.
57. Herzfeld, U. C., Mayer, H., Feller, W., Mimler, M. (2000). Geostatistical analysis of glacier-roughness data, Ann. Glaciol., 2000, vol. 30, no. 1, pp. 235–242.

58. Hickey, R. (2000). Slope angle and slope length solutions for GIS. Cartography, vol. 29, no. 1, pp. 1–8.
59. Hobson R. D. (1972). Surface roughness in topography: quantitative approach. In R. J. Chorley, editor. Spatial analysis in geomorphology. Harper and Row, New York, New York, USA, pp. 221–245.
60. Hofierka, J. (1992). Interpolation, morphometric analysis of relief, and modeling water erosion. M.S. thesis, Comenius University, Bratislava, Slovakia, p. 54. (in Slovak)
61. Holmes, K. W., Chadwick, O. A., and Kyriakidis, P. C. (2000). Error in a USGS 30-meter digital elevation model and its impact on terrain modeling. J. Hydrol. 233(1). pp.154-173.
62. Huang, S.L., Ferng, J.J., (1990). Applied Land Classification for Surface Water Quality Management: 2. Land Process Classification. Journal of Environmental Management, 31, 127-141.
63. Hutchinson, M. F. (1996). A locally adaptive approach to the interpolation of digital elevation models. In The Proceedings of Third International Conference/Workshop on Integrating GIS and Environmental Modeling. pp. 21–26. Santa Fe, NM.
64. Iwahashi, J. & Pike, R. J. (2007). "Automated classifications of topography from DEMs by an unsupervised nested-means algorithm and a three-zone geometric signature," Geomorphology, vol. 86, no. 3/4, pp. 409–440.
65. James, M.R., Robson, S. (2012). Straightforward reconstruction of 3D surfaces and topography with a camera: Accuracy and geosciences applications. Journal of Geophysical Research 117. pp1–17. DOI: 10.1029/2011JF002289.
66. Jenness, J. (2005). Topographic Position Index. Extension for ArcView 3.x. http://jennessent.com.
67. Jenness, J. (2010). "Topographic Position Index (tpi_jen.avx) extension for ArcView 3.x", v. 1.3a. Jenness Enterprises, http://www.jennessent.com/arcview/tpi.htm.
68. Jenness, J. (2004). "Calculating landscape surface area from digital elevation models." Wildlife Society Bulletin 32.3, 2004, pp. 829–839.
69. Jenson, S. K. (1991). Application of hydrologic information automatically extracted from digital elevation models. Hydrological Processes, pp. 5, 31–44.
70. Jha, V. C. (1996). Himalayan Geomorphology. Rawat Publishing Co, Jaipur, and New Delhi, 1996. p.112 – 144.
71. Kennelly, P.J. (2008). Terrain maps displaying hill-shading with curvature. Geomorphology 102, 567-577. Doi: 10.1016/j. geomorph.2008.05.046.
72. Kienzle, S. W. (2004). The effect of DEM raster resolution on first-order, second-order, and compound terrain derivatives. Transactions in GIS 8,83-111.
73. King, C., N. Baghdadi, Lecomte, V., and Cerdan, O. (2005). The application of remote-sensing data to monitoring and modeling of soil erosion. Catena 62, 79-93. Doi: 10.1016/j. Catena.2005.05.007
74. Koeln, G.T., Cowardin, L.M. (1996). Strong, L.L. Geographical information systems. in T.A. Bookhout, ed. Research and management techniques for wildlife and habitats. Fifth ed., rev. The Wildlife Society, Bethesda MD., pp. 540–566.
75. Kothyari, U. C., Jain, M. K., & Ranga-Raju, K. G. (2002). Estimation of temporal variation of sediment yield using GIS. In Hydrological Sci J des Sci Hydrol, 47(5), 693-706.
76. Lam, N. and Quattrochi, D.A. (1992). On the issues of scale, resolution, and fractal analysis in the mapping sciences, Prof. Geogr., 44.88.
77. Leh, M., Bajwa, S., & Chaubey, I. (2011). Impact of land use change on erosion risk: An integrated remote sensing, geographic information system, and modeling methodology. In Land Degrad. Dev, 24(5), 409-421.
78. Levin, S.A. (1992). The problem of pattern and scale in ecology. Ecology, 73, pp. 1943–1967.

79. Li, Z. (1993). Mathematical models of the accuracy of digital terrain model surfaces linearly constructed from gridded data, Photogrammetric Record, (82): 661-674.
80. Li, Z. (2008). Multi-scale digital terrain modeling and analysis. In: Zhou, Q., Lees, B., Tang, G. (Eds.), Advances in Digital Terrain Analysis. Springer, Berlin, Heidelberg, pp. 59 83.
81. Liu, S., Bliss, N., Sundquist, E., & Huntington, T. G. (2003). Modeling carbon dynamics in vegetation and soil under the impact of soil erosion and deposition. Global Biogeochem. Cycles, 17(2), 1074.
82. Logan, T. A.; Nicoll, J.; Laurencelle, J.; Hogenson, K.; Gens, R.; Buechler, B.; Barton, B.; Shreve, W.; Stern, T.; Drew, L.; Guritz, R. (2014). Radiometrically Terrain Corrected ALOS PALSAR Data Available from the Alaska Satellite Facility. American Geophysical Union, Fall Meeting 2014, abstract id. IN33B-3762. 12/2014.
83. Lundblad, E.R., Wright, D.J., Miller, J., Larkin, E.M., Rinehart, R., Naar, D.F., Donahue, B.T., Anderson, S.M., Battista, T. A. (2006) benthic terrain classification scheme for American Samoa. Mar Geod. 29, pp. 89–111.
84. MacMillan, R.A., Shary, P.A. (2009) Landforms and landform elements in geomorphometry. In: Hengl, T., Reuter, H.I. (Eds.), Geomorphometry—Concepts, Software, Applications. Developments in Soil Science, vol. 33. Elsevier, Amsterdam, pp. 227–254.
85. Mark, D. M. (1983). In Automated detection of drainage networks for digital elevation models (pp. 288-289). Proceedings of Auto-Carto, 6, Ottowa, Ontario, Canada.
86. Mark, D.M. (1975). Geomorphometric parameters: A review and evaluation, Geografiska Annaler. Ser. A, Phys. Geography, 1975, vol. 57, no. 3/4, pp. 165– 177.
87. Mark, D. M., and Aronson, P. B. (1984). Scale-dependent fractal dimensions of topographic surfaces: an empirical investigation, with applications in geomorphology and computer mapping, Math. Geol., 11,671.
88. Martínez, L.J. and N.A. Correa. (2016). Digital elevation models to improve soil mapping in mountainous areas: a case study in Colombia. pp. 377–388. In: Zinck, J.A., G. Metternicht, G. Bocco, and H.F. Del Valle (eds.). Geopedology is an integration of geomorphology and pedology for soil and landscape studies. Springer International Publishing, Cham, Switzerland.
89. McCormick, M.I. (1994). Comparison of field methods for measuring surface topography and their associations with a tropical reef fish assemblage. Marine Ecology Progress Series 112, pp. 87-96.
90. Merritt, W.S., Letcher, R.A., and Jakeman, A.J. (2003). A review of erosion and sediment transport models. Environ. Modell. Softw. 18, 761-799. Doi: 10.1016/S1364-8152(03)00078-1
91. Minár, J., Jenčo, M., Evans, I., Minár, J. Jr., Kadlec, M., Krcho, J, Pacina, J., Burian, L., Benová, A. (2013) Third-order geomorphometric variables (derivatives): definition, computation and utilization of changes of curvatures, International Journal of Geographical Information Science, 27:7, 1381-1402, DOI:10.1080/13658816.2013.792113.
92. Mitasova, H., & Mitas, L. (2001). Multiscale soil erosion simulations for land use management. In R. Harmon, & W. Doe (Eds.), Landscape erosion and landscape evolution modeling (pp. 321-347). Kluwer Academic/Plenum, New York.
93. Mitasova, H., Hofierka, J., Zlocha M., Iverson, L. R. (1996) Modelling topographic potential for erosion and deposition using GIS, International Journal of Geographical Information Systems, 10:5, 629-641, DOI: 10.1080/02693799608902101
94. Mitasova, H., Iverson, L. (1992). Erosion and sedimentation potential analysis for Hunter Lake. An environmental assessment of the Hunter Lake project area, edited by W.U. Brigham and A.R Brigham (Illinois Natural History Survey Champaign, Illinois)

95. Mitasova, H., Mitas, L., Brown, W. M., & Johnston, D. (1999). Terrain modeling and soil erosion simulations for Fort Hood and Fort Polk test areas. University of Illinois, Urbana- Champaign, IL
96. Momm, H. G., Bingner, R. L., Wells, R. and Dabney, S. D. S. (2011). Analysis of topographic attributes for identification of ephemeral gully channel initiation in agricultural watersheds. ASABE Paper No. 1111250. St. Joseph, Mich.: ASABE.
97. Mondragon, I.F., Olivares-Mendez, M.A., Campoy, P., Martinez, C., Mejias, L. (2010). Unmanned aerial vehicles UAVs attitude, height, motion estimation, and control using visual systems. Autonomous robotics, 29, pp. 17-34.
98. Montgomery, D.R., Dietrich, W.E. (1988). Where do channels begin? Nature 336. pp. 232-234.
99. Moore, I. D. (1996). Hydrologic modeling and GIS. In M. F. Goodchild, L. T. Steyaert, B. O. Parks, C. Johnston, D. Maidment, M. Crane, & S. Glendinning (Eds.), GIS and environmental modeling: Progress and research issues (pp. 143-148). GIS World Books, Fort Collins CO.
100. Moore, I. D., & Wilson, J. P. (1992). Length-slope factors for the Revised Universal Soil Loss Equation: Simplified method of estimation. In J Soil Water Conserv, 47, 423-428.
101. Moore, I. D., Burch, G. J. and Mackenzie, D. H. (1988). Topographic effects on the distribution of surface soil water and the location of ephemeral gullies. Trans. ASAE 31(4). pp. 1098-1107.
102. Moore, I. D., Grayson, R. B., Ladson, A. R. (1991) "Digital Terrain Modeling: A Review of Hydrological, Geomorphological, and Biological Application," Hydrological Processes, Vol. 5, No. 1, p. 3. doi:10.1002/hyp.3360050103.
103. Moore, I. D., Turner, A. K., Wilson, J. P., Jenson, S. K., & Band, L. E. (1993). GIS and land-surface-subsurface process modeling. In M. F. Goodchild, B. O. Park, & L. T. Styaert (Eds.), Environmental Modeling with GIS (pp. 213-230).
104. Moser, K., Ahn, C., Noe, G. (2007) Characterization of microtopography and its influence on vegetation patterns in created wetlands. Wetlands, 27, pp. 1081-1097.
105. Murphy, P. N. C., Ogilvie, J., & Arp, P. (2009). Topographic modeling of soil moisture conditions: A comparison and verification of two models. Eur J Soil Sci, 60, 94-109.
106. Nachtergaele, J., Poesen, J. (1999). Assessment of soil losses by ephemeral gully erosion using high-altitude (stereo) aerial photographs. Earth Surface Processes and Landform 24. pp. 693–706. DOI: 10.1002/(SICI)1096-9837(199908)24:8<693: AID-ESP992>3.0.CO;2-7.
107. Nellis, M.D. and Briggs, J.M. (1989). the effect of spatial scale on Konza landscape classification using textural analysis, landscape ecol.,2,93.
108. Neteler, M. and Mitasova, H. (2008). Open-source GIS: a GRASS GIS approach. 3rd ed. Springer, New York, NY.
109. Nir, D. (1957). "The Ratio of Relative and Absolute Altitude of Mt. Carmel." Geographical Review 27: 564-569.
110. Oliveira, A. H., da Silva, M. A., Silva, M. L. N., Curi, N., Neto, G. K., & de Freitas, D. A. F. (2013). Development of topographic factor modeling for application in soil erosion models. In M. C. Hernandez Soriano (Ed.), Soil processes and current trends in quality assessment. Tech, Rijeka, Croatia.
111. Parker, C., Thorne, C. Bingner, R. Wells, R. and Wilcox, D. (2007). Automated mapping of potential for ephemeral gully formation in agricultural watersheds laboratory. Publication No. 56. Oxford, Miss.: USDA-ARS National Sedimentation Laboratory.
112. Parkner, T., Page, M.J., Marutami, T., Trustrum, N.A. (2006). Development and controlling factors of gullies and gully complexes. East coast, New Zealand. Earth Surface Processes and Landforms 31. pp. 187–199. DOI: 10.1002/esp.1321.

113. Patton, P.C., Schumm, S.A. (1975). Gully Erosion, Northwestern Colorado: a threshold phenomenon. Geology 3. pp. 88–90. https://doi.org/10.1130/0091-7613(1975)3<88: GENCAT>2.0.CO;2.
114. Phillips, J.M., Webb, B.W., Walling, D.E. and Leeks, G.J.L. (1999). Estimating the suspended sediment loads of rivers in the LOIS study area using infrequent samples. Hydrological Processes 13: 1035–50.
115. Pike R. J. (2002). A bibliography of terrain modeling (geomorphometry), the quantitative representation of topography - supplement 4.0., Open-File Rep. No. 02-465. U.S. Geological Survey, Denver, p. 116.
116. Pike, A. C. Mueller, T. G. Schörgendorfer, A Shearer S. A. and. Karathanasis, A. D. (2009). "Erosion Index Derived from Terrain Attributes Using Logistic Regression and Neural Networks," Agronomy Journal, Vol. 101, No. 5,2009, p. 1068. doi:10.2134/agronj2008.0207x.
117. Pogorelov, A.V. and Doumit, J.A. (2009). Relief of Kuban River basin: Morphometric analysis. M.: GEO, p.208. (In Russian)
118. Rasemann, S., Schmidt, J., Schrott, L., Dikau, R. (2004). "Geomorphometry in mountain terrain". In: Bishop, M.P., Shroder, J.F. eds. GIS & Mountain Geomorphology. Springer, Berlin, pp.101–145.
119. Reynolds, K. (2001). NetWeaver: a knowledge-based development system. United States Department of Agriculture (USDA) – Forest Service, Washington DC.
120. Ries, J.B., Marzolff, I. (2003). Monitoring of gully erosion in the Central Ebro Basin by large-scale aerial photography was taken from a remotely controlled blimp. Catena 50. pp. 309–328. https://doi.org/10.1016/S0341-8162(02)00133-9
121. Riley, S.J., DeGloria, S. D., Elliot, R. A. (1999). Terrain ruggedness index that quantifies topographic heterogeneity. Intermountain journal of sciences, Vol.5, No. 1-4.
122. Risk, M.J. (1972). Fish diversity on a coral reef in the Virgin Islands. Atoll Research Bulletin 193, pp. 1-6.
123. Saulnier G.-M., Obled C., Beven K. (1997). Analytical compensation between DTM grid resolution and effective values of saturated hydraulic conductivity within the TOPMODEL framework. Hydrological Processes 11, pp.1331-1346.
124. Shary, P.A. (1995). Land surface in gravity points classification by a complete system of curvatures. Mathematical Geology, 27, 373–390.
125. Shary, P.A., Sharaya, L.S., Mitusov, A.V. (2002). Fundamental quantitative methods of land surface analysis. Geoderma 107, 1–32.
126. Shrestha, D. P. (1997). Assessment of soil erosion in the Nepalese Himalaya: a case study in LikhuKhola valley, Middle Mountain region. Land Husbandry, International Journal of Soil Erosion and Conservation, 2(1): 59-80
127. Smith, G. H. (1935). The relative relief of Ohio. Geographical Review, 25: 272-284.
128. Srinivasan, R. and Engel, B.A. (1991) Effect of slope prediction methods on slope and erosion estimates. Applied Engineering in Agriculture, 7(6), 779 – 783.
129. Stambaugh M.C., Guyette R.P. (2008). Predicting spatio-temporal variability in fire return intervals using a topographic roughness index. For Ecol Manag, 254(3), pp. 463–473.
130. Stieglitz M., Shaman J., McNamara J., Engel V., Shanley J., Kling G. W. (2003). An approach to understanding hydrologic connectivity on the hillslope and the implications for nutrient transport. Global Biogeochemical Cycles 17 ,1105.
131. Stone R. O., Dugundji J. A. (1965) study of micro relief-Its mapping, classification and quantification by means of a Fourier analysis, Eng. Geol., vol. 1, no. 2, pp. 89–187.

132. Tagil S. & Jenness J (2008) GIS-based automated landform classification and topographic, Landcover, and geologic attributes of landforms around the Yazoren Polje, Turkey. Journal of Applied Sciences 8(6): 910-921.
133. Takaku, J., Tadono, T., Tsutsui, K., & Ichikawa, M. (2016). Validation of "AW3D" Global DSM Generated from ALOS PRISM, ISPRS Annals of the Photogrammetry. Remote Sensing and Spatial Information Sciences, III (4), 25-31.
134. Thorne, C. R., Grissenger, E. H. and Murphey, J. B. (1984). Field Study of Ephemeral Cropland Gullies in Northern Mississippi. Paper presented at the 1984 Winter Meeting of the American Society of Agricultural Engineers.
135. Thorne, C. R., Zevenbergen, L. W., Grissenger, E. H. and Murphey, J. B.(1986). Ephemeral Gullies as Sources of Sediment. Proceedings of the Fourth Federal Inter-Agency Sedimentation Conference, 3. pp 152 – 161.
136. Toy, T.J., G.R. Foster, and K.G. Renard. (2002). Soil erosion: processes, prediction, measurement, and control. John Wiley and Sons, New York, NY
137. Traboulsi, M. (2010). La pluviometrie moyenne annuelle au Liban : interpolation et cartographie automatique, Journal scientifique Libanais, Conseil national de la recherche scientifique, Volume 11, No 2, pp. 11-25.
138. Turner, D., Lucieer, A., & Watson, C. (2012). An automated technique for generating georectified mosaics from ultra-high resolution unmanned aerial vehicle (UAV) imagery based on structure from motion (SfM) point clouds. Remote Sensing 4. pp.1392–1410. DOI: 10.3390/rs4051392.
139. USGS, (2006). SRTM30 Documentation, Available online at: ftp://e0srp01u.ecs.nasa.gov/srtm/version2/SRTM30 (accessed 01/08/2006).
140. Valentine P.C., Scully L.A., Fuller S.J. (2004). Terrain Ruggedness Analysis and Distribution of Boulder Ridges and Bedrock Outcrops in the Stellwagen Bank National Marine Sanctuary Region —Posters presented at the Fifth International Symposium of the Geological and Biological Habitat Mapping Group, Galway, Ireland.
141. Veitinger J., Purves R. S., Sovilla B. (2016). Potential slab avalanche release area identification from estimated winter terrain: a multi-scale, fuzzy logic approach/Natural Hazards and Earth System Sciences, 16, pp. 2211–2225.
142. Warren, S. D., Mitasova, H., Jourdan, M. R., Brown, W. M., Johnson, B. E., Johnston, D. M., Watson, C. C. (2000). Digital terrain modeling and distributed soil erosion simulation/measurement for minimizing environmental impacts of military training. Colorado State University, Fort Collins, CO.
143. Warren, S.D., Diersing, V.E., Thompson, P.J., Goran, W.D. (1989). An erosion-based land classification system for military installations. Environmental Management, 13,251-257.
144. Wedding L.M., Friedlander A.M., McGranaghan M., Yost R.S., Monaco M. E. (2008). Using bathymetric LIDAR to define nearshore benthic habitat complexity: implications for management of reef fish assemblages in Hawaii. Remote Sens Environ, 112(11), pp. 4159–4165.
145. Westoby, M.J., Brasington, J., Glasser, N.F., Hambrey, M.J., Reynolds, J.M. (2012). 'Structure-from-Motion' photogrammetry: A low-cost, effective tool for geoscience applications. Geomorphology 179. pp 300–314. https://doi.org/10.1016/j.geomorph.2012.08.021.
146. Wilson, J.P., and J.C. Gallant. (2000). Terrain analysis: principles and application. John Wiley & Sons, New York, NY.pp. 1-27.
147. Wischmeier, W.H., Smith, D.D. (1978). Predicting rainfall erosion losses, a guide to conservation planning. Agriculture Handbook No.537, US Department of Agriculture Washington D.C.
148. Wood, J. (1996) The geomorphological characterization of digital elevation models, PhD Thesis. University of Leicester.

149. Wood, J. (2009) Geomorphometry in LandSerf. In: Hengl, T., Reuter, H.I. (Eds.), Geomorphometry — Concepts, Software, Applications. Developments in Soil Science, vol. 33. Elsevier, Amsterdam, pp. 333–349.
150. Woodby, D., Carlile, D., Hulbert, L. (2009) Predictive modeling of coral distribution in the Central Aleutian Islands, USA. Mar Ecol Prog Ser. 397, pp. 227–240.
151. 180. Woodcock C. E., Strahler. A H., "The Factor of Scale in Remote Sensing," Remote Sensing of Environment, vol.21, pp.311-332, 1987.
152. Wright, D.J., Heyman W.D. (2008) Introduction to the special issue: marine and coastal GIS for geomorphology, habitat mapping, and marine reserves. Mar Geod. 31, pp. 223–230.
153. Wu, J. (2013). Effects of changing scale on landscape pattern analysis: scaling relations Landscape Ecol. 19, pp. 125–138.
154. Xu, Z. X., Li, J. Y. (2003) Estimating basin evapotranspiration using distributed hydrologic model. Journal of Hydrologic Engineering 8, 74-80.
155. Yamazaki D., Ikeshima, D. Tawatari, R. Yamaguchi, T. O'Loughlin, F. Neal, J.C. Sampson, C.C. Kanae, S.& Bates, P.D. (2017), A high accuracy map of global terrain elevations Geophysical Research Letters, vol.44, pp.5844-5853, 2017 doi: 10.1002/2017GL072874
156. Zevenbergen, L. W. (1989). Modeling Erosion Using Terrain Analysis. A thesis was presented for the Doctor of Philosophy degree at the University of London.
157. Zevenbergen, L. W., Thorne, C. R. (1987). Quantitative analysis of land surface topography. Earth Surface Processes and Landforms, 12. pp. 47-56.
158. Zhang, W., Montgomery, D. R. (1994). Digital elevation model grid size, landscape representation, and hydrologic simulations. Water Resources Research 30,1019-1028.

Prof. Jean Doumit received his Ph.D. in geosciences from Kuban State University in the Russian Federation. He has since worked as a part-time faculty member at several universities throughout Lebanon. Currently, Prof. Doumit is a full Professor of Geography in the faculty of Letters and Human Sciences at Lebanese University.
He teaches subjects in Remote Sensing and Geospatial Information Science and Technology. His research interests include Digital Cartography, Geospatial Data Analysis, Remote Sensing, and GIS, among others. Prof. Doumit has received multiple international awards for his success and findings in scientific research and is the author or coauthor of several scientific books and publications.